NASA/CR-1999-209334

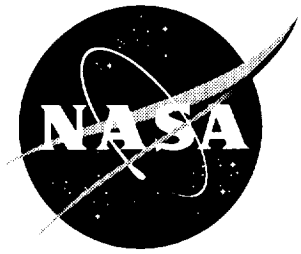

Receptivity of Flat-Plate Boundary Layer in a Non-Uniform Free Stream (Vorticity Normal to the Plate)

Final Report

M. N. Kogan, V. G. Shumilkin, M. V. Ustinov, and S. V. Zhigulev
Central Aerohydrodynamics Institute (TsAGI), Zhukovski, Moscow Region, Russia

National Aeronautics and
Space Administration

Langley Research Center
Hampton, Virginia 23681-2199

Prepared for Langley Research Center
under Cooperative Agreement NCC1-241

June 1999

Available from:

NASA Center for AeroSpace Information (CASI)
7121 Standard Drive
Hanover, MD 21076-1320
(301) 621-0390

National Technical Information Service (NTIS)
5285 Port Royal Road
Springfield, VA 22161-2171
(703) 605-6000

1. Part 1. Experimental study of wake-boundary layer interaction for different leading edge shapes

Introduction

Recent progress in both the linear and nonlinear aspects of stability theory has highlighted the importance of receptivity problem [1]. One of the most unclear part of receptivity studies is the receptivity of boundary-layer flow to vortical disturbances. Some experimental [2] and theoretical [3] results permits to propose that quasi-steady outer-flow vortical disturbances may trigger by-pass transition. For this reason the experimental and theoretical study of vortex-boundary layer interaction is an actual task. In present work such interaction is investigated for the vorticity normal to the leading edge. The interest to this type of vortical disturbances arises from the theoretical works of M.E. Goldstein et. al. [4-6], where it was shown that the flow around the leading edge amplifies them through vortex lines stretching. Far downstream, the amplification leads to significant distortion of the boundary layer and, finally, to localized flow separation.

The purpose of experimental part of this work is study of the role of vortex lines stretching mechanism in non-uniform flow interaction with boundary layer. Such non-uniformity was produced by the wake behind a wire or a set of wires and its interaction with boundary layer at the plates of different leading edge shapes was investigated. Laminar-turbulent transition caused by wake/boundary layer interaction is a topic of investigation too.

1.1. Experimental setup and equipment

The experiment was performed in a low-turbulence direct-flow wind tunnel T-36 I of Central Aerohydrodynamics institute (TsAGI). The test section is 2.6 m long, 0.5 m wide and 0.35 m high, and is preceded by 12:1 contraction. The free-stream turbulence level in the test section is 0.06%, measured in the band 5-1500 Hz at velocities **greater** then $5m/s$. .

The general outline of experimental setup is shown in Figure 1 a. Interaction of wake from vertically stretched wire or a set of wires with the boundary layer over the horizontally mounted plate was studied. Four plates with different shapes of leading edge shown in Figure 2 were used. These plates of 1810 mm long, 500 mm wide and 20 mm thick were made from Plexiglas and had drains for static pressure distribution measurements. Plates # 1,2 and 4 had semi-elliptical leading edges of aspect ratios 8:1, 4:1, and 1:1. The last semicircular leading edge is too blunt, so local separated bubble occurred when the flow around it is symmetric. In order to achieve the non-separated symmetric flow over possibly blunt nose, the leading edge of plate #3 was designed. The contour of this leading

edge is described by expression

$$\overline{x} = -\sqrt{a^2 - \overline{y}^2 + \frac{2a\overline{y}}{\tan(2\overline{y}\arctan a)}} + \sqrt{a^2 + \frac{a}{\arctan a}} \qquad \overline{x} = 2\frac{x}{H} \qquad \overline{y} = 2\frac{y}{H}$$

where x, y are longitudinal and vertical coordinates of nose contour, $H = 20mm$ - thickness of the plate, $a = 4.65$. The radii of noses of plates #1,2,3,4 are $1.25mm$, $2.5mm$, $5.31mm$, $10mm$ respectively, so the plate #1 had the most sharp nose and nose radius grows monotonically with number of plate increase.

To control the stagnation point position over nose two flaps mounted above the plate near its trailing edge were used. The wires were stretched at the holder moving horizontally with steps 0.1 mm. All three components of velocity were measured with a DISA 55M01 anemometer. A single hot wire probe with horizontal wire of diameter $5\mu m$ and a sensitive length 0.5 mm was used for streamwise velocity measurements. Spanwise and vertical components of velocity were measured by X-wire probe of similar dimensions. The probe was mounted on a carriage and was transversed in streamwise and vertical directions. The accuracy of probe movement in vertical direction was 0.1 mm. Instead of probe movement in spanwise direction the horizontal transmission of the wires was used. Coordinate system and general designations used are shown in Figure 1 b, c.

1.2. Undisturbed flow around plates

The interaction of non-uniform flow with boundary layer over the plates of different leading edge shape was studied for free-stream velocities $u_\infty = 5m/s$ and $17m/s$. the most of results were obtained for $u_\infty = 17m/s$, so the undisturbed flow around the plates for this velocity only will be described in details. Brief information concerning flow with $u_\infty = 5m/s$ is presented in the end of this subsection, for more fully it is described in previous report.

For plates #1-3 the flow around the leading edge was adjusted to be symmetric. Symmetric flow over blunt semicircular nose of plate #4 was separated, with the local separated bubble located near nose-plate mating appears. To eliminate separation the attachment line was moved to upper part of nose and flow around plate #4 becomes substantially asymmetric.

Velocity distributions along the upper and lower sides of nose for all plates computed from static pressure measured are shown in Figure 3. For plates #1-3 the velocity at lower and upper sides coincides within 2% of outer flow velocity, so the flow around leading edge was almost perfectly symmetric. Velocity distribution over the plate #4 is substantially asymmetric, with velocity at upper side of it is smaller then this at the lower side. Moreover, velocities in first two points at upper side are approximately the same. So, stagnation point was located between two first drains i.e. at y between 2 and $4mm$.

At all plates the flow accelerates initially and then retreads to u_∞ near the beginning of the plane part of the surface. In accordance with theory, the largest

acceleration should occur at the most blunt nose and the velocity maximum should decrease as the leading edge becomes sharper. This rule really fulfilled for velocity distributions at plates #1-3. The most blunt nose plate #4 stands out of this rule, with the velocity maximum at the upper side of it is the smallest. The reason of this is the asymmetric flow about leading edge of plate #4.

Velocity distributions along the plane parts of all plates measured by hot wire probe outside the boundary layer (at $y = 40mm$) are plotted in Figure 4. For plates #1-3 there exist a slight negative pressure gradient along x and pressure gradient is slightly positive for plate #4. All these gradients are very small, with velocity varies by 1% over the length of $1m$.

Velocity profiles in the boundary layer at different distances x from the leading edge for plates #1-4 are shown in Figures 5-8. Near the leading edge ($x = 20$ and 40 mm) the profiles have maxima at the joint of boundary layer and inviscid flow. The velocity at these maxima (shown by open symbols in figure 3) closely coincides with velocity obtained from static pressure measurements. Far from leading edge velocity profiles tends to Blasius profile for flat-plate boundary layer.

At plates #1-3 the flow in boundary layer was laminar with r.m.s. velocity pulsations in it was less then 0.3% of u_∞ over all plates length. Laminar- turbulent transition was observed in a boundary layer of plate #4 at $x \sim 500mm$. Two factors may cause the transition: positive pressure gradient and amplification of outer flow pulsations at the blunt nose.

Only plates #2 and 4 were tested for outer flow velocity $5m/s$. Velocity distributions over noses for this speed were the same as these for $u_\infty = 17m/s$ with accuracy $\sim 4/\%$. The distributions of velocity over plane parts of the plates for $u_\infty = 17m/s$ and $5m/s$ coincides within accuracy of measurements ($\sim 0.3\%$). The boundary layer at both plates in flow with $u_\infty = 5m/s$ was laminar, with r.m.s. velocity pulsations in it were less then 0.2% from u_∞.

1.3. Flow in wakes

In the reported work four wakes were used as a source of upstream inhomogeneity. One of them is steady laminar wake behind a wire of $d = 0.09mm$ in a flow with $u_\infty = 5m/s$. The Reynolds number of this wake based on diameter of the wire was $R_d = u_\infty d/\upsilon = 31$ and velocity pulsations within it are the same as in the free stream. Two next wakes: the wake behind the wire of $d = 0.09mm$ in flow with $u_\infty = 17m/s$ and the wake from wire of $d = 0.3mm$ in flow with $u_\infty = 5m/s$ were not entirely laminar. Both of them had Reynolds number $R_d \simeq 105$, which exceeds the critical Reynolds number $R_* \sim 40-50$ for steady laminar flow around the cylinder [8]. So, the Karman vortex street occurs in the flow behind wire. This street decays gradually downstream and for distance **greater** then 100 d, the peak in velocity pulsation spectrum associated with it disappears [8]. Pulsations in such decayed Karman vortex streets were about 0.2% of the outer flow velocity. It is more then in laminar wake, but it is sufficiently less then in turbulent one.

The fourth wake was a wake behind a set of wires of $d = 0.09mm$ placed in distance $D = 6mm$ from each other along the span in flow with $u_\infty = 17m/s$.

Profiles of mean velocity in all wakes behind single wire were found well correlate with formula

$$\frac{u}{u_\infty} = \left[1 - u_0 \exp\left(-\ln(2)\left(\frac{z}{b}\right)^2\right)\right] \qquad u_0 = \frac{A}{\sqrt{\frac{L}{d} - l_0}} \qquad \frac{b}{d} = B\sqrt{\frac{L}{d} - l_0} \tag{1.1}$$

where u_0 is velocity deficit, b - half-width of the wake, L - distance from the wire, A, B, l_0 -constants. For laminar wake it is an exact solution of Prandtl equations with $A = \frac{C_d}{4}\sqrt{\frac{R_d}{\pi}}$, $B = 2\sqrt{\frac{\ln 2}{R_d}}$, $l_0 = 0$. From experimental data for wake behind wire of $d = 0.09mm$ in flow with $u_\infty = 5m/s$ it was found that $A = 1.35$.

For wakes of wire of $d = 0.3mm$ in flow with $u_\infty = 5m/s$ and of wire of $d = 0.09mm$ in flow with $u_\infty = 17m/s$, which are decayed Karman vortex streets (1.1) is only a fit of experimental data. Velocity deficits u_0,and half-widths b of these wakes as functions of distance from wire L are plotted in Figures 9 and 10 respectively. Lines in this figures shows fits (1.1) with constants A, B and l_0 found from experimental data.

The flow in the wake from a set of wires is more complicated. Mean velocity profiles measured in these wakes for distances from wires $L = 60$, 170, 270, 370, 550, $800mm$ are shown in Figure 11. Not far from wires ($L = 60mm$) the wakes of the individual wires developed independently one from another. As L increases ($L = 170$, 270 and $370mm$) the wakes becomes wider and the interaction of neighboring wakes began. Finally, for $L = 550$ and $800mm$ the velocity profile becomes near-sinusoidal and it remains qualitatively the same for larger distance from wires. The flow distortion Δu, i.e. the difference between maximal and minimal velocities in profiles as function of L is shown in Figure 10 together with velocity deficit in the wake from one wire. There were observed no distinctive difference between the L- dependencies of flow distortion in wakes from the single wire and from the set of wires. Theoretically, this difference should exist, but the accuracy of the measurements is not enough to observe it. The maximal velocity pulsations in the wake from set of wires were about $0.2 - 0.3\%$, and slightly exceeds the pulsations in a single wire wake.

1.4. Wake-boundary layer interaction

Interaction of the boundary layer at the plates of different leading edge shapes with wakes described in previous section was studied for various distances from wire to leading edge. Geometry and flow parameters of all configurations tested, that is diameter and amount of wires, velocity, number of plate used, distance

from wire to leading edge are listed in the Table. The Table also includes characteristics of wakes at the leading edge position and other important parameters describing these configurations.

Interaction of wake behind single wire with boundary layer was studied in details, so most of this section is devoted to this topic. Only preliminary results concerning a wake from a set of wire action on boundary layer are described here.

1.4.1. Steady boundary layer distortion

For small outer flow velocity of 5 m/s (configurations 15-19 in Table) the wake slightly distorted boundary layer. The maximum velocity deviation from undisturbed flow was only 3 times grater then velocity deficit in oncoming wake. The slight effect of vortical disturbances on boundary layer in this regime is caused by low unit Reynolds number $R_1 = u_\infty 1/v = 3.45 * 10^5$ and large boundary layer thickness comparable with the radius of the plate nose. Main results were obtained for outer flow velocity 17 m/s corresponding to higher unit Reynolds number $R_1 = 1.17 * 10^6$. For this value of R_1 the maximal flow distortion was about 10 times grater, then oncoming flow inhomogeneity.

There were observed three qualitatively different regimes of single wire wake /boundary layer interaction: linear regime, symmetric nonlinear regime and antisymmetric nonlinear regime. General features of these regimes will be illustrated for interaction of wake behind the wire of $d = 0.09mm$ in flow with $u_\infty = 17m/s$ with plate #2. For this wake and plate combination linear regime was observed in configuration 8, when $L = 725mm$; symmetric nonlinear regime occurred in configuration 6 when $L = 250mm$ and antisymmetric nonlinear regime occurred for $L = 40mm$ in configuration 4 (see Table). Evolution in x of spanwise distributions of streamwise velocity in boundary layer observed in these three regimes are shown in Figures 12, 13, and 14 respectively. The boundary layer flow distortions Δu_b as functions of distance from leading edge x for the same regimes are plotted in Figure 15. This distortion Δu_b is determined as a difference between the maximal and minimal velocities in the spanwise profile measured for y corresponding to $u = 0.5u_\infty$.

Linear regime occurs when the distance from wire to leading edge is large enough and velocity deficit of oncoming wake is small. In this case the shape of spanwise distribution of velocity in boundary layer approximately repeats the velocity profile in the wake. The amplitude of boundary layer distortion grows almost linearly with distance from leading edge.

When the wire was placed closer to leading edge, the boundary layer response to the wake becomes noticeable nonlinear. Nonlinearity manifests itself in deformation of spanwise profile of velocity in boundary layer (see Figures 13 and 14). For moderate distance from leading edge $L = 250mm$, the profile remains symmetric with respect to the wake centre, so this regime of interaction is called as nonlinear symmetric one. If the wire was placed nearby to leading edge

($L = 40mm$), the boundary layer response to the symmetric wake becomes antisymmetric as shown in Figure 14). This type of wake/boundary layer interaction will be called as nonlinear antisymmetric regime. There are two possible antisymmetric regimes: the "right" regime (shown in Figure 14) with maximum of velocity at the right side and the "left" one with maximum at the left side. Both of these regimes were observed and they change each other randomly when the wind tunnel was stopped and started again. For definiteness, in all next figures dealing with antisymmetric flow distortion the right regime is shown. Unlike the linear regime, the flow distortion in both nonlinear regimes reaches maximum at about $100mm$ from leading edge and then decay downstream (see Figure 15). At large distance from leading edge (600mm for example), the distortion from weak wake initiating linear regime becomes **greater** than distortion from high-deficit wake initiating non-linear regime.

Streamwise velocity distributions in plane normal to flow direction ($y, z-$ plane) for nonlinear antisymmetric, nonlinear symmetric and linear regimes are shown in Figures 16a), 17a) and 18. In addition to these data, distributions of spanwise and vertical components of velocity in this plane for nonlinear antisymmetric and nonlinear symmetric regimes are shown in Figures 16 b) and 17 b). Vectors plotted in these Figures are proportional to projection of velocity onto (y, z) plane. Dashed lines $y = 2mm$ shows the outer edge of boundary layer where $u = 0.99u_\infty$. For distances from the plate $y < 1mm$ the measurements of vertical and spanwise velocity components becomes impossible because of probe size, so the reconstruction of the flow based on subsequent speculations is drawn here. Figure 17 b) shows that nonlinear symmetric regime of boundary layer distortion is associated with two counter-rotational vortices located above the boundary layer at $z \cong 4mm$. In nonlinear antisymmetric regime only one streamwise vortex at $z \cong 4mm$ was observed as shown in Figure 16 b).

To explain the formation of three different types of boundary layer distortion, let's consider the conceptual scheme of wake/leading edge interaction, shown in Figure 19. The wake may be considered as a pair of counter-rotational vortex sheets. Stretching of these sheets vortex lines around the nose produce a pair of counter-rotational streamwise vortices at the plate surface. The lifting of fluid between the vortices causes the diminishing of the streamwise velocity, whereas at the periphery of them the downwards outer flow leads to growth in the boundary layer velocity. This explains the boundary layer distortion in linear regime.

In nonlinear symmetric regime the local maximum of velocity in the middle of the wake appears (see Figure 13). Figure 17 a) shows, that this maximum becomes more pronounced in the vicinity of the wall. Formation of this maximum may be explained if we suppose that when streamwise vortices become strong enough two small-size secondary vortices originate within the boundary layer as drawn in Figure 17 b). Contrary to main vortices, the secondary vortices drops fluid in the middle and produce local velocity maximum.

The loss of symmetry and antisymmetric regime production may be explained

by the instability of streamwise vortex system associated with nonlinear symmetric regime. This phenomenon is similar to the well-known Crow instability [7] of a pair of streamwise counter-rotational vortices which manifests in twisting of vortices in a spiral manner. The result of it should be the lifting of one vortex and the remained vortex will produce an antisymmetric flow distortion. Such vortex is really seen in Figure 16 b), where flow in $(y,z)-$ plane for antisymmetric regime is shown. Another point in support of the instability mechanism of antisymmetric regime formation provides the flow distortion development in configuration 10 shown in Figure 20 a). In this configuration initially symmetric boundary layer distortion gradually becomes asymmetric with x growth and finally reaches completely antisymmetric state at $x = 200mm$.

Contrary to unbounded stream where the Crow instability occurs for all vortex strengths, the wall and viscosity should stabilize the vortex pair. The instability should occur only if the vortices are strong enough to lift one of them. In accordance with rapid distortion theory [4], the streamwise vorticity is proportional to initial vertical vorticity in the wake which may be estimated as u_0/b. The instability should exist if this vorticity is large with respect to some characteristic velocity gradient in a flow around the nose. If we suppose the inviscid nature of instability, this gradient should be u_∞/r where r is the radius of nose, and the non-dimensional stability criterion $K = \frac{u_0}{b}\frac{r}{u_\infty}$ can be constructed. If the instability related with vortices/boundary layer interaction is expected, the vorticity should be related to velocity gradient in boundary layer over nose. In this case, the stability criterion becomes $K_\nu = \frac{u_0}{b}\frac{\delta}{u_\infty}$, where $\delta = \left(\frac{r\nu}{u_\infty}\right)^{1/2}$ is the boundary layer thickness in the stagnation point. Both criteria for all configurations tested are given in Table. Comparison of two criteria shows that transition of a symmetric flow into antisymmetric some better correlates with inviscid criterion K. As a rule, boundary layer flow is symmetric for $K \leq 0.1$ and becomes antisymmetric for $K \geq 0.2$. The exceptions to this rule are configurations configurations 18 and 19 and 13,14, where the symmetric distortion occurs for $K \geq 0.2$. In two first configurations (18,19) the unit Reynolds number is too small, so the wake width is approximately equal to boundary layer thickness and wake-boundary layer interaction is fully viscous. In two other configurations 13 and 14 the flow around the nose of plate #4 was not symmetric, so the comparison of the results with these for symmetric flow around plates #1-3 is not correct. In any case this correlation shows the significant role of inviscid processes in symmetry/antisymmetry transformation.

Integral characteristics of boundary layer distorted by wake in all three regimes of interaction (displacement thickness δ^*, momentum-loss thickness δ^{**}, and form-parameter $H = \delta^*/\delta^{**}$) as functions of Z are shown in Figure 20 b). This Figure shows, that wake strongly deforms the boundary layer and it's parameters vary by an order of unity. In accordance with the previous speculations, in linear regime the boundary layer becomes thicker in the wake centre. In nonlinear symmetric

regime the displacement thickness grows at sides of the wake and remains almost unchanged in it's centre. The minimum of δ^* in the wake's centre is probably caused by downward flow produced by secondary vortices. The form of $\delta^*(z)$ dependance in antisymmetric regime is antisymmetric too, with δ^* increases at the left side where fluid moves upward and decrease at the right side where downward flow (y, z) plane was observed (see figure 16 b).

Vertical distributions of boundary layer distortion Δu_b measured in different configurations and different distances from leading edge x are shown in Figure 21. For convenience, these distortions are normalized by their maximums and y is referred to boundary layer displacement thickness δ^* in the places, where the distortions were measured. In these variables all data are grouped near two curves, shown by thick solid and dashed lines, with data for nonlinear symmetric and antisymmetric regimes lie near one curve and data for linear regime form the second curve. Curve for nonlinear regimes well coincides with profile of low-frequency pulsations in boundary layer under enhanced outer flow turbulence level measured by Kendall [9]. Maximum of distortion in linear regimes of interaction is shifted from the wall to $y \simeq 1.7\delta^*$.

To study the role of leading edge in wake/boundary layer interaction the plates #1-3 were tested for the same outer flow conditions. Three tests of this type were made for $u_\infty = 17m/s$, $d = 0.09mm$ and distances from wire to leading edge $L = 40$, 250 and $725mm$. Results of them in form of $x-$dependencies of boundary layer distortions Δu_b and pulsations u' at all three plates for $L = 40$, 250 and $725mm$ are shown in Figures 22, 23 and 24 respectively. Distortions Δu_b plotted in parts *a)* of the Figures were determined as a differences between the maximal and minimal velocities in the spanwise profiles measured for y corresponding to $u = 0.5u_\infty$. Pulsations u' shown in parts *b)* of these Figures are the maximal over span values of r.m.s. streamwise velocity pulsations in frequency range $5 - 1500Hz$ measured for the same y. Distortion and pulsations measured in this way are close to their maximum values in the section $x = const$. The data about pulsations permits to estimate the influence of pulsations on steady boundary layer distortion development.

For small ($L = 40mm$) and large ($L = 725mm$) distances from wire to leading edge the influence of nose shape on boundary layer distortion is clearly defined. In these cases the distortion grows as radius of leading edge increase, with distributions of distortion over x are qualitatively similar for all shapes of leading edge. For $L = 725mm$ (see Figure 24 a)) the linear regime of distortion occurred at all plates. As was mentioned above, the distortion for this regime grows with x over the entire length of plate. At first glance, it would seem that the distributions of distortion over blunt nose plate #3 stands out of this rule, for distortion reaches maximum at $x = 300mm$ and then decreases. However, this is not the case for the decrease of distortion is caused by laminar-turbulent transition occurred at $x \sim 300 - 400mm$ (see Figure 24 b)). Laminar-turbulent transition in this configuration is considered in subsection 2.4.2 in more detailes (see also Figure 29).

At plate #2 the pulsations are sufficiently large to effect on the steady boundary layer distortion too. Only at plate #1 the pure steady flow inhomogeneity interaction with boundary layer was observed. For this reason, the data obtained are insufficient for finding the quantitative relationship between the radius of nose and boundary layer distortion in linear regime. Whether the growth of distortion is linear in x or it saturates at some distance from leading edge is unclear yet.

For all other distances from wire to leading edge ($L = 40$ and $250mm$) the boundary layer remained laminar and effect of pulsations on steady distortion development was negligible. For $L = 40mm$ nonlinear antisymmetric regime occurred at all plates. The distributions of boundary layer distortion in this case shown in Figure 22 a) have maxima at moderate distance from leading edge and decayed for large x. The maximal over x distortion is approximately proportional to radius of leading edge, and distances from leading edge to maximum varies in inverse proportion to this radius. It should be remarked that in Goldsteins theory [4] the distance from leading edge to singularity is inversely proportional to radius of leading edge also.

Distributions of distortion over x measured for $L = 250mm$ and different plates were quite different, because they correspond to different regimes of wake /boundary layer interaction. At plate #3 the nonlinear antisymmetric regime occurred and distribution of Δu_b is similar to that for antisymmetric regime shown in Figure 22 a). Pure nonlinear symmetric regime occurred at plate #2 and distribution of distortion exhibited maximum and then decayed. At the most sharp leading edge plate #1 the $z-$ profiles of distortion for small x had features of nonlinear symmetric regime, but for $x > 300mm$ they becomes quite similar to profiles observed in linear regime. So, the distortion initially decays and then begins to grow in a manner familiar for linear regime. For small x, as usual, the maximal distortion occurred at blunt nose plate #3. But for large x the distortion at the most sharp nose plate #1 unexpectedly becomes grater, then those at more blunt nose plates #2 and #3.

Boundary layer response on the wake behind a set of 5 wires was studied only in four configurations: for $L = 40mm$ at plates #1and #3 (configurations 20 and 23) and for $L = 725mm$ at plates #1and #2 (configurations 21 and 22). Results in form of $x-$dependencies of boundary layer distortion Δu_b and pulsations u' are shown by dashed lines in Figure 22 (for $L = 40mm$) and Figure 24 (for $L = 725mm$) together with similar data for wake from single wire. Except configuration 22 with $L = 725mm$ and plate #2, the boundary layer distortion from a set of wires differs from those from a single wire less then 15%. In configuration 22 the distortion from the set of wires is two times greater then this from single wire. Consequently, the flow inhomogeneity amplification in this configuration depends crucially upon the shape of oncoming velocity profile. Hence, the wake/ boundary layer interaction in this regime is nonlinear. Figure 25 shows the evolution of spanwise profiles of mean velocity and its pulsations measured in configuration 22. Unexpectedly, no deformation of almost sinusoidal profile of oncoming flow

in boundary layer is seen in this Figure. Similar profiles corresponding to interaction of wake from a set of wires with plate #3 for $L = 40mm$ (configuration 23) are shown in Figure 26. For such small distance from wires to leading edge the oncoming flow is a superposition of five wakes from individual wires. These wakes initially interact with leading edge independently, so the velocity profile for $x = 25mm$ is a superposition of 5 profiles familiar for single wake /boundary layer interaction in nonlinear antisymmetric regime. The orientation of flow distortion from these wires is not the same, with three middle wires produced "left" regime and two side wires excited "right" one. The flow distortions in all but one wakes are identical and equal to flow distortion from single wire. This explains the coincidence of flow distortions from a single wire and a set of wires for small and moderate x. Sufficient interaction between neighboring wakes begins only for $x > 100mm$ where laminar-turbulent transition occurred and comparison of distortions becomes meaningful.

Response of boundary layer at sharp nose plate #1 to both near ($L = 40mm$) and far ($L = 725mm$) wakes seems to be linear, so the distortions from one wire and a set of wires were approximately the same (see Figures 22 and 24). Linear behavior of distortion is probably caused by weak vortex lines stretching by flow around sharp nose. However, all conclusions concerning boundary layer response on wakes linearity drawn here are quite preliminary and should be proved during the future work.

1.4.2. Laminar-turbulent transition caused by wake/boundary layer interaction

Laminar-turbulent transition excited by wake/boundary layer interaction was studied also. Boundary layer distortions Δu_b and pulsations u' as function of x measured in configurations where transition takes place are plotted in Figure 27. Two different types of transition may be distinguished. The first one is associated with origination of high pulsations ($\sim 6 - 8\%$) immediately in the first near-nose section, where the measurements were made. This type of transition occurred in configurations 12, 13, 23 when near wake interacted with blunt nose plates #3 and #4. Example of mean velocity and pulsations profiles development for this type transition excited by wake from single wire in configuration 12 is shown in Figure 28. Similar results for transition from a set of wires in configuration 23 may be seen in Figure 26. Possible reason of pulsations origination near the leading edge may be local flow separation provoked by wake. Really, the boundary layer distortion in the near nose section $x = 20$ or $25mm$ in configurations 12, 23 are very strong (see Figures 28, 26) and the velocity profiles near nose may correspond to separated flow in boundary layer. It's interesting, that in flow distorted by a set of wires (configuration 23) the pulsations originated in wake behind one of wires (fourth from left side) only. It may be caused by interaction of distortions of different orientations ("left" and "right") near the nose. Behind

the second wire where the same interaction takes place the growth of pulsations occurs too, but it begins later at $x = 100mm$. For regimes of interaction shown in Figures 26 and 28 the effect of pulsations on mean flow development is significant over whole plate surface. The flow in the centre of wake becomes turbulent at small distance $\sim 100 - 200mm$ from leading edge. Further, the turbulent flow spreads on the region much wider then the part of boundary layer distorted by the wake.

The second type of transition is characterized by gradual growth of initially small pulsations. Complete transition of this type was observed in configurations 11 and 22 for boundary layer distorted by single wire and a set of wires respectively. Development of mean velocity and pulsations profiles in course of transitions in these configurations are shown in Figures 29 and 25. For the wake from single wire/boundary layer interaction (Figure 29) the maximal pulsations initially (at $x = 150mm$) were observed at the sides of the wake where spanwise gradient of velocity is maximal. In this stage of transition pulsations still have no effect on mean velocity profile. Further at $x = 350mm$ the additional maximum of pulsations appears in the middle of the wake and distribution of pulsations becomes wider. Reaching high level of $\sim 10\%$ of u_∞ pulsations begin to deform mean velocity profile with velocity increases at the sides of the wake. Finally, at $x = 400mm$ several maximums of pulsations forming peak-valley structure appears and turbulence begins to spread in spanwise direction. In final section $x = 500mm$ the turbulent part of boundary layer is about 5 times wider then oncoming wake.

Transition excited by a set of five wires shown in Figure 25 exhibits the same features. Initially at $x = 300mm$ maximums of pulsations are located between maximums and minimums of mean flow velocity and coincides with maximal gradients of velocity in spanwise direction. Further ($x = 350mm$) maximums of pulsations move to the minimums of mean velocity and finally at $x = 500mm$ turbulence spreads to width region. It's interesting, that pulsations at sides of disturbed domain are grater then those in it's central part during entire transition process.

To reveal the type of disturbances responsible for transition, the power spectra of streamwise velocity pulsations were measured. These spectra in configuration 11 in section $x = 150mm$, where pulsations began to grow are shown in Figure 30. From this Figure it is seen that the spectra measured in the centre of wake, at side of it, and far from the wake are quite different. A broad wave packet with frequencies around $720Hz$ can be seen in the spectrum at side of the wake. Spectrum in the centre of it contains this packet too, but the major part of its energy is confined in low frequency band. The reduced frequency of this wave packet $F = 10^6 \cdot 2\pi\nu f/u_\infty^2 = 227$ is approximately equals to the frequency of high-frequency pulsations observed in flow with embedded streamwise vortices in [10]. The spectrum measured far enough from wake contains packet with $f \sim 500Hz$ or $F \sim 150$. This packet, in principle, may be formed by Tollmien-Schlichting

waves generated in boundary layer by the disturbances within the wake.

Spectra measured in configuration 22 where transition excited by a set of wires was observed are shown in Figures 31 and 32. Figure 31 shows spectra measured at the side of wake for $z = -17mm$, whereas spectra measured at the nearest to centre maximum of mean velocity ($z = -3mm$) are plotted in Figure 32. Three spectra measured at beginning ($x = 150mm$), middle ($x = 200mm$) and end ($x = 350mm$) of transition are presented in both Figures. A packet with frequency$\sim 720Hz$ the same as for single wire is seen only in spectrum at side of wake in the beginning of transition. Other spectra measured at side of wake are broadband, with low frequency pulsations grow predominantly over the middle and end of transition. In the centre of wake all spectra are broadband and transition here is associated with growth of low-frequency pulsations.

1.4.3. Discussion

In this section the data obtained will be compared with recent experimental and theoretical results dealing with boundary layer receptivity to quasi-steady outer flow vortical disturbances and subsequent amplification of these disturbances in a boundary layer. For convenience of such comparison, let's introduce the amplification coefficient k defined as $k = \Delta u_b/u_0$. This coefficient as function of Reynolds number $R = u_\infty x/v$ computed for different regimes of single wire wake interaction with plates #1 and 3 are plotted in Figure 33 a) and b) respectively. For the influence of flow inhomogeneity amplitude u_0 is excluded by means of amplification coefficient introduction, the spanwise scale of flow inhomogeneity (b) remains as a single parameter describing oncoming flow. From Figure 33 one can see that near the leading edge the boundary layer response to flow inhomogeneity is almost independent from it's scale. At large distance from leading edge large scale disturbances with $b = 1.6mm$ ($L = 720mm$) amplify and small scale ones with $b = 0.88$ and $0.46mm$ ($L = 250$ and $40mm$) decay or remain almost constant. Similar conclusion may be drawn from Kendall's [9, 11] experimental data on transition driven by free-stream turbulence if the correlation between the spanwise λ and time $\tau \sim 1/f$ scales of free-stream turbulence $\lambda \sim const \cdot \tau \sim const/f$ is assumed. Measured in [11] r.m.s. velocity pulsations in six frequency bands shown as function of R in Figure 34 reveals the similar behavior as amplification coefficients in Figure 33. Really, near the nose the amplitudes **in all bands** are approximately the same, so disturbances of all scales amplify almost equally here. For large Reynolds number (far from leading edge) the low frequency or large scale pulsations grow but small size or high frequency ones remains almost independent from R. Another proof of this trend may be seen in Figure 35 where broadband r.m.s. pulsations in boundary layer as function of spanwise wavenumber $\overline{\beta} = \frac{2\pi v}{u_\infty \lambda}$ are plotted. This curve is computed from the cross-correlation data given in Figure 5 of [9]. Figure 35 directly shows, that large-size disturbances are more amplified than the small-size ones. Nevertheless, there exist maximum

of amplitude at $\overline{\beta} \sim 2.5 \cdot 10^{-4}$ and very large-size pulsations grow more slowly. Estimates of $\overline{\beta}$ in our experiments obtained assuming $\lambda \sim 4b$ are $\overline{\beta} \sim 8 \cdot 10^{-4}$ for large scale inhomogeneity corresponding to $L = 720mm$ and $\overline{\beta} = 1.5 \cdot 10^{-3}$ and $3 \cdot 10^{-3}$ for near wakes with $L = 250$ and $40mm$ respectively. So, the largest scale inhomogeneity used in our tests is too small with respect to optimal size of disturbances exhibiting maximal amplification in [9]. This fact explains relatively weak growth of disturbances observed here with respect to $30 - 60$ times amplification of low frequency pulsations in boundary layer reported in [11]. Another possible reason of weak growth of disturbances in our experiment is the influence of non-linearity, for boundary layer distortion was very large $\sim 0.3 - 0.5u_\infty$ with respect to r.m.s. pulsation in [11] been $3 - 5\%u_\infty$.

If we are of the opinion that all scales of flow inhomogeneity used in our tests are small and correspond to middle or high frequency pulsations in [9,11], the finding of two different vertical profiles of boundary layer distortion shown in Figure 21 becomes consistent with data of [11]. It turns out that vertical profiles of high frequency pulsations shown in Figure 36 are not self-similar and changes with distance from leading edge. For small x it is similar to well-known distribution for low-frequency pulsations shown by (**X**) in Figure 21 and it's maximum moves from wall as x increase. Similar correlation may be seen in Figure 21 where dashed curve with near-wall maximum is composed from data measured at $x = 150mm$, and solid curve with maximum far from wall is formed by distortions measured at larger x. However, the shift of maximum in linear regime may be caused by non-linearity i.e. large amplitude of distortion $\sim 30\%$ in our experiment. Really, it is the linear regime produces the maximal deviations of the boundary layer displacement thickness in the disturbed domain. In the centre of it δ^* exceeds the undisturbed value by factor of 1.4 (see Figure 20 b). So, it is unclear, what value of displacement thickness should be used for scaling of y in this regime. If some averaged $\delta^* \sim 1.2\delta_0^*$ (δ_0^* is displacement thickness of undisturbed boundary layer) was used, the curves for linear and nonlinear regimes would coincide.

The amplification coefficients obtained here may be more directly compared with theoretical results of [12], where the steady spanwise-periodic disturbances experienced maximal spatial growth were found. The amplification coefficient may be directly computed from the results of this work as $k = \sqrt{G}$, where G is the energy growth. If we assume that energy in initial section is proportional to u_0^2, the amplification coefficient computed in this manner will be proportional to that measured here. Figure 37 shows amplification coefficient as function of R for various $\overline{\beta}$ computed from results of [12]. This Figure is quite similar to Figure 33 a) where our experimental results are plotted, with large scale disturbances grows with R and small size ones decay in both Figures. Theory [12] gives the expression for wave number providing maximal growth as $\overline{\beta} \sim 0.45/\sqrt{R}$. For $R = 10^6$corresponding to $x \sim 800mm$ in our experiment it gives $\overline{\beta} = 4.5 \cdot 10^{-4}$ which correspond to spatial period $\lambda \sim 13mm$ or $b \sim 3.2mm$ and is two times

grater than maximal spanwise scale used in our tests.

In general, results dealing with amplification of steady inhomogeneity in boundary layer at sharp nose plate #1 obtained here are in qualitative agreement with available data about boundary layer response to free-stream turbulence. The amplification coefficients at blunt nose plate #3 exhibit the similar properties, but they are two times greater then these for sharp nose plate #1. So, the response of boundary layer at plate #3 to outer flow turbulence should be two times greater then this at sharp nose models usually used in such experiments. Consequently, one may suppose, that the similar development of transition at plate #3 will take place for twice smaller outer flow turbulence level. Due to most of bodies of practical use (wings, turbine blades and others) have blunt leading edges, this conclusion may be important for transition prediction.

2. Part 2. Theoretical study of boundary layer receptivity to steady outer flow inhomogeneity and resulting laminar-turbulent transition.

Introduction

Response of steady boundary layer on the plate to the steady outer flow inhomogeneity (or vorticity normal to leading edge) was studied in works of Goldstein et al [7]. Here it was found that the flow around the leading edge amplify the vortical disturbances throw the vortex stretching mechanism. Initially these vortices excite distortion of boundary layer flow growing linearly in streamwise direction. Far downstream the amplification result in appearance of flow inhomogeneity of finite amplitude. In the experiments described in section 1. the finite amplitude flow inhomogeneity in boundary layer was observed too.

Nevertheless, the laminar- turbulent transition is not caused directly by steady flow inhomogeneity, but it is provides conditions for flow instability with respect to unsteady pulsations. The stability of such boundary layer with steady spanwise modulation of velocity profile is studied theoretically in section 2.1.

The action of vortex stretching mechanism introduced by Goldstein et all [6] for the swept wing flow is a topic of section 2.2. In this flow additional mechanism of flow inhomogeneity amplification via generation of steady cross-flow instability modes was found. Results obtained in this section explains some data of experiment of section 1. and provides the new area for future experimental work. . .

2.1. Stability of boundary layer with steady inhomogeneity of velocity profile

In this section the stability of boundary layer flow with steady spanwise modulation of velocity profile is studied theoretically. Such modulation is a model

of a streaky structure originating in the boundary layer subjected to free-stream turbulence. The non-uniform flow in boundary layer produced by wake is another example of modulated flow. It's well-known that transition is not caused directly by steady flow distortion, but it's initiated by the growth of high-frequency travelling waves. For this reason, the stability studies of modulated flows are necessary for understanding of transition caused by outer flow turbulence. In contrast to generalized Rayleigh's equation approach used in [6], the stability analysis is based on more general linearized Navier-Stokes equations.

2.1.1. Problem formulation

Consider the stability of boundary layer flow with steady variations of velocity profile in spanwise direction. We'll use the coordinate system introduced in section 2 with lengths scaled with averaged over span boundary layer displacement thickness δ^*. Basic flow $\mathbf{V}_0(y,z)$ is considered to be spanwise-periodic with period T_z and homogeneous in streamwise direction. We present this flow in form of Fourier series

$$\begin{gathered}\mathbf{V}_0 = \{U_0(y),0,0\} + \mathbf{V}_i \quad \mathbf{V}_i = \sum_{n=-N}^{N} \mathbf{V}_{0n} e^{in\beta z} \\ \mathbf{V}_i = \{u_i, v_i, w_i\}\end{gathered} \tag{2.1}$$

where $U_0(y)$ - Blasius flow profile, $\mathbf{V}_i$ - flow inhomogeneity, $\beta = 2\pi/T_z$.

There are two general types of unstable disturbances in periodic flows: the disturbances of the same period as the basic flow (fundamental disturbances) and subharmonic ones. Disturbances of both types will be sought in common form

$$\mathbf{V}_p = \left[\sum_{n=-N}^{N} \mathbf{V}_n(z) e^{in\frac{\beta}{2}z}\right] e^{i(\alpha x - \omega t)} \quad \mathbf{V}_p = \{u,v,w\} \tag{2.2}$$

We'll consider the temporal stability i.e. complex ω corresponding to real α will be sought.

Substitution of complete flow-field $\mathbf{V} = \mathbf{V}_0 + \epsilon \mathbf{V}_p$ into Navier-Stokes equations and linearization in ϵ gives an eigenvalue problem for ω

$$-i\omega \mathbf{L}_2 \circ \mathbf{V}_p = \mathbf{L}_1 \circ \mathbf{V}_p \tag{2.3}$$

where $\mathbf{L}_1$ and $\mathbf{L}_2$ are linear operators including derivatives with respect to y. Discretization of (3.3) in y yields the eigenvalue problem for matrix

$$(\mathbf{A} - i\omega \mathbf{E})\mathbf{F} = 0 \qquad \mathbf{A} = \mathbf{D}^{-1}\widetilde{\mathbf{A}} \tag{2.4}$$

Here vector $\mathbf{F}$ includes discrete representation of disturbances and matrixes $\widetilde{\mathbf{A}}$ and $\mathbf{D}$ corresponds to operators $\mathbf{L}_1$ and $\mathbf{L}_2$.

2.1.2. Numerical method

In all works where stability of periodic flows is studied the matrixes $\widetilde{\mathbf{A}}$ and $\mathbf{D}$ were determined and eigenvalue problem (3.4) is solved. Here we'll introduce an alternative approach to stability of complex geometry flows which is based on algorithm for Navier-Stokes equations solution. This approach makes us possible to study the stability of any periodic flow using a code for DNS of periodic flows. In all of these codes the flow field is presented in form of two-dimensional Fourier series in (x, z) plane. If we fix a part of harmonics representing basic flow, then remaining harmonics will describe the evolution of disturbances. If the amplitude of disturbances is small enough, it's evolution is described by linearized (near the basic flow) Navier-Stokes equations. These equations may be written in form similar to (3.3)

$$\frac{\partial}{\partial t}(\mathbf{L}_2 \circ \mathbf{V}_p') = \mathbf{L}_1 \circ \mathbf{V}_p'$$

where $\mathbf{L}_1$ and $\mathbf{L}_2$ are the same as in (3.3). All codes for DNS solve the discrete version of these equations of form

$$\frac{\partial}{\partial t}\mathbf{G} = \mathbf{A}\mathbf{G}$$

Here $\mathbf{A}$ is the same matrix as in (3.4) and $\mathbf{G}$ contains discrete representation of disturbances. If the finite-difference scheme used in DNS code is known, the matrix $\mathbf{A}$ may be easily related with matrix of transition $\mathbf{B}$. The former matrix describes the evolution of disturbances over one time step τ and relates disturbances at time t, $\mathbf{G}^k$ and at time $t + \tau$, $\mathbf{G}$ as

$$\mathbf{G} = \mathbf{B}\mathbf{G}^k$$

Transition matrix may be directly computed using DNS code. For Crank-Nicholson scheme used in our code, matrix $\mathbf{B}$ is related with $\mathbf{A}$ as

$$\mathbf{B} = \left[\mathbf{E} - \frac{\tau}{2}\mathbf{A}\right]^{-1} \times \left[\mathbf{E} + \frac{\tau}{2}\mathbf{A}\right]$$

It is easy to prove that matrixes $\mathbf{A}$ and $\mathbf{B}$ have the same eigenvectors, and eigenvalues of $\mathbf{B}$, μ_j are related with eigenvalues of $\mathbf{A}$, λ_j as

$$\mu_j = \frac{1 + \frac{\tau}{2}\lambda_j}{1 - \frac{\tau}{2}\lambda_j}$$

So eigenvalues ω_j of stability problem may be obtained from μ_j as

$$\omega_j = -\frac{2i}{\tau}\frac{1 - \mu_j}{1 + \mu_j}$$

The form of disturbances corresponding to ω_j is determined by eigenvector of $\mathbf{B}$ associated with μ_j.

The method described here was tested by means of computation of Blasius flow stability and the secondary instability of finite-amplitude TS wave. The results were in excellent agreement with those of traditional methods.

2.1.3. Results

Stability of Blasius boundary layer with $R = u_\infty \delta^*/\upsilon = 1000$ distorted by harmonic velocity modulation or by localized flow inhomogeneity were studied. The first flow is a model of periodic streaky structure observed under enhanced outer flow turbulence level, the second one is a model of the single streak or distortion produced by wake studied in section 2. In both flows inhomogeneity velocity vector $\mathbf{V}_i$ had only streamwise component u_i of form

$$u_i = af(y)g(z)$$

where a is an amplitude, functions $f(y)$ and $g(z)$ defines vertical and spanwise distribution of flow inhomogeneity. Vertical distribution for both flows was

$$f(y) = \frac{\exp(-\frac{(y-y_0)^2}{\Delta^2}) - \exp(-\frac{(y+y_0)^2}{\Delta^2})}{\max\limits_y \left[\exp(-\frac{(y-y_0)^2}{\Delta^2}) - \exp(-\frac{(y+y_0)^2}{\Delta^2})\right]} \tag{2.5}$$

with parameters $\Delta = 1.2$ and $y = 1.4$ chosen for coincidence with profile of low-frequency pulsations measured in boundary layer subjected to free-stream turbulence [9]. This profile is plotted by solid line in Figure 22 *a* together with profile of velocity pulsations from [9] shown by points. For the harmonic inhomogeneity spanwise distribution was

$$g(z) = \cos \beta z$$

whereas for localized inhomogeneity it was represented as

$$g(z) = \frac{1-q}{2}\left[1 + (1+q)\sum_{n=1}^{N} q^n \cos n\beta z\right] \qquad q < 1 \tag{2.6}$$

The last function with $q = 0.63$ shown in Figure 22 *b* has a narrow maximum within $z = 0$ and vanishes over the remanding part of period.

Due to basic flow symmetry, the disturbances may be symmetric or antisymmetric, i.e. the streamwise velocity of disturbances may be even or odd function of z. As was mentioned above, the disturbances of both these types may have fundamental or subharmonic period. So, there exist four types of unstable modes. Figure 23 shows the spanwise distribution of streamwise velocity $Re(u)$ and amplitudes of pulsations $|u|$ for all these modes computed for harmonically modulated flow with $a = -0.3$, $\alpha = 0.25$, $\beta = 0.6$. Symmetric and antisymmetric fundamental modes are shown in Figure 23 *a* and *b*, whereas Figure 23 *c* and *d* shows symmetric and antisymmetric subharmonic disturbances. For symmetric modes $|u|$ is largest at the minimums of basic flow velocity u_i, whereas maximal pulsations of antisymmetric modes coincides with maxima of gradients $|\partial u_i/\partial z|$. The phase velocity of symmetric modes coincides with TS wave velocity, but

antisymmetric disturbances propagate faster with $c = Re(\omega)/\alpha = 0.6$. Further computations reveals that the subharmonic mode is the most unstable one among the antisymmetric disturbances and the fundamental mode is the most amplified symmetric disturbance. So, only subharmonic antisymmetric and fundamental symmetric modes will be considered later. For brevity, these modes will be named as antisymmetric and symmetric ones.

Growth rates $\theta = Im(\omega)$ of symmetric and antisymmetric modes as functions of amplitude a and spanwise wavenumber β are shown in Figures 24 and 25 respectively. These results were computed for $\alpha = 0.25$; amplitude dependance of θ corresponds to $\beta = 0.6$, and $\theta(\beta)$ corresponds to $a = 0.3$. Growth rates of all modes increase with amplitude growth. For small amplitudes of flow inhomogeneity the symmetric modes are the most unstable, whereas antisymmetric disturbances becomes the most amplified for large amplitudes $a \geq 0.3$. The β- dependences of growth rates are different for symmetric and antisymmetric modes. Growth rates of symmetric modes are maximal for $\beta = 0$ and gradually decrease with growth of β. Amplification rates of antisymmetric disturbances initially increases with β growth, then reaches maximum at $\beta = 0.6$ and falls off. This result contradicts with conclusion of [10] about growth rate of these modes proportionality to $|\partial u_i/\partial z|$.

Figure 26 shows the growth rates of symmetric and antisymmetric modes as functions of reduced frequency $F = 10^6\omega/R$ computed in flow with $a = -0.3$ and $\beta = 0.6$. Both symmetric and antisymmetric disturbances amplify much rapidly then TS waves. The growth rates of these two types of modes are comparable, with symmetric modes are the most unstable at large frequency, whereas the antisymmetric modes are the most amplified low-frequency disturbances. Instability occurs in wide frequency range $20 \leq F \leq 220$ with maximal growth rate achieves at $F = 150$. Disturbances in the same frequency range amplified in the boundary layer flow with embedded streamwise vortices in experiment [10].

Stability localized inhomogeneity flow (3.6) with positive and negative amplitudes $a = \pm 0.3$ was studied in order to reveal the influence of width of inhomogeneity region on flow stability. For this purpose the stability of flow (3.6) with $q = 0.63$ and various β with respect to symmetric modes was computed. The results shown in Figure 27 demonstrates that the flow with high-speed streak has almost the same stability characteristics as homogeneous Blasius flow. In flow with low-speed streak the growth rates of disturbances remains the same as in Blasius flow if $\beta \geq 0.2$. The instability in this flow becomes remarkable only if $\beta \leq 0.2$, with growth rate of disturbances increases with β diminishing. It means that single thin streak does not destabilize flow in spite of inflexible velocity profile within it. The remarkable instability in this streak occurs only if it's width exceeds a threshold value $L^* \sim 7\delta^*$. This fact explains the absence of transition in boundary layer distorted by wake studied in section 2. Really, in all flow configurations tested, the width of distorted part of boundary layer did not exceeds the threshold value predicted by theory. It's interesting to note

that the harmonic modulation of small spanwise period $T_z \leq L^*$ ($\beta \geq 1$) leads to remarkable instability (see Figure 25). So, the periodically placed streaks are more dangerous that equal sole streak.

2.2. Receptivity of swept wing boundary layer to small outer flow inhomogeneity

In this section the response of boundary layer on the swept wing to the sinusoidal variations of outer flow velocity in spanwise direction is studied theoretically. Similar to straight wing, the flow inhomogeneity should amplify in boundary layer via Goldstein's vortex stretching mechanism. The resulting disturbances in boundary layer will be quite similar to steady cross-flow instability vortices, so these vortices should be generated. This is an additional mechanism of steady outer flow disturbances growth in swept wing boundary layer. The simple analytic theory describing amplification of outer flow inhomogeneity through the cross-flow instability modes generation is developed here.

2.2.1. Problem formulation

Consider the viscous incompressible fluid flow over the infinite swept wing. Scheme of flow configuration and coordinates systems used are shown in Figure 37. The outer flow is assumed to be unidirectional and it's velocity varies slightly along the span. Let's designate the chord of the wing as L, the mean value of outer flow velocity as U_∞ and the angle between the flow direction and chord as α (see Figure 37). The radius of the wing leading edge κL is assumed to be small with respect to chord, i.e. $\kappa \ll 1$. However, the wing thickness is not necessary small. Further we suppose, that the Reynolds number $R = U_\infty L/\upsilon$ is large enough for viscous effects been negligeable outside thin boundary layer. To describe flow the nondimensional variables are introduced using L and U_∞ as reference length and velocity. Two Cartesian coordinates systems shown in Figure 37 (x, y, z) and (ξ, η, z) will be used further. Origins and applicate axis z of both systems coincide. Abscisa axis x of first system coincides with outer flow direction, whereas abscisa axis of second one is directed along the chord of the wing. Components of vectors in these systems will be designated by subscripts x, y, z and ξ, η, z respectively.

Further we suppose that velocity vector $\mathbf{V}$ far upstream the leading edge ($\xi \to \infty$) is presented in form

$$\mathbf{V} = \{V_x, V_y, V_z\} \qquad V_x \to 1 + \epsilon u_\infty(y) \quad V_y = V_z \to 0 \quad \xi \to -\infty \qquad (2.7)$$

where $\epsilon \ll 1$ is small parameter and function $u_\infty(y)$ describes the velocity variation along the span. At the surface of the wing $z = z_s(\xi)$, the no-slip boundary conditions should be established

$$\mathbf{V}(\xi, \eta, z_s(\xi)) = 0 \qquad (2.8)$$

Boundary conditions (3.1), (3.2) together with Navier-Stokes equations describing the flow provides complete problem formulation. In contrast to work of Goldstein at al [4], only linear with respect to ϵ solution of this problem will be sought here.

2.2.2. Solution for inviscid flow

As was mentioned above, the flow around the wing is inviscid outside the thin boundary layer whose thickness is $\sim R^{-1/2}$. The solution for inviscid flow is sought in form

$$\mathbf{V} = \mathbf{U}_0 + \epsilon\mathbf{u}$$

where $\mathbf{U}_0$ is a potential basic flow around the wing corresponding to uniform outer stream and $\epsilon\mathbf{u}$ is a disturbance, generated by outer flow inhomogeneity. The disturbance is governed by linearized Eulier equations. The solution of this equations obtained in [13] can be specialized to present case to give

$$\mathbf{u} = \mathbf{u}^{(\mathrm{I})} + \nabla\varphi \tag{2.9}$$

$$\mathbf{u}^{(\mathrm{I})} = u_\infty(Y) \cdot \nabla\Delta(x, y, z) \tag{2.10}$$

$$\Delta\varphi = -(\nabla, \mathbf{u}^{(\mathrm{I})}) \tag{2.11}$$

$$(\nabla\varphi, \mathbf{n})|_{z=z_s(\xi,\eta)} = 0 \tag{2.12}$$

Here Y is an integral of equation for streamlines of basic flow

$$\frac{dx}{U_{0x}} = \frac{dy}{U_{0y}} = \frac{dz}{U_{0z}}$$

such, that $Y \to y$ as $\xi \to -\infty$, and $\Delta(x, y, z)$ is Laighill's [2] drift function

$$\Delta(x, y, z) = x + \int_{-\infty}^{x} \left[\frac{1}{U_{0x}(x', y(x'), z(x'))} - 1\right] dx'$$

Integration here is performed along a streamline of basic flow passing through point x, y, z. The difference of drift function between any two points on a streamline is equal to the time it takes a fluid particle to transverse the distance between those points.

For subsequent consideration it is more convenient to use coordinates (ξ, η, z) fitted to wing chord. In these coordinates the drift function takes form

$$\Delta = \eta \sin\alpha + \Delta_\perp(\xi, z)$$

where

$$\Delta_\perp(\xi, z) = \xi + \int_{-\infty}^{\xi} \left[\frac{\cos\alpha}{U_{0\xi}} - 1 \right] d\xi' \tag{2.13}$$

is the drift function corresponding to flow around straight wing with outer flow velocity equals 1. To find integral Y, let's relate dy with $d\xi$ for displacement along the streamline. Bearing in mind relationship

$$d\eta = \frac{U_{0\eta}}{U_{0\xi}} d\xi = \frac{\sin\alpha}{U_{0\xi}} d\xi$$

we find

$$dy = \cos\alpha d\eta - \sin\alpha d\xi = \sin\alpha \left[\frac{\cos\alpha}{U_{0\xi}} - 1 \right] d\xi$$

Integration of this along streamline provides the expression for Y

$$Y = \lim_{\xi \to -\infty} y(\xi, \eta(\xi), z(\xi)) = \eta\cos\alpha - \Delta_\perp(\xi, z)\sin\alpha \tag{2.14}$$

Substitution of this into (3.4) and (3.5) gives the expression for $\mathbf{u^{(I)}}$ and equation for φ in coordinates (ξ, η, z)

$$u_\eta^{(I)} = u_\infty(Y)\sin\alpha \qquad \mathbf{u}_\perp^{(I)} = u_\infty(Y)\nabla_\perp\Delta_\perp\cos\alpha \tag{2.15}$$

$$\frac{\partial^2\varphi}{\partial\eta^2} + \nabla_\perp^2\varphi = -u_\infty(Y)\cdot\nabla_\perp^2\Delta_\perp\cos\alpha - u_\infty'\left[1 - (\nabla_\perp\Delta_\perp)^2\right]\sin\alpha\cos\alpha \tag{2.16}$$

where $\mathbf{u}_\perp^{(I)} = \left\{u_\xi^{(I)}, u_z^{(I)}\right\}$ and $\nabla_\perp = \left\{\frac{\partial}{\partial\xi}, \frac{\partial}{\partial z}\right\}$ are projections of $\mathbf{u}^{(I)}$ and three-dimensional operator ∇ onto (ξ, η) plane.

Further we introduce the ortohonal coordinate system (s, η) associated with streamlines of potential flow around the wing

$$s = \int_0^\Phi \frac{d\Phi}{\sqrt{U^2 + W^2}|_{\Psi=const}} \qquad \eta = \int_0^\Psi \frac{d\Psi'}{\sqrt{U^2 + W^2}|_{\Phi=const}}$$

where

$$U = \frac{U_{0x}}{\cos\alpha} = \frac{\partial\Phi}{\partial\xi} = \frac{\partial\Psi}{\partial z} \qquad W = \frac{U_{0z}}{\cos\alpha} = \frac{\partial\Phi}{\partial z} = -\frac{\partial\Psi}{\partial\xi}$$

and $\Psi = 0$ at the wing surface and $\Phi = 0$ in the stagnation point. For Jacobian $\mathbf{I} = \|\partial(s,\eta)/\partial(\xi,\eta)\| \equiv 1$, the expression (3.9),equation for φ (3.10) and operator $\nabla_\perp$ remain unchanged upon the coordinates transformation. However, boundary conditions at the surface (3.6) become more simple

$$\frac{\partial\varphi}{\partial\eta}(s, 0) = 0 \tag{2.17}$$

Solution for potential φ will be sought in form

$$\varphi = \varphi' + \tilde{\varphi} \qquad \varphi' = \cot\alpha \int u_\infty(Y)dY$$

Substitution of this into (3.10), (3.11) gives the following problem for $\tilde{\varphi}$

$$\begin{array}{c} \frac{\partial^2\tilde{\varphi}}{\partial\eta^2} + \nabla_\perp^2\tilde{\varphi} = (1-\cot^2\alpha)\,u'_\infty(Y)\sin\alpha\cos\alpha \\ \frac{\partial\tilde{\varphi}}{\partial n}(s,0) = 0 \end{array} \tag{2.18}$$

Our task is the finding the solution at the wing surface. To do this let's find the asymptotic behavior of $\Delta_\perp$ as $n \to 0$. At first the expression for $\Delta_\perp$ in coordinates (Φ, Ψ) should be found. For this purpose we relate $d\Phi$ and $d\xi$ for displacement along the streamline as

$$d\Phi = \frac{\partial\Phi}{\partial\xi}d\xi + \frac{\partial\Phi}{\partial z}dz = Ud\xi + Wdz = \frac{U^2+W^2}{U}d\xi$$

substitution of this into (3.7) gives

$$\Delta_\perp(\Phi,\Psi) = \Phi + \widetilde{\Delta_0}(\Psi) - \int_\Phi^\infty \left[\frac{1}{U^2+W^2} - 1\right] d\Phi$$

where

$$\widetilde{\Delta_0}(\Psi) = \int_{-\infty}^{+\infty} \left[\frac{1}{U^2+W^2} - 1\right] d\Phi$$

as shown in [4], $\widetilde{\Delta_0}(\Psi)$ becomes singular near the wall as

$$\widetilde{\Delta_0}(\Psi) \sim -r\ln\Psi + \widetilde{\Delta_{00}}(\Psi) \qquad \Psi \to 0$$

where r is radius of leading edge and $\widetilde{\Delta_{00}}(\Psi)$ remains bounded as $\Psi \to 0$. So, the drift function within the wall behaves as

$$\Delta_\perp \to -\frac{\kappa}{a}\ln n + \Delta_0(s) \qquad n \to 0$$

where

$$\Delta_0(s) = \Phi - \int_\Phi^\infty \left[\frac{1}{U_0^2} - 1\right]_{\Psi=0} d\Phi - \frac{\kappa}{a}\ln U_0 + const$$

Here $U_0(s)$ is velocity at the wall, a is constant depending from the shape of the profile of wing. From this result and (3.8) it follows that

$$Y \to \eta\cos\alpha + \frac{\kappa}{a}\ln n\sin\alpha - \Delta_0(s)\sin\alpha \qquad n \to 0 \tag{2.19}$$

With this asymptotic of Y in hand one can easily show that solution of (3.12) within the wall appears in form

$$\tilde{\varphi} \to n^2 F(s,\eta,Y) \qquad n \to 0$$

where F remains bounded when $n \to 0$. So, $\nabla\tilde{\varphi}$ vanishes as $n \to 0$, and the solution for velocity of disturbance near the wall in accordance with (3.3), (3.9), (3.12) becomes

$$u_s \sim u_\infty(Y)\frac{\partial\Delta_\perp}{\partial s}\cos\alpha + \frac{\partial\varphi'}{\partial s} \to 0$$

$$u_\eta \sim u_\infty(Y)\sin\alpha + \frac{\partial\varphi'}{\partial\eta} \to \frac{1}{\sin\alpha}u_\infty(y) \qquad \text{as } n \to \infty$$

$$u_n \to 0$$

Finally, we have following expressions for components of complete velocity vector $\mathbf{V}$ near the wall

$$V_s \to U_0(s)\cos\alpha; \qquad V_\eta \to \sin\alpha + \epsilon\frac{u_\infty(Y)}{\sin\alpha}; \qquad V_n \to 0 \qquad \text{as } n \to 0 \quad (2.20)$$

2.2.3. The boundary layer solution

Near the wall the boundary layer of thickness $\sim R^{-1/2}$ should be introduced to fit no-slip boundary conditions. In this layer we shall use the rescaled normal to wall coordinate $Z = n\sqrt{R}$ and notations u, v, w for velocity components along s, η and n axis. Due to problem linearity, the boundary layer solution will be sought in form

$$u = u_0(s, Z) + \epsilon\tilde{u}(s, \eta, Z)$$

$$v = v_0(s, Z) + \epsilon\tilde{v}(s, \eta, Z)$$

$$w = \frac{1}{\sqrt{R}}w_0(s, Z) + \epsilon\tilde{w}(s, \eta, Z)$$

$$p = p_0(s, Z) + \epsilon\tilde{p}(s, \eta, Z)$$

where basic flow u_0, v_0, w_0 and p_0 correspond to boundary layer in the homogeneous stream and $\tilde{u}$, $\tilde{v}$, $\tilde{w}$, $\tilde{p}$ describe perturbations of velocity and pressure introduced by outer flow inhomogeneity. Basic flow is described by conventional Prandtl equations with boundary conditions

$$u_0(s,0) = v_0(s,0) = w_0(s,o) = 0; \qquad u_0(\infty) = U_0(s)\cos\alpha \qquad v_0(\infty) = \sin\alpha$$

Disturbances obey the linearized Navier-Stokes equations with boundary conditions following from (3.13), (3.14)

$$\tilde{u},\ \tilde{v},\ \tilde{w}(s,\eta,0) = 0$$

$$\tilde{u}(s,\eta,z) \to 0;$$

$$\tilde{v}(s,\eta,z) \to \tfrac{1}{\sin\alpha}u_\infty\left(\eta\cos\alpha + \left(\tfrac{\kappa}{a}\ln Z - \Delta_0(s) - \tfrac{\kappa}{a}\ln R\right)\sin\alpha\right) \qquad \text{as } Z \to \infty$$

For the sake of simplicity, the sinusoidal flow inhomogeneity of form

$$u_\infty(y) = e^{i\tilde{\beta}\sqrt{R}y} \tag{2.21}$$

will be considered further. The period of inhomogeneity is assumed to be of the same order as the spanwise period of cross-flow instability vortices, so $\tilde{\beta}$ is assumed to be of order of 1.

To meet the boundary conditions (3.15), (3.16) the solution for disturbances of velocity and pressure will be sought in form

$$\left\{ \begin{array}{c} \tilde{u} \\ \tilde{v} \\ \tilde{w} \\ \tilde{p} \end{array} \right\} = \left\{ \begin{array}{c} \hat{u} \\ \hat{v} \\ \hat{w} \\ \hat{p} \end{array} \right\} (s, Z) e^{i\sqrt{R}(\chi(s)+\beta\eta)} \tag{2.22}$$

where $\chi(s) = -\tilde{\beta}(\Delta_0(s) + \frac{\kappa}{a}\ln R)\sin\alpha$, $\beta = \tilde{\beta}\cos\alpha$. From (3.15), (3.16) it follows that amplitudes $\hat{u}$, $\hat{v}$, $\hat{w}$ should satisfy the boundary conditions

$$\hat{u}(s,0) = \hat{v}(s,0) = \hat{w}(s,0) = \hat{u}(s,\infty) = 0 \qquad \hat{v}(s,z) \to \frac{1}{\sin\alpha} e^{i\mu \ln Z} \qquad Z \to \infty \tag{2.23}$$

where $\mu = \frac{\tilde{\beta}\kappa\sqrt{R}}{a}\sin\alpha$.

The disturbances (3.17) are the products of amplitudes $\hat{u}$, $\hat{v}$, $\hat{w}$, $\hat{p}$, which vary relatively slowly with s to fast oscillating exponent. When they are substituted into linearized Navier-Stokes equations the terms of order of R, $\sqrt{R}$ and 1 appear. If the terms of order of 1 were neglected and pressure is eliminated from equations, then the following equations for amplitudes of velocity are obtained

$$\mathbf{L}(\overline{\alpha})\circ\hat{w} + \delta(\mathbf{M}(\overline{\alpha})\circ\hat{w} + \mathbf{N}(\overline{\alpha})\circ\frac{\partial\hat{w}}{\partial s} + \mathbf{K}(\overline{\alpha})\circ\hat{u}) = 0; \qquad \delta = R^{-1/2} \tag{2.24}$$

$$i\overline{\alpha}\hat{u} + i\beta\hat{v} + \delta\frac{\partial\hat{u}}{\partial s} = 0$$

Here

$$\mathbf{L}(\overline{\alpha}) = (i\overline{\alpha}u_0 + i\beta v_0)\cdot\left(\frac{\partial^2}{\partial Z^2} - \gamma^2\right) - \left(i\overline{\alpha}\frac{\partial^2 u_0}{\partial Z^2} + i\beta\frac{\partial^2 v_0}{\partial Z^2}\right) - \frac{1}{\sqrt{R}}\left(\frac{\partial^2}{\partial Z^2} - \gamma^2\right)^2$$

$$\mathbf{N}(\overline{\alpha}) = u_0\left(\frac{\partial^2}{\partial Z^2} - \gamma^2\right) - \frac{\partial^2 u_0}{\partial Z^2} + 2i\alpha\,(i\overline{\alpha}u_0 + i\beta v_0) \tag{2.25}$$

and $\overline{\alpha} = \frac{\partial\chi}{\partial s}$, $\gamma^2 = \overline{\alpha}^2 + \beta^2$. Expressions for operators $\mathbf{M}(\overline{\alpha})$, $\mathbf{K}(\overline{\alpha})$ describing the effect of flow nonparallelity will not be used further, hence they are omitted here.

Solution of (3.19) with boundary conditions (3.18) will be sought as a sum

$$\left\{ \begin{array}{c} \widehat{u} \\ \widehat{v} \\ \widehat{w} \end{array} \right\} = \left\{ \begin{array}{c} 0 \\ \widehat{v}_r \\ \widehat{w}_r \end{array} \right\}(z) + \left\{ \begin{array}{c} \widehat{u}_0 \\ \widehat{v}_0 \\ \widehat{w}_0 \end{array} \right\}(s, Z) \tag{2.26}$$

where augend fits the boundary conditions (3.18) and addend satisfy the homogeneous boundary conditions

$$\widehat{u}_0(s,0) = \widehat{v}_0(s,0) = \widehat{w}_0(s,0) = \widehat{u}_0(s,\infty) = \widehat{v}_0(s,\infty) = 0 \tag{2.27}$$

One of possible forms of augend in (3.21) is

$$\widehat{v}_r = \frac{H(Z)}{\sin\alpha} e^{i\mu \ln Z} \qquad \widehat{w}_r = -\frac{i\beta}{\sin\alpha} \int_0^Z H(Z') e^{i\mu \ln Z'} dZ'$$

where $H(Z)$ is an arbitrary function filling the following requirements

$$H(Z) \to 1, \quad Z \to \infty; \qquad H(Z)/Z^3 \to const \quad Z \to 0$$

This choice permits us to satisfy continuity equation for $\widehat{v}_r$, $\widehat{w}_r$ and ensures that $\widehat{w}_r$, $\widehat{w}_r'$, $\widehat{w}_r''$, $\widehat{w}_r'''$ and $\widehat{w}_r^{IV}$ are finite as $Z \to 0$.

Substitution of (3.21) into (3.20) gives the following problem for $\widehat{u}_0$, $\widehat{v}_0$, $\widehat{w}_0$

$$\mathbf{L}(\overline{\alpha})\circ\widehat{w}_0 + \delta(\mathbf{M}(\overline{\alpha})\circ\widehat{w}_0 + \mathbf{N}(\overline{\alpha})\circ\frac{\partial \widehat{w}_0}{\partial s} + \mathbf{K}(\overline{\alpha})\circ\widehat{u}_0) = -\mathbf{L}(\overline{\alpha})\circ\widehat{w}_r - \delta\mathbf{M}(\overline{\alpha})\circ\widehat{w}_r \tag{2.28}$$

To solve it, let's suppose that $\overline{\alpha}$ is close to eigenvalue of Orr-Sommerfeld equation α_0, corresponding to steady cross-flow instability mode. Physically, it means that the direction of cross-flow instability vortex is close to the streamline of undisturbed flow at the outer edge of boundary layer. Introducing small parameter θ we write

$$\overline{\alpha} = \alpha_0 + \theta\Delta(s); \qquad \Delta(s) \sim 1$$

In this case the Orr-Sommerfeld operator $\mathbf{L}(\overline{\alpha})$ may be presented in form

$$\mathbf{L}(\overline{\alpha}) = \mathbf{L}(\alpha_0) + \theta\frac{\partial \mathbf{L}}{\partial \alpha}(\alpha_0) \cdot \Delta(s)$$

and (3.23) becomes

$$\left[\mathbf{L}(\alpha_0) + \theta\Delta\tfrac{\partial \mathbf{L}}{\partial \alpha}(\alpha_0) + \delta\mathbf{M}(\alpha_0)\right]\circ\widehat{w}_0 + \delta\mathbf{N}(\alpha_0)\circ\tfrac{\partial \widehat{w}_0}{\partial s} + \delta\mathbf{K}(\alpha_0)\circ\widehat{u}_0 + O(\theta\delta) + O(\theta^2) =$$

$$-\mathbf{L}(\overline{\alpha})\circ\widehat{w}_r - \delta\mathbf{M}(\overline{\alpha})\circ\widehat{w}_r$$

If we assume that $\theta \gg \delta$ the solution of this equation may be sought in the frame of multi-scale method as

$$\widehat{w}_0 = \frac{1}{\theta} A(X)\Phi(s,Z) + w_1(s,Z) \qquad X = \frac{1}{\lambda}s \qquad \lambda = \frac{\delta}{\theta} \ll 1 \tag{2.29}$$

where $\Phi(s,Z)$ is an eigenfunction of Orr-Sommerfeld equation corresponding to eigenvalue α_0. Substituting this into (3.22) and retaining only $O(\theta)$ terms we obtain

$$\mathbf{L}(\alpha_0) \circ w_1 = -\mathbf{L}(\alpha_0) \circ \widehat{w}_r - \Delta A \frac{\partial \mathbf{L}}{\partial \alpha}(\alpha_0) \circ \Phi - \frac{dA}{dX}\mathbf{N}(\alpha_0) \circ \Phi$$

This equation for w_1 has solution only if right part of it is **orthogonal** to eigenfunction Φ^+ of adjoint to $\mathbf{L}(\alpha_0)$ operator. The **orthogonality** condition provides the following equation for amplitude $A(X)$

$$\frac{dA}{dX} - i\Delta(\lambda X) \cdot A = P(\lambda X)$$

where

$$P(\lambda X) = -\frac{\langle \Phi^+, \mathbf{L}(\alpha_0) \circ \widehat{w}_r \rangle}{\langle \Phi^+, \mathbf{N}(\alpha_0) \circ \Phi \rangle}$$

and $\langle \Psi, \Phi \rangle \equiv \int_0^\infty \Psi \Phi dZ$ is a definition of scalar product.
It may be easily shown, that general solution of this equation is

$$A = ae^{i\Theta(X)} + i\frac{P}{\Delta} + O(\lambda); \qquad \frac{d\Theta}{dX} = \Delta(\lambda X) \tag{2.30}$$

where a is constant depending from initial condition. To formulate this condition, let's suppose that near the leading edge the difference $\overline{\alpha} - \alpha_0$ becomes finite, so $|\Delta(s)|$ becomes $\sim 1/\theta$ when s becomes small. Here scaling (3.24) becomes unsuitable and $\widehat{w}_0 \sim 1$ or $A \sim \theta$ should be written instead of it. So, if we want to match the solution (3.25) with solution near the leading edge we must to write

$$A \sim O(\theta) \sim a + iP \cdot O(\theta)$$

From here we have an estimate $a \sim O(\theta)$, so first term in (3.25) may be neglected and finite expression for amplitude becomes

$$A = i\frac{P}{\Delta}$$

So, the expression for $\widehat{w}$ in ordinary boundary layer variables is

$$\widehat{w} = i\frac{P(s)}{\overline{\alpha} - \alpha_0}\Phi(s,Z) + O(\overline{\alpha} - \alpha_0)$$

This expression is valid for $R^{-1/2} \ll |\overline{\alpha} - \alpha_0| \ll 1$. If $|\overline{\alpha} - \alpha_0|$ becomes $\sim R^{-1/2}$ the effect of flow **nonparallelism** should be taken into account.

Results obtained reveals that boundary response on outer flow inhomogeneity is inversely proportional to difference $\overline{\alpha} - \alpha_0$. To estimate this difference we shall use the generalized Faulkner-Scan (F-S) self-similar flow as a simple model of boundary layer flow at real swept wing. This flow corresponds to outer flow velocity distribution

$$U_0 = s^m \cos\alpha \qquad V_0 = \sin\alpha$$

and is defined as

$$u_0 = s^m F'\left(\frac{Z}{\delta}\right)\cos\alpha \qquad v_0 = G'\left(\frac{Z}{\delta}\right)\sin\alpha \qquad \delta = \left(\frac{2}{m+1}\right)^{1/2} R^{-1/2} s^{\frac{1-m}{2}}$$

where functions F and G are solutions of boundary value problem for ordinary differential equations

$$F''' + FF'' + \tfrac{2m}{m+1}\left(1 - F'^2\right) = 0 \qquad G''' + FG' = 0$$
$$F(0) = F'(0) = 0 \quad F'(\infty) = 1 \qquad G(0) = G'(0) = 0 \quad G'(\infty) = 1$$

Of course, real flow over the wing should be approximated by F-S Flow with exponent m varying with s. Immediately at the nose the flow near stagnation point with $m = 1$ occurs, than flow acceleration becomes weaker and m gradually diminishes to zero. After the point of minimum static pressure, the flow begins to retard and m becomes negative. So, to estimate the difference $\overline{\alpha} - \alpha_0$ over all wing surface, it should be computed for F-S flow with various m. Results of such computations made for $R = 1000$, $\alpha = \pi/4$, $s = 1$ and several values of $\beta = 0.2,\ 0.4\ , 0.6$ are presented in Figure 38. The real part of difference $\overline{\alpha} - \alpha_0$ and it's absolute value as functions of m are plotted by solid and dashed lines in this Figure. For all values of spanwise **wavenumber** $Re(\overline{\alpha} - \alpha_0)$ is positive for positive m and negative if m is negative. As m tends to zero $Re(\overline{\alpha} - \alpha_0)$ goes to zero. Due to imaginary part of α_0 **being** small $\sim 10^{-3}$ and $\overline{\alpha}$ real, the absolute value of $\overline{\alpha} - \alpha_0$ is predominantly defined by it's real part. So, $|\overline{\alpha} - \alpha_0|$ becomes small enough as m tends to zero. Unfortunately, cross-flow instability modes do not exist for $m = 0$, so the value of $\overline{\alpha} - \alpha_0$ is not defined in this point and minimum of $|\overline{\alpha} - \alpha_0|$ could not be found at all. However, for smallest values of $m = \pm 0.001$, where computations were performed the absolute values $|\overline{\alpha} - \alpha_0|$ were about $2 \cdot 10^{-3}$, so the boundary layer distortion may be about 500 times **greater** then oncoming flow inhomogeneity.

In real flow over the wing, the boundary layer velocity profiles with $m \sim 0$ correspond to flow around pressure minimum. So, the maximal boundary layer distortion should occur near the minimum of static pressure distribution over wing profile. **However,** this conclusion is quite preliminary due to crudeness of F-S flow model. More realistic prediction of boundary layer distortion may be reached by means of solution of (3.23) in the boundary layer over real wing using PSE-method.

3. Conclusions

1. Large volume of averaged (steady) and pulsational flow characteristics of boundary layer/free stream inhomogeneity interaction have been measured with plates of different nose shapes and for different free stream inhomogeneities. Flow inhomogeneities were created by the wakes behind one or several wires stretched normal to leading edge.

2. It was found, in a qualitative agreement with Goldstein's theory [4,6], that the deformation of normal to the plate vorticity by the flow around the leading edge may be the cause of streamwise vortices (streaks) formation observed in the presence of free-stream turbulence.

3. The vortex stretching in course of this deformation leads to significant amplification of disturbances in boundary layer.

4. Three different regimes of single wire wake/boundary layer interaction were discovered: linear, symmetric nonlinear and antisymmetric nonlinear ones. The regimes are distinguished by different character of downstream amplification of disturbances and different spanwise disturbances distribution. The antisymmetric regime is the most unexpected as antisymmetric spanwise distribution of disturbances in boundary layer takes place for symmetric upstream boundary conditions.

5. The increase of wake velocity deficit and decrease of wake width lead to transformation of distortion from linear to symmetric nonlinear and then to antisymmetric nonlinear regime. The criterion for transition to antisymmetic regime was introduced.

6. Distortion of velocity profile in the boundary layer for nonlinear regimes have maximum close to leading edge. This maximum may be the cause of early (bypass) laminar-turbulent transition. If not, the distortion then decreases downstream due to viscous dissipation and becomes smaller then gradually increasing distortion for linear regime.

7. The vortex lines stretching and hence disturbance amplification increase with increase of plate nose radius.

8 Interaction of several wakes generated by a set of wires intensify the processes caused by single wake.

9. The wake/boundary layer interaction properties investigated here simulate/reflect boundary layer processes caused by low frequency vorticity of free-stream turbulence.

10. The results obtained permit to suppose that the shape of leading edge should have noticeable influence on laminar-turbulent transition caused by outer flow turbulence/inhomogeneities. Transition Reynolds number for blunt nose body may be few times smaller than those observed in well-known experiments [9-11] performed with sharp leading edge plates. This difference caused not so much by different pressure distribution but by different stretching of vortex lines by flow around leading edge.

11. The stability of steady spanwise-modulated flow was studied theoretically. This flow is a model of streaks found in experiments of Kendall et al [9-11] at high free-stream turbulence level. It was shown, that one isolated streak is more stable then periodically placed streaks of the same shape. The isolated streak does not destabilize flow at all if it is **narrower** then threshold value of $\sim 7\delta^*$. Experiment described in Part I shows that laminar-turbulent transition in periodically modulated boundary layer distorted by the wake from a set of wires really occurred earlier then in a boundary layer distorted by single wire wake.

12. The response of boundary layer on the swept wing to the sinusoidal variations of outer flow velocity in spanwise direction was studied theoretically. In addition to Goldstein's vortex line stretching mechanism, the amplification of outer flow inhomogeneity in boundary **layer through the cross-flow instability mode** generation was found. This phenomenon may lead to extremely high receptivity of swept wing boundary layer to outer flow vorticity.

13. Understanding of streaks formation and their structure opens the hope of control the laminar-turbulent transition caused by outer flow vortical disturbances.

References

[1] Bushnell, D. Viscous drag reduction in aeronautics, *ICAS'94 Proceedings, Anaheim, USA, September 18-23, 1993*

[2] Breuer, K.S. & Landahl, M.T. The evolution of localized disturbances in a laminar boundary layer. Part 2. Strong disturbances, *J. Fluid Mech.*,1990,v. 220, 595-621.

[3] Butler K. M.O.& Farrel B.F. Three-dimensional optimal perturbations in viscous shear flows, *Phys. Fluids, 1992, A,* **4**, 1637-1650.

[4] Goldstein M.E., Leib S.I., Couley S.J. Distortion of a flat plate boundary layer by free-stream vorticity normal to the plate. *J. Fluid Mech.,1992,* v. 237, p.231-260.

[5] Goldstein M.E., Leib S.I. A note on the distortion of flat-plate boundary layer by free-stream vorticity normal to the plate. *J. Fluid Mech.,1993,* v. 248, p.531-541.

[6] Goldstein M.E. On the environmental realizability of algebraically growing disturbances and their relation to Klebanoff modes. *Presented at Florida State University International Symposium on Theoretical and Computational Fluid Dynamics in honor of Sir James Lighthill.*

[7] Crow S.C. Stability theory for a pair of trailing vortices. *AIAA paper* 90-1504, 1990

[8] Mansy H.,Yang P.M., Williams D.R. Quantitative measurements of three-dimensional structures in the wake of a circular cylinder. *J. Fluid Mech.*, 1994, V.270, pp.277-296.

[9] Kendall J.M. Experimental study of disturbances produced in a pre-transitional laminar boundary layer by weak free-stream turbulence. *AIAA paper* 85-1695, 1985

[10] Bakchinov, A.A., Grek, G.R., Klingmann, B.G.B., Kozlov, V.V. (1995) Transition experiments in a boundary layer with embedded streamwise vortices, *Phys. Fluids,* v. **7**, pp. 820-832.

[11] Kendall J.M. (1990) Boundary layer receptivity to freestream turbulence, *AIAA paper* #90-1504.

[12] Andersson P., Bergeron M., Henningson D.S. (1998) Optimal disturbances and bypass transition in boundary layers, *Submitted to Phys. Fluids.*

[13] Goldstein M.E. (1978) Unsteady vortical and entropic distortions of potential flows round arbitrary obstacles, *J. Fluid Mech.,* v.89, part 3, pp. 433-468.

Table

number of configu ration	num- ber of plate	num ber of wires	U	d [mm]	L [mm]	u_0	b [mm]	R_d	R_1	regime (sec*)	K	K_v	x* [mm]
1	1	1	17	0.09	40	0.056	0.46	106	$1.17\cdot10^6$	a. s.	0.15	$3.9\cdot10^{-5}$	--
2	1	1	17	0.09	250	0.032	0.88	106	$1.17\cdot10^6$	s	0.045	$1.17\cdot10^{-3}$	--
3	1	1	17	0.09	720	0.020	1.66	106	$1.17\cdot10^6$	l	0.015	$3.9\cdot10^{-4}$	--
4	2	1	17	0.09	40	0.055	0.46	106	$1.17\cdot10^6$	a.s	0.30	$5.6\cdot10^{-3}$	--
5	2	1	17	0.09	150	0.039	0.73	106	$1.17\cdot10^6$	tr	0.133	$2.5\cdot10^{-3}$	--
6	2	1	17	0.09	250	0.032	0.88	106	$1.17\cdot10^6$	s.	0.09	$1.7\cdot10^{-3}$	--
7	2	1	17	0.09	500	0.023	1.27	106	$1.17\cdot10^6$	l	0.046	$8.5\cdot10^{-4}$	--
8	2	1	17	0.09	725	0.020	1.66	106	$1.17\cdot10^6$	l	0.030	$5.6\cdot10^{-4}$	--
9	3	1	17	0.09	40	0.055	0.46	106	$1.17\cdot10^6$	a. s.	0.64	$8.1\cdot10^{-3}$	--
10	3	1	17	0.09	250	0.032	0.88	106	$1.17\cdot10^6$	tr	0.191	$2.4\cdot10^{-3}$	--
11	3	1	17	0.09	725	0.020	1.66	106	$1.17\cdot10^6$	l	0.064	$8.13\cdot10^{-4}$	400
12	4	1	17	0.09	40	0.055	0.46	106	$1.17\cdot10^6$	a.s.	1.20	$1.1\cdot10^{-2}$	75
13	4	1	17	0.09	150	0.039	0.73	106	$1.17\cdot10^6$	s	0.538	$5.0\cdot10^{-3}$	75
14	4	1	17	0.09	250	0.032	0.88	106	$1.17\cdot10^6$	s	0.360	$3.4\cdot10^{-3}$	250
15	2	1	5	0.3	40	0.109	1.07	104	$3.45\cdot10^5$	a.s	0.255	$6.7\cdot10^{-3}$	--
16	2	1	5	0.3	100	0.073	1.33	104	$3.45\cdot10^5$	s	0.137	$3.6\cdot10^{-3}$	--
17	2	1	5	0.3	200	0.040	1.87	104	$3.45\cdot10^5$	s	0.053	$1.4\cdot10^{-3}$	--
18	2	1	5	0.09	10	0.13	0.284	31	$3.45\cdot10^5$	s	1.13	$2.9\cdot10^{-2}$	--
19	2	1	5	0.09	40	0.064	0.567	31	$3.45\cdot10^5$	s	0.282	$7.36\cdot10^{-3}$	--
20	1	5	17	0.09	40	0.055	--	106	$1.17\cdot10^6$	--	--	--	--
21	1	5	17	0.09	725	0.02	--	106	$1.17\cdot10^6$	--	--	--	--
22	2	5	17	0.09	725	0.02	--	106	$1.17\cdot10^6$	--	--	--	400
23	3	5	17	0.09	40	0.055	--	106	$1.17\cdot10^6$	--	--	--	100

* regimes of interaction: l - linear, s - symmetric nonlinear, a.s - antisymmetric nonlinear

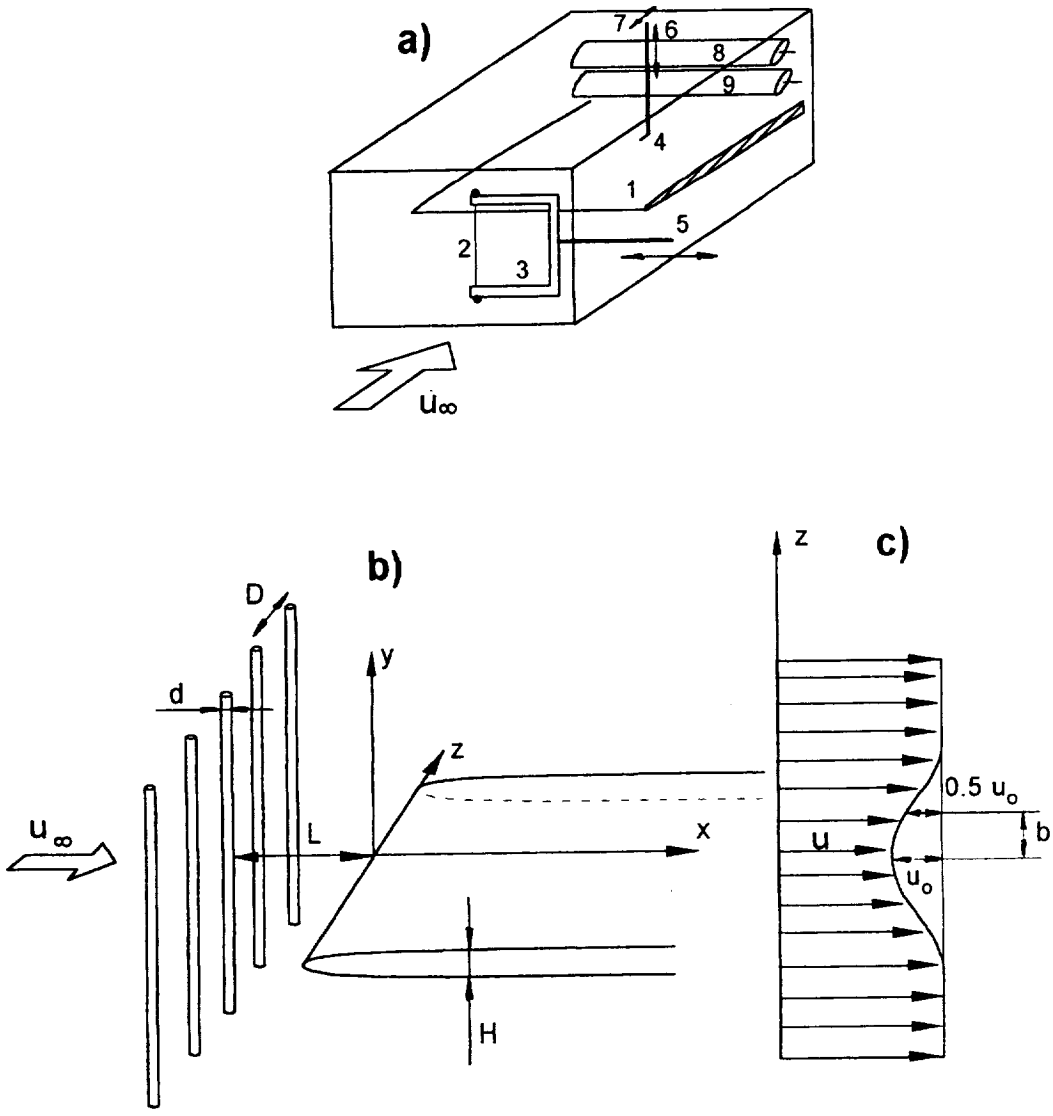

Figure 1. (a) - experimental setup: 1 - plate, 2 - wire(s), 3 - wire holder, 4 - probe, 5 - wire holder movement, 6,7 - probe movement, 8,9 - flaps.
(b) - coordinate system and general designations.
(c) - parameters of single wire wake: u_o - velocity deficit, b - half- width.

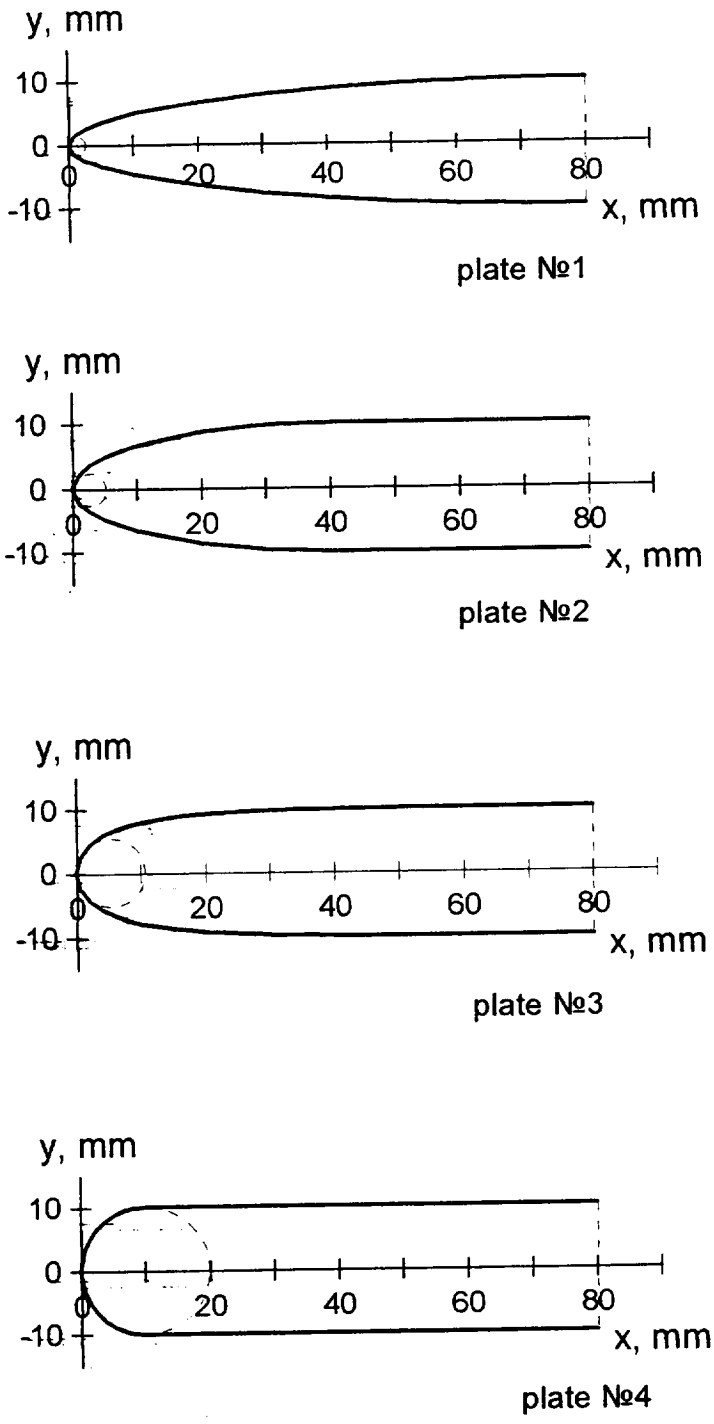

Figure 2. Contours of leading edges of plates № 1 - 4

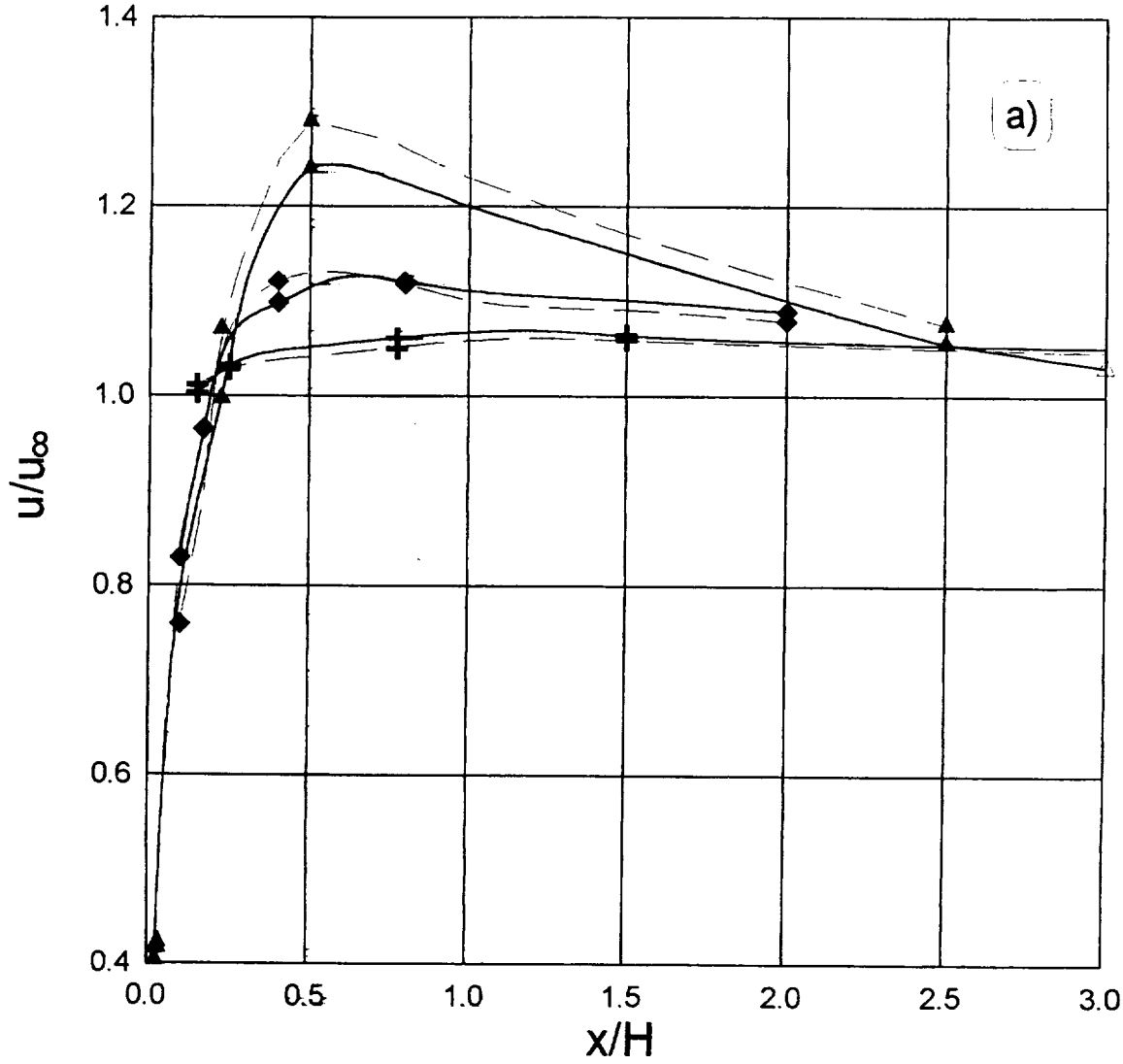

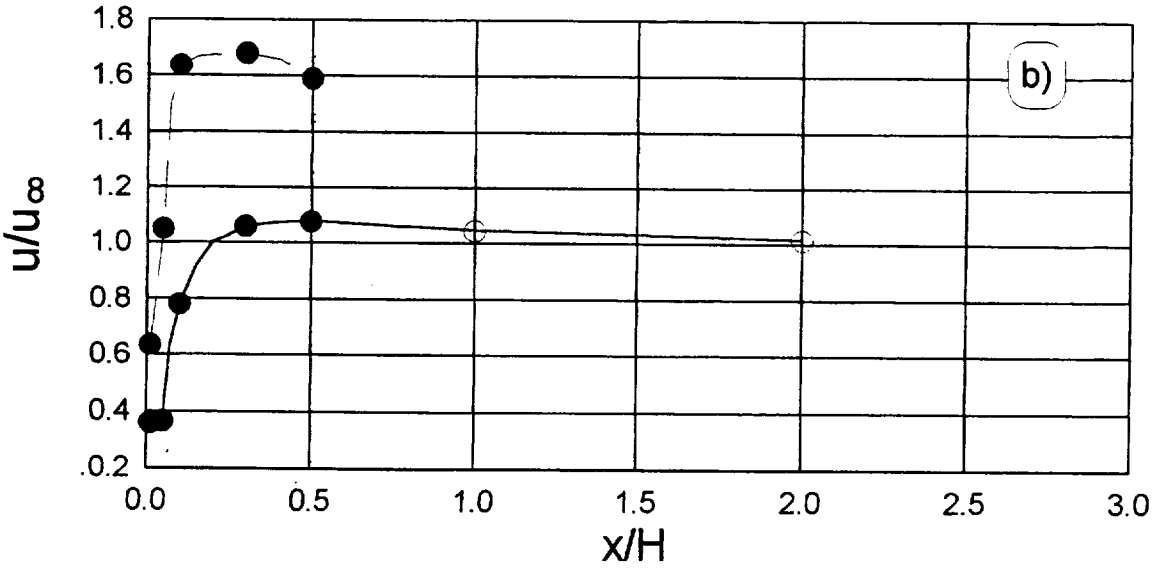

Figure 3. Velocity distribution over upper (——) and lower (- - -) sides of nose.

a) - symmetric flow over plates № 1 - 3; plate № 1 (✚); plate № 2 (◆); plate № 3 (▲);
b) - non-symmetric flow over plate № 4 (●)

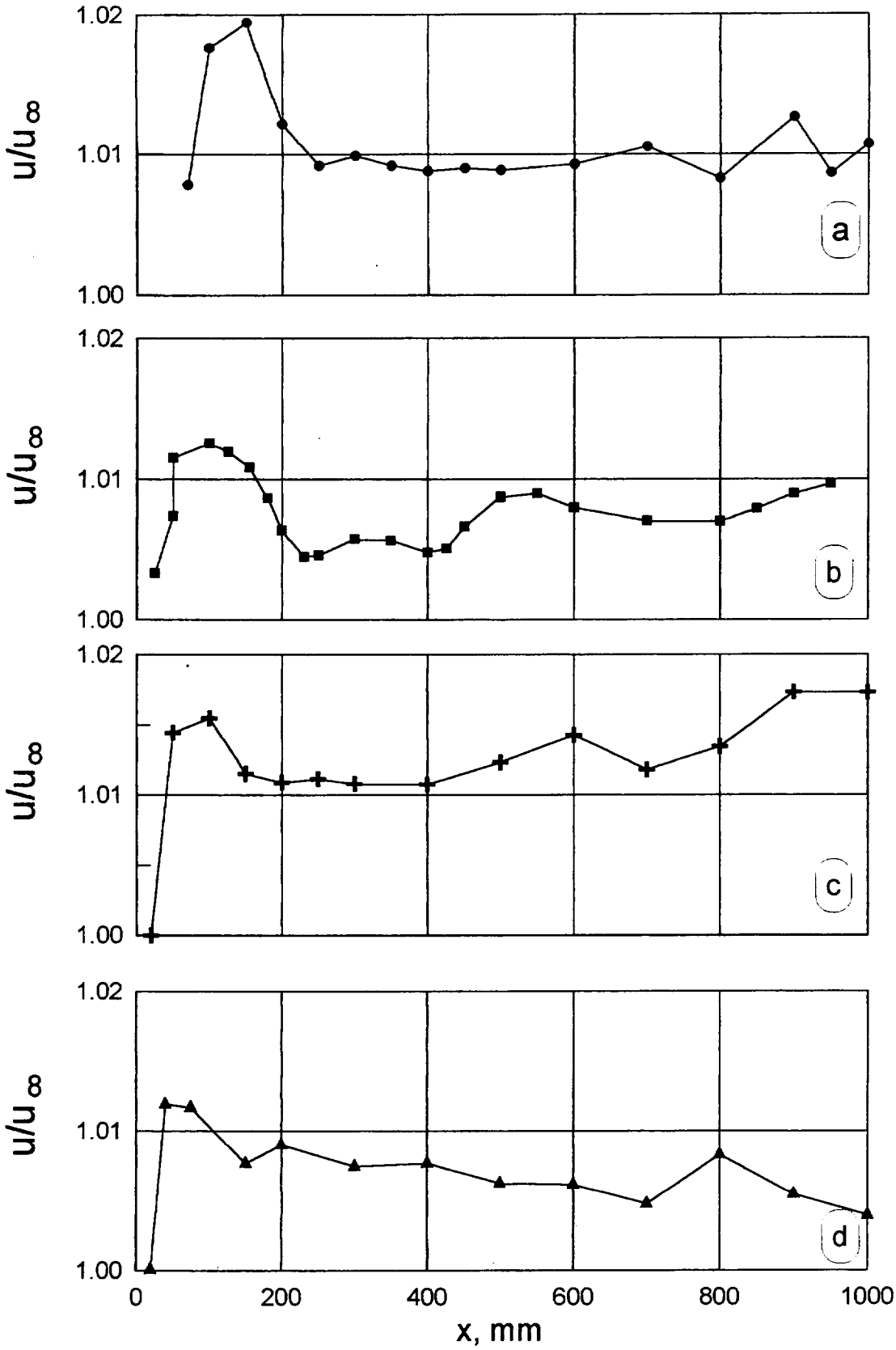

Figure 4 .Velocity distributions along the plane parts of plates.
a - plate № 1; b - plate № 2; c - plate № 3; d - plate № 4

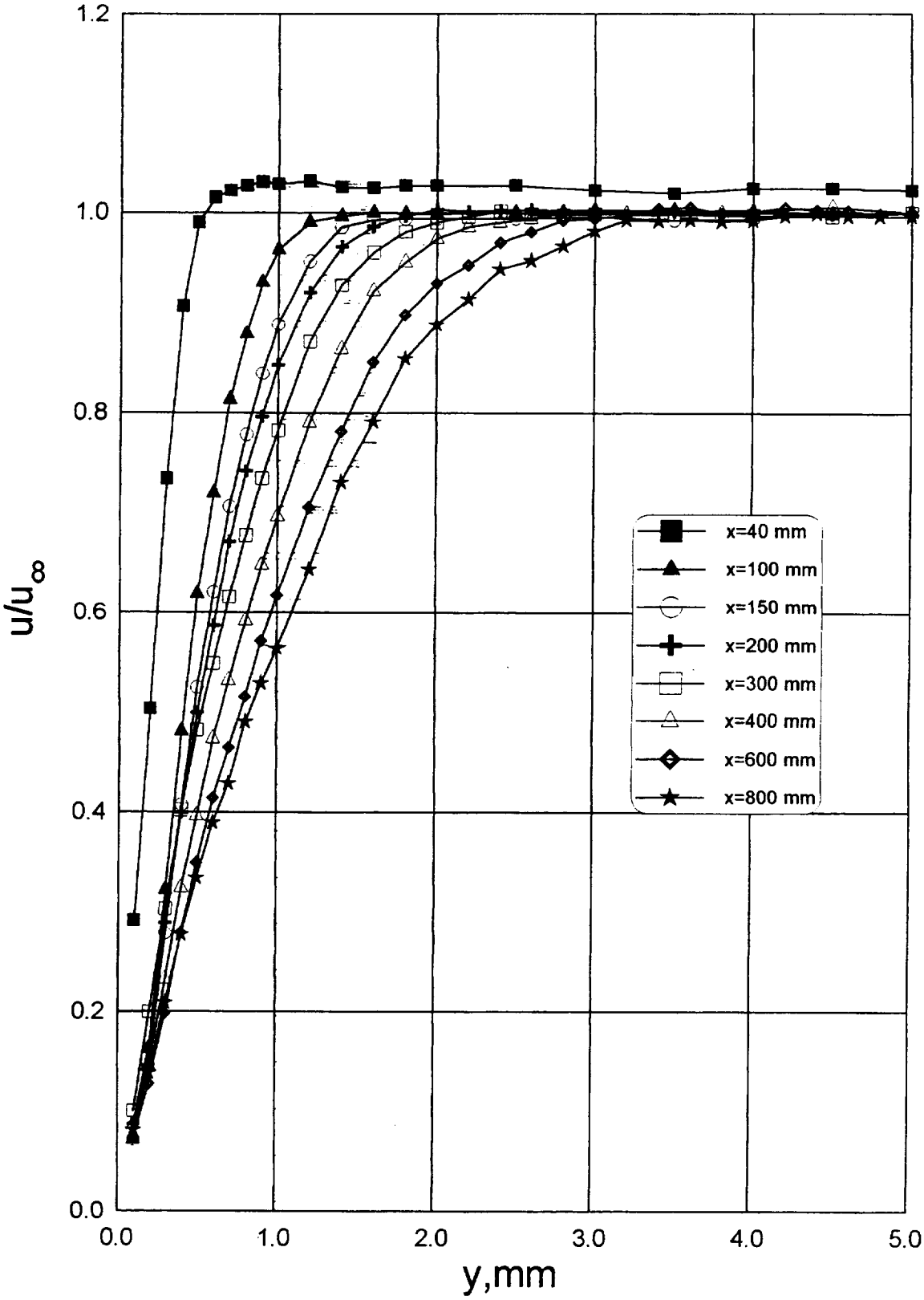

Figure 5 . Velocity profiles in boundary layer at plate №1

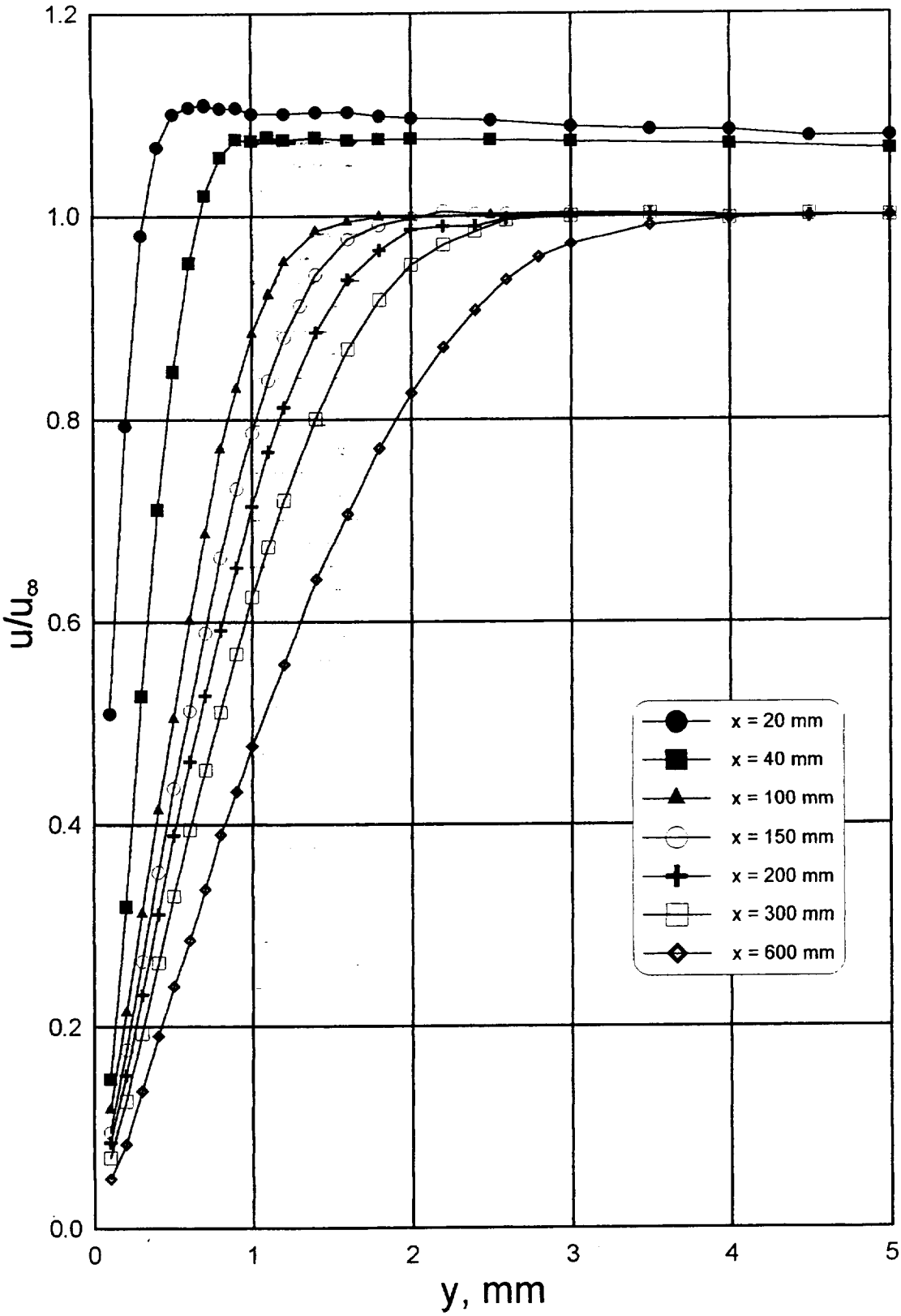

Figure 6. Velocity profiles in boundary layer at plate № 2.

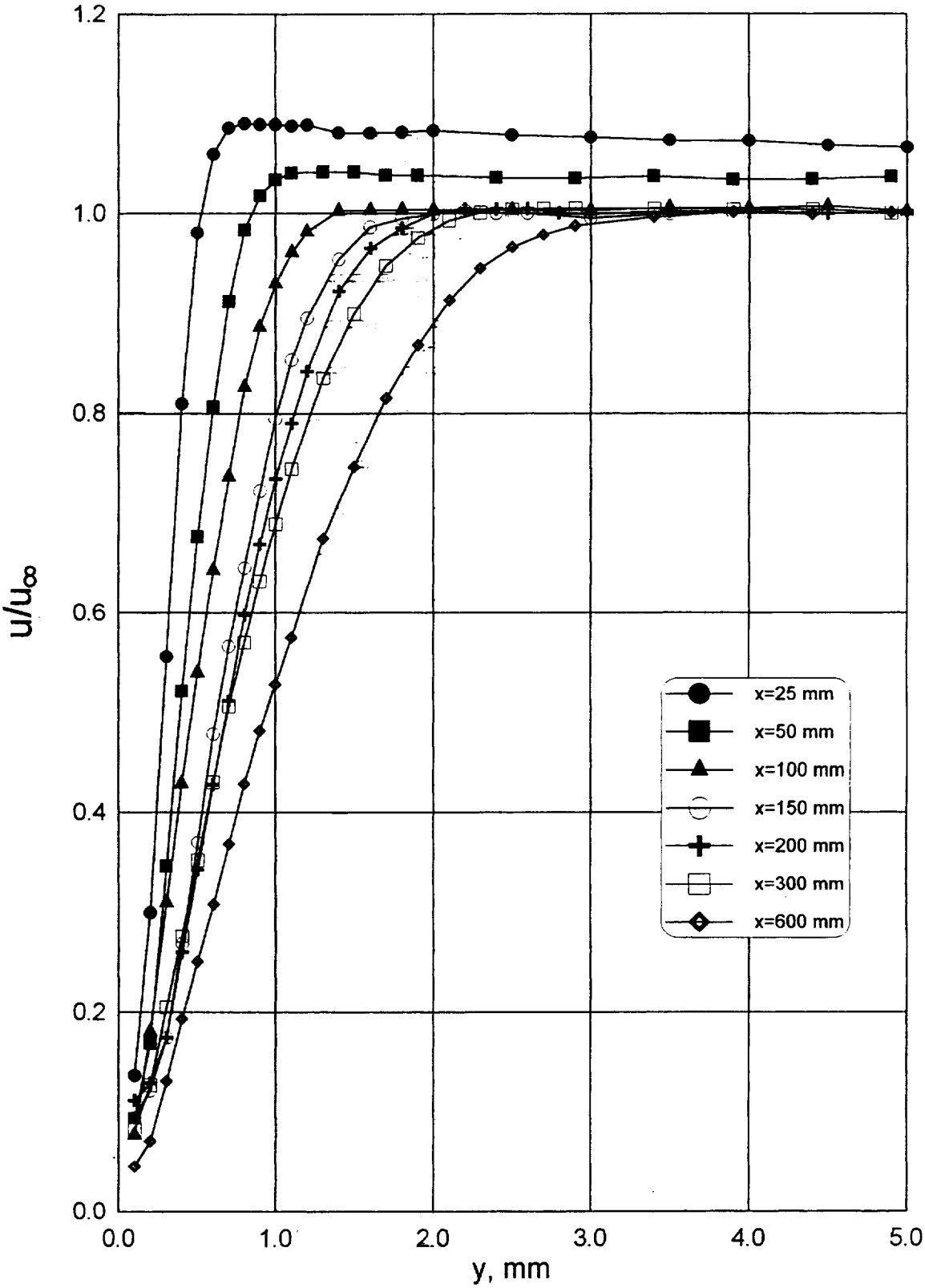

Figure 7 . Velocity profiles in boundary layer at plate № 3

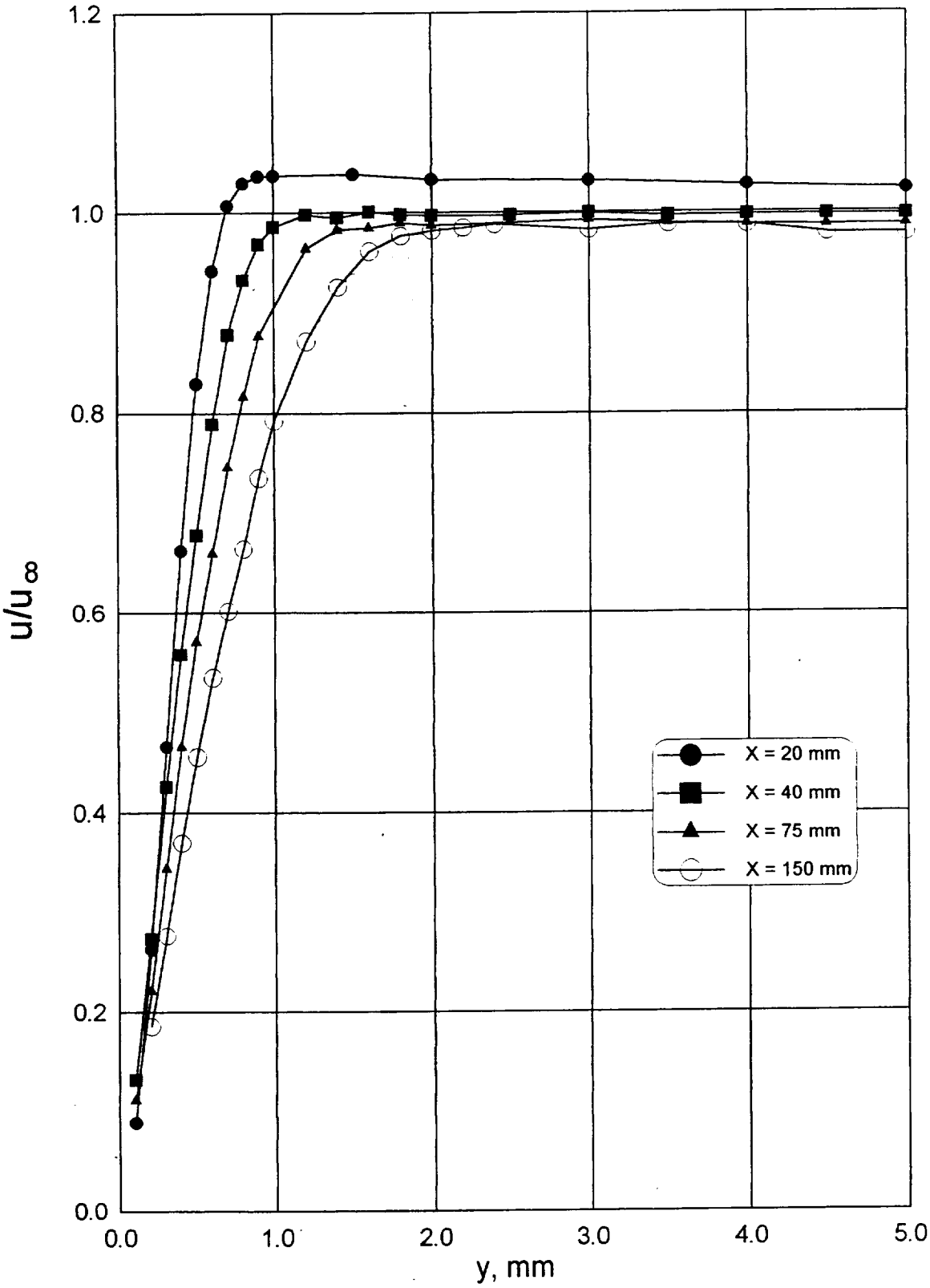

Figure 8 . Velocity profiles in boundary layer at plate № 4

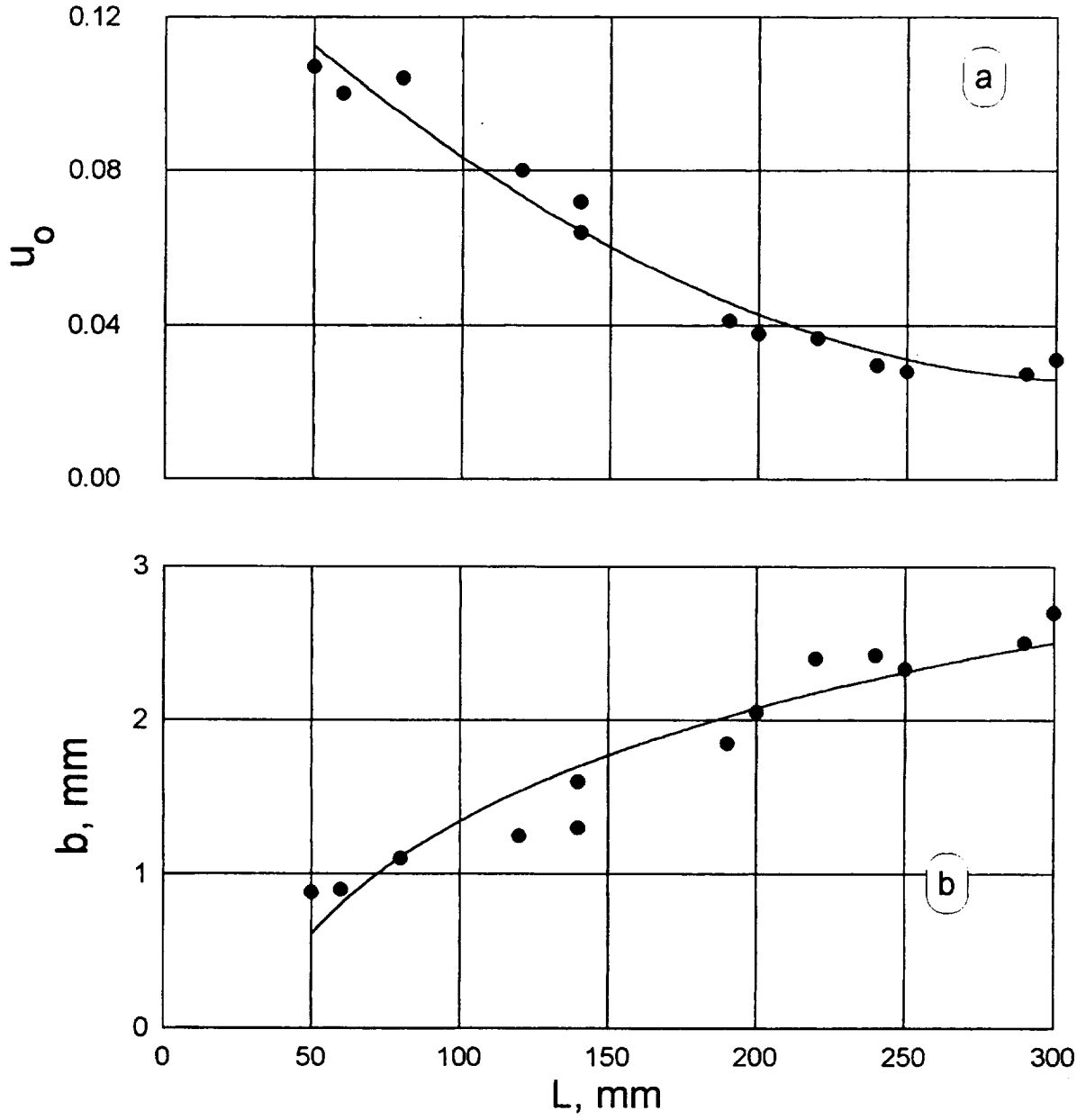

Figure 9 . Wake behind wire of d = 0.3 mm
in flow with u_∞ = 5 m/s
a) - velocity deficit u_o
b) - half width b

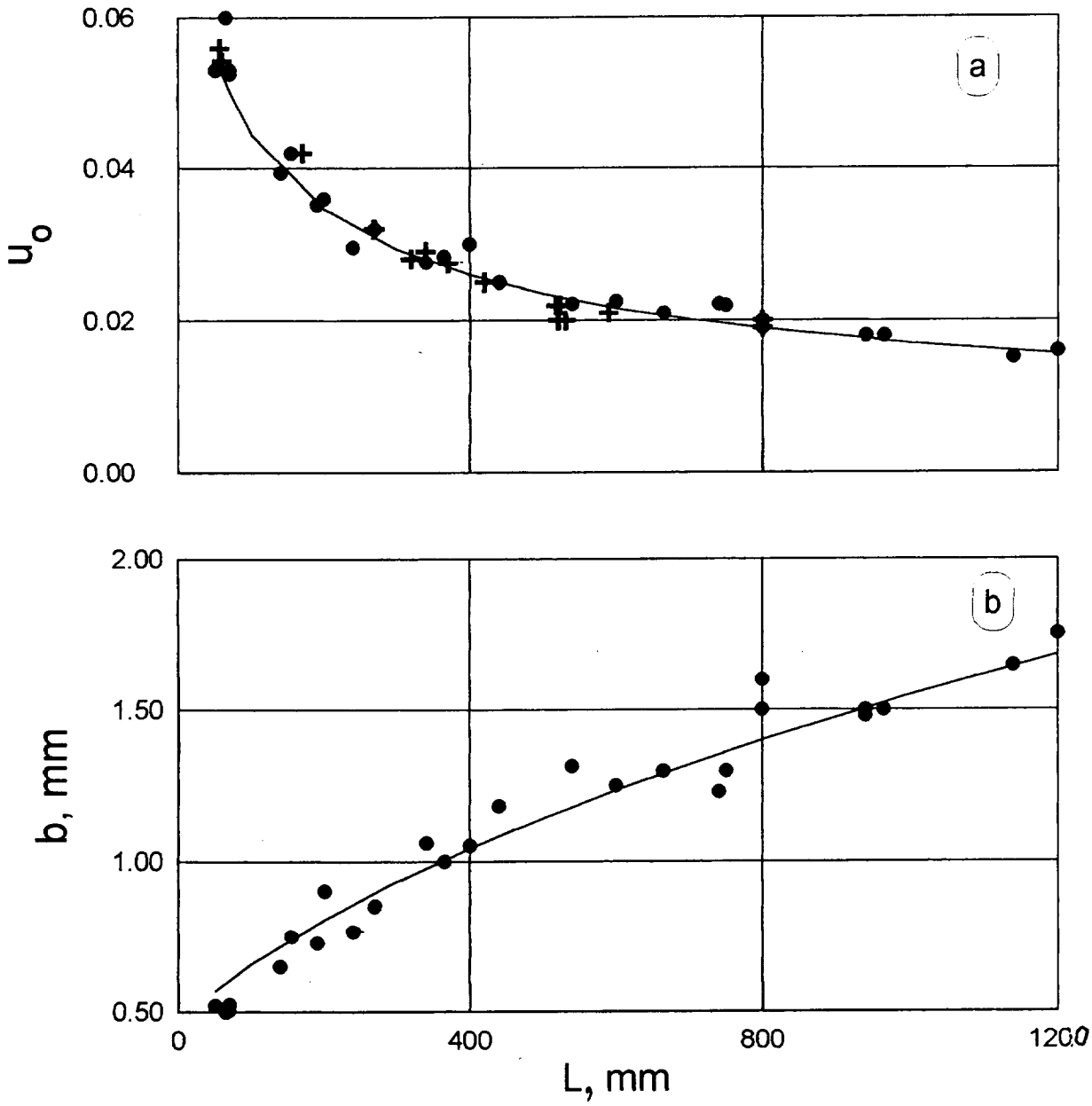

Figure 10 . Wake behind 1 and 5 wires of d = 0.09 mm
in flow with u_∞ = 17 m/s
(a) (●) - velocity deficit in the wake from single wire;
(+) - flow distortion $\Delta u/u_\infty$ in the wake from 5 wires
(b) - half-width of wake from single wire b

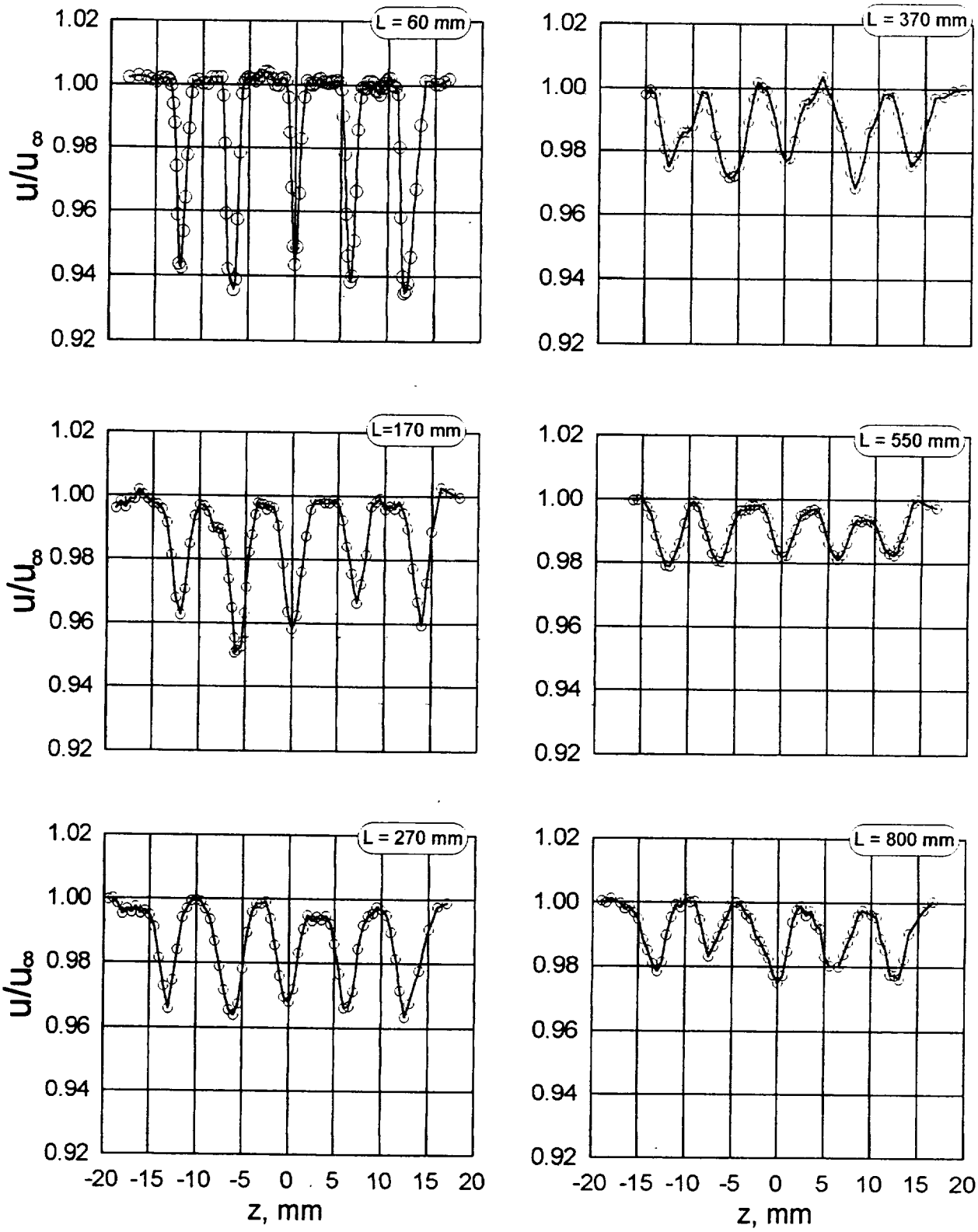

Figure 11. Mean velocity profiles in wake behind 5 wires of d = 0.09 mm in flow with u_∞ = 17 m/s

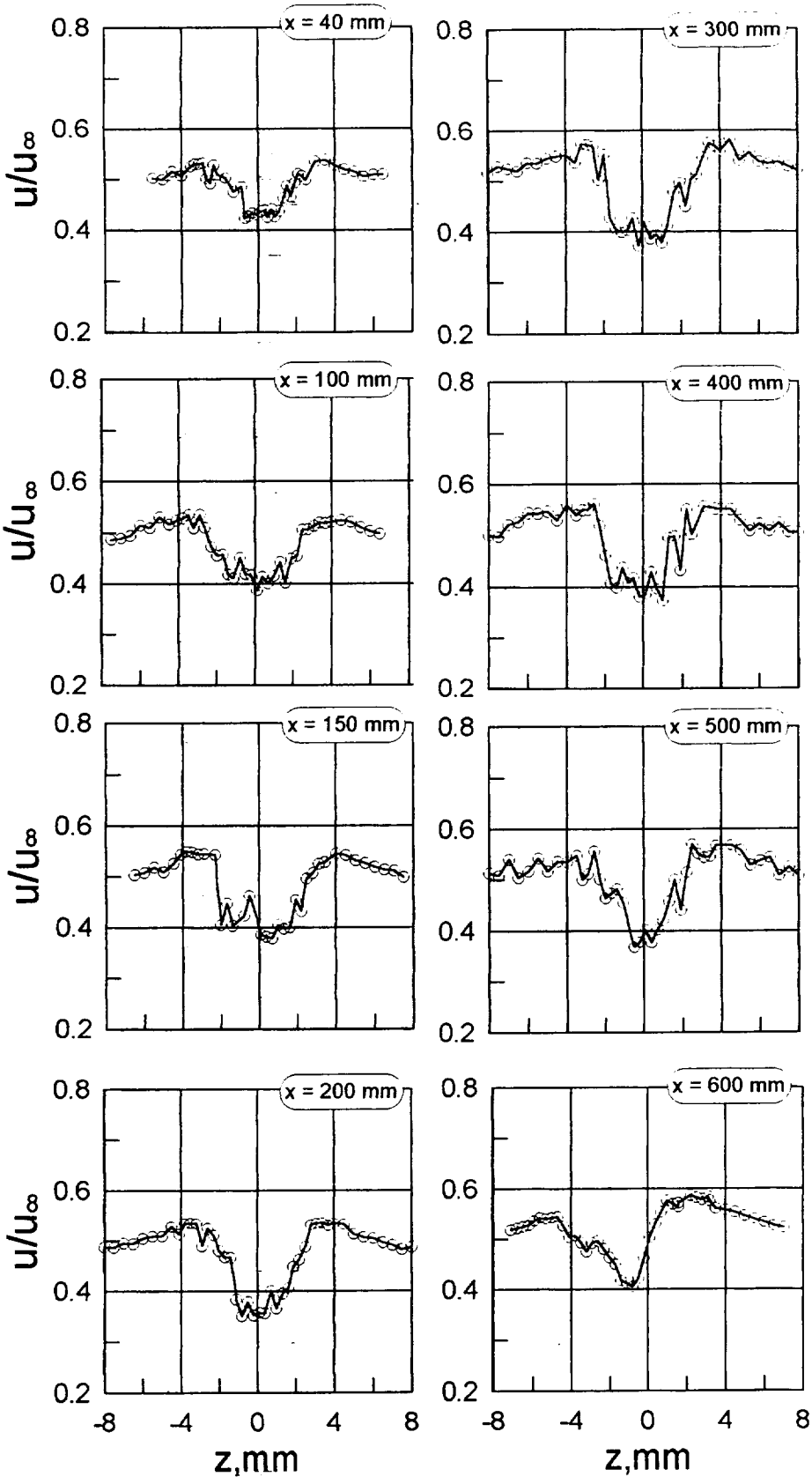

Figure 12 . Boundary layer distortion in linear regime of interaction.
(configuration 8; u_∞=17 m/s; plate № 2; d=0.09 mm;
L = 725 mm)

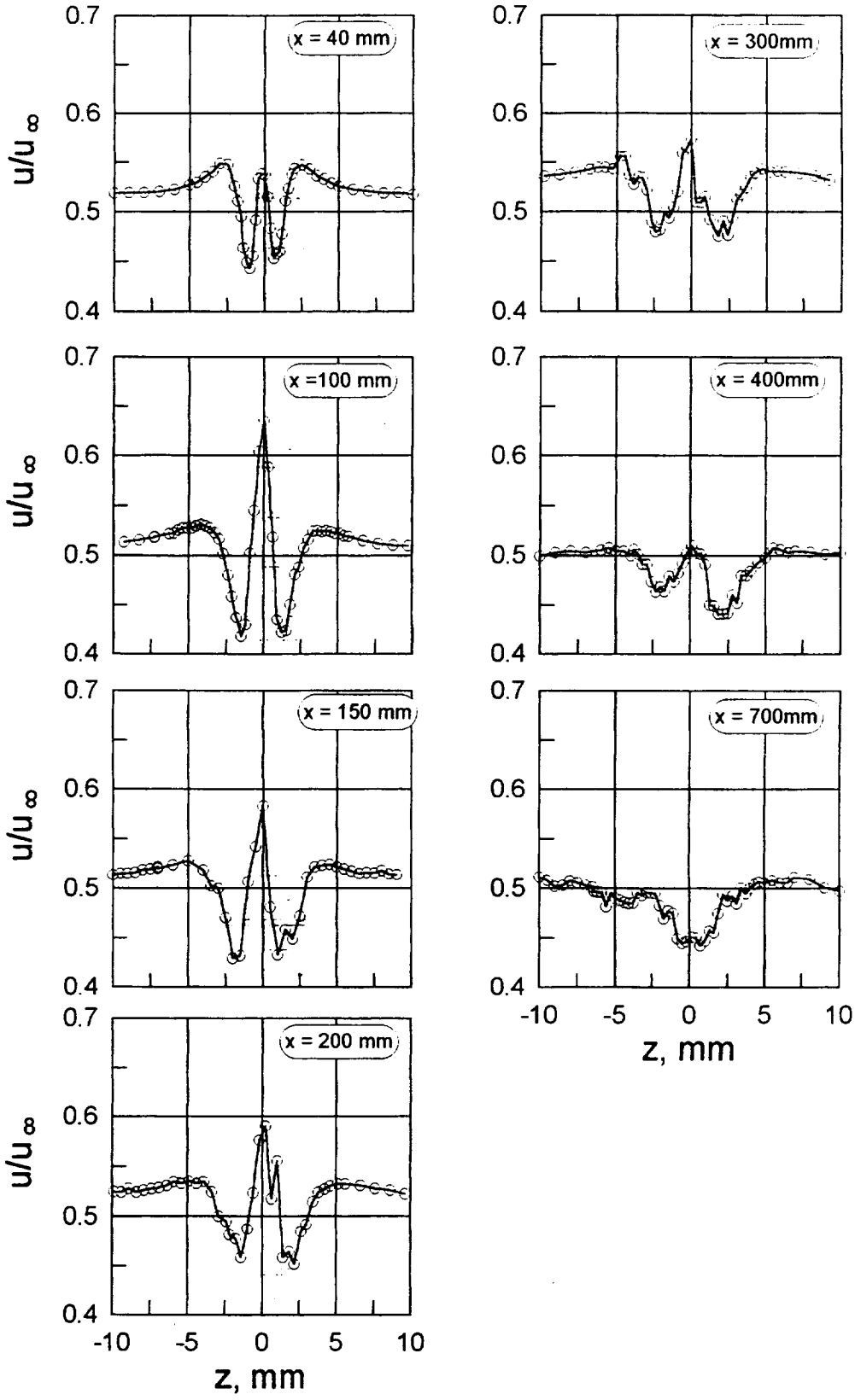

Figure 13. Boundary layer distortion in nonlinear symmetric regime of interaction
(configuration 6; u_∞ = 17 m/s; plate №2; d = 0.09 mm; L = 250 mm)

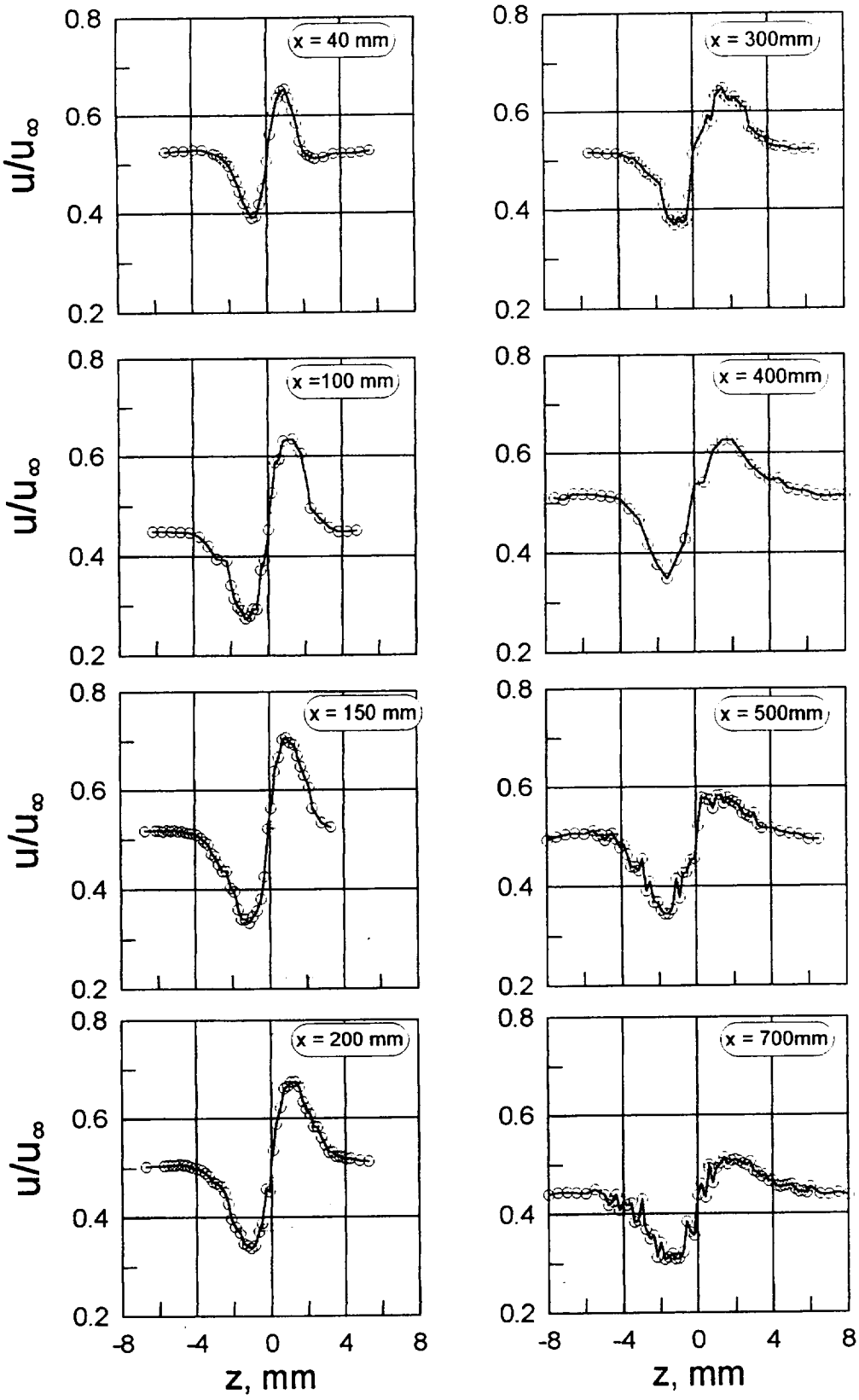

Figure 14. Boundary layer distortion in nonlinear antisymmetric regime of interaction
(configuration 4; u_∞=17 m/s; plate №2; d=0.09 mm; L = 40 mm)

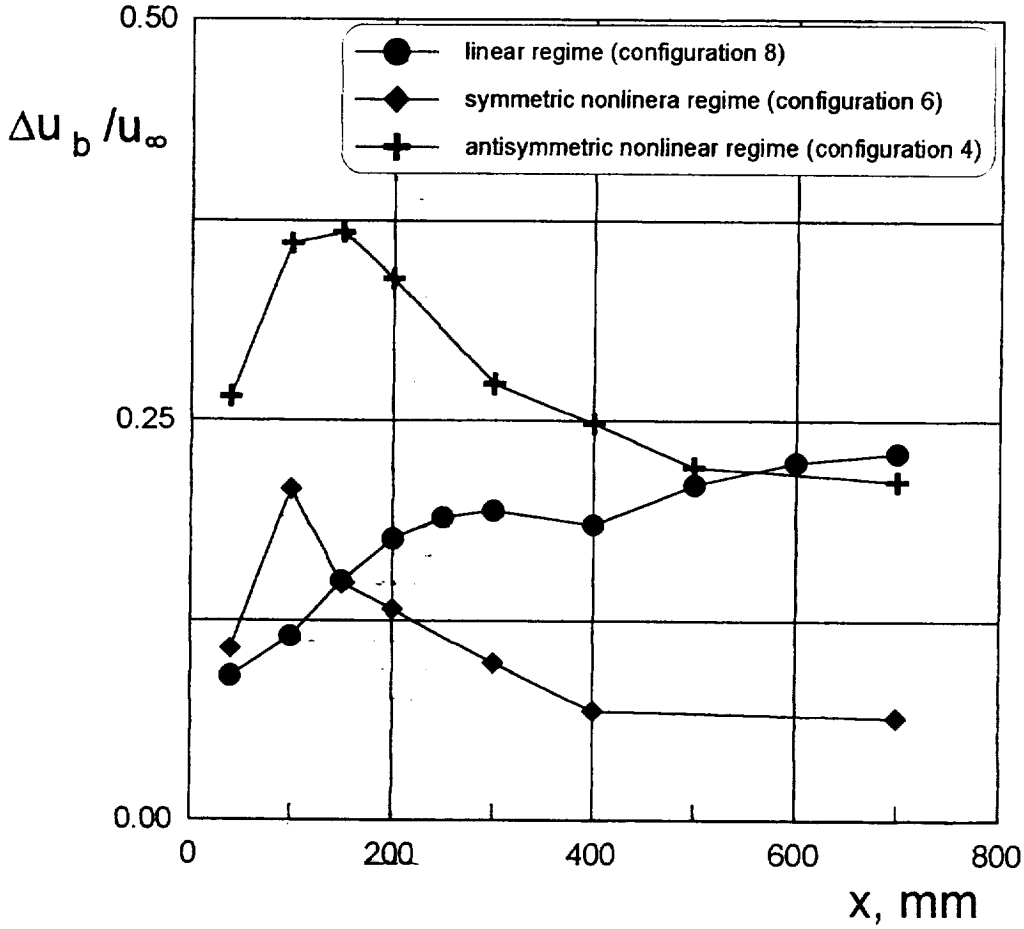

Figure 15. Boundary layer distortion as function of distance from leading edge for linear (—●—); nonlinear symmetric (—◆—); and nonlinear antisymmetric (—+—) regimes of interaction.

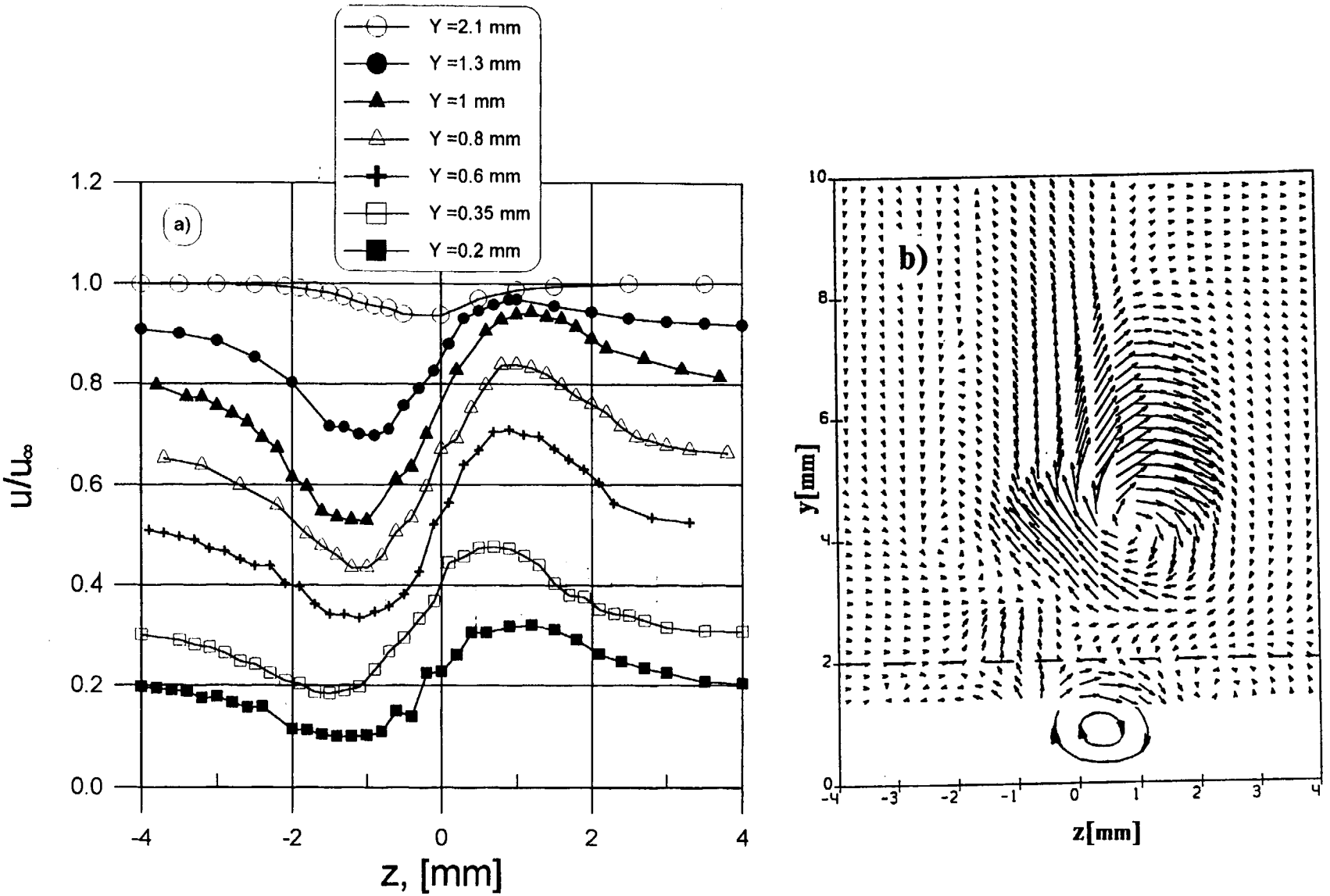

Figure16. Distribution of three components of velocity vector in (y,z) - plane at x = 150 mm measured in configuration 4 (nonlinear antisymmetric regime)
(a) - spanwise profiles of streamwise velocity
(b) - projections of velocity vectors onto (y, z) - plane

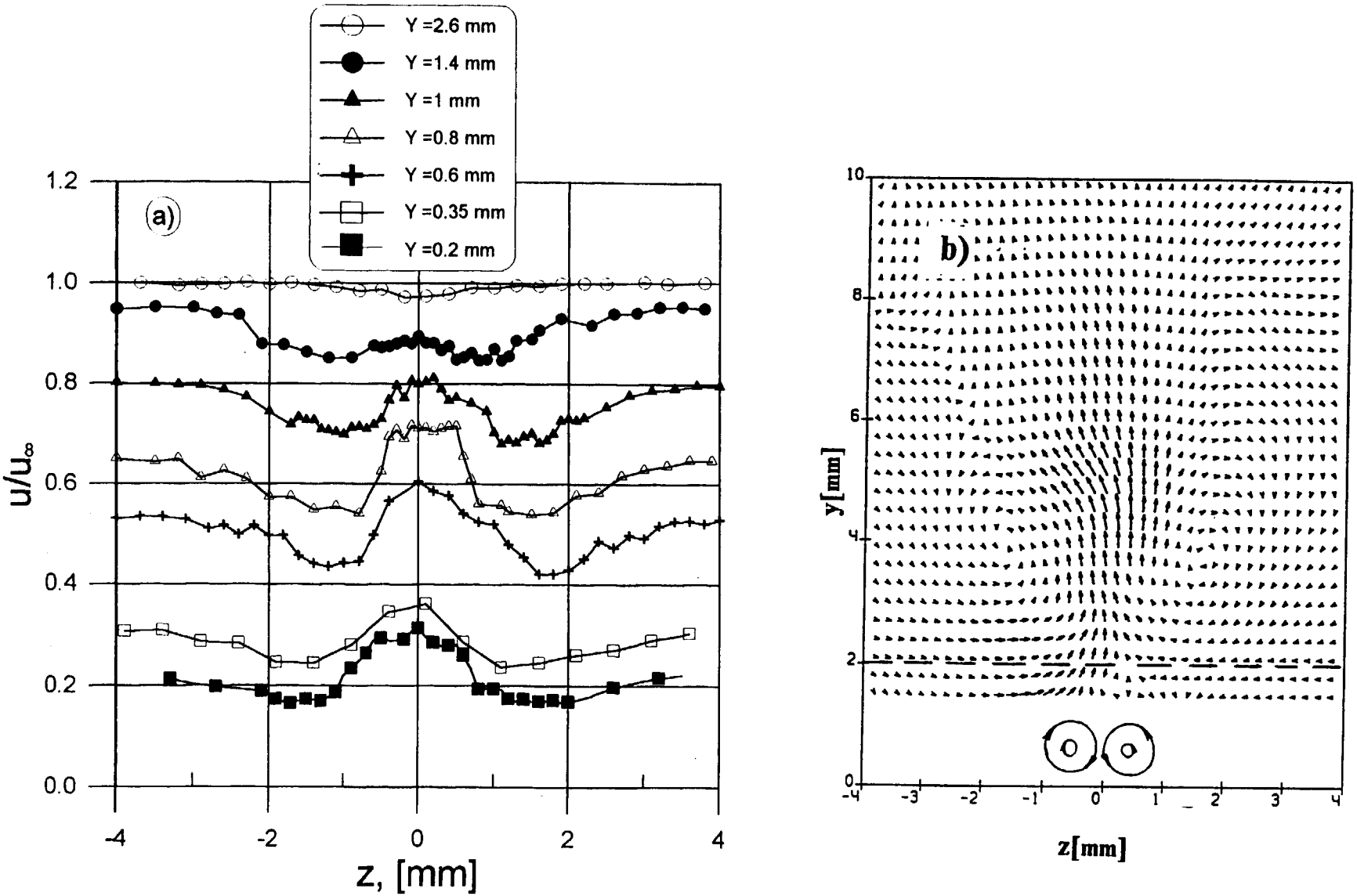

Figure17. Distribution of three components of velocity vector in (y,z) - plane at x = 150 mm measured in configuration 6 (nonlinear antisymmetric regime)
(a) - spanwise profiles of streamwise velocity
(b) - projections of velocity vectors onto (y, z) - plane

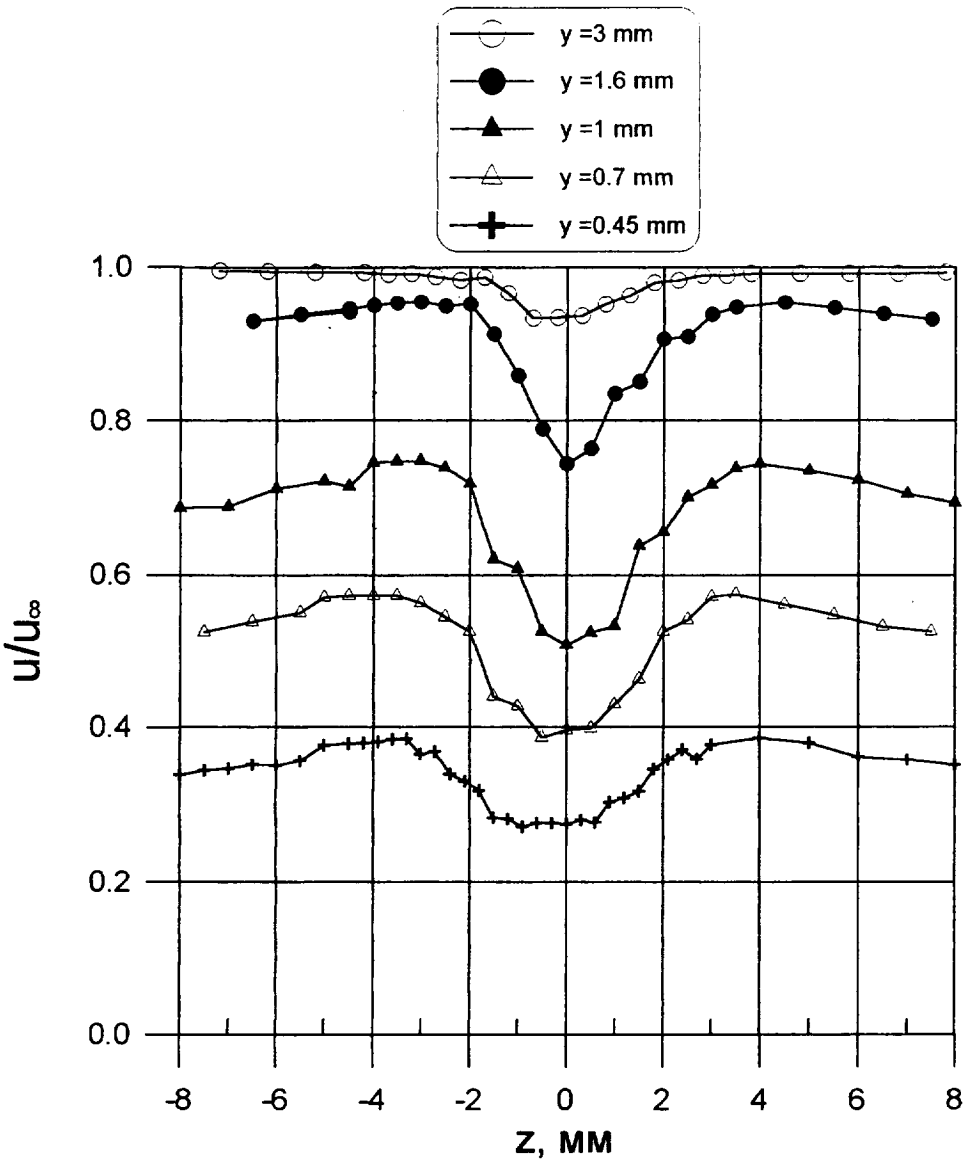

Figure 18.Streamwise velocity distribution in (y,z) - plane at x=250 mm measured in configuration 8 (linear regime)

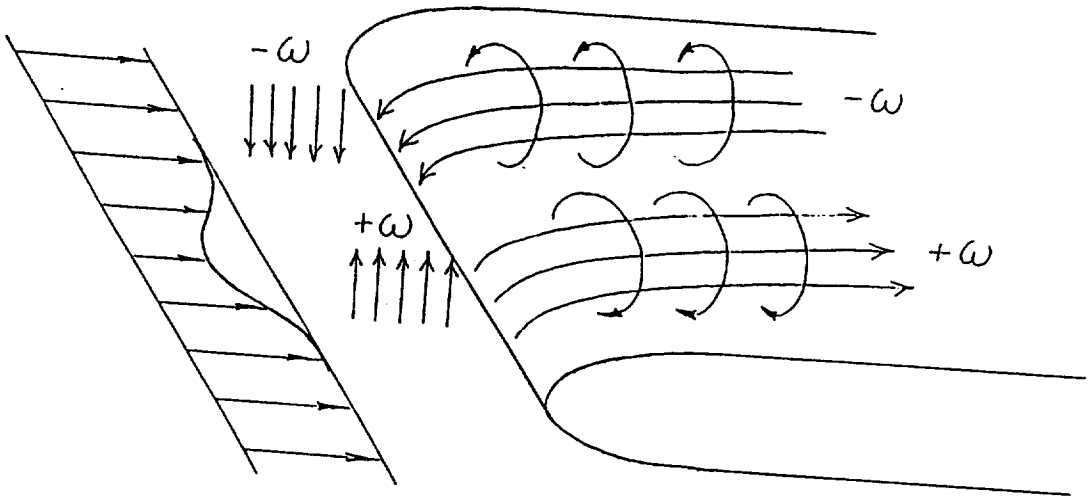

Figure 19. Conceptual scheme of vortex lines stretching by flow around the leading edge.

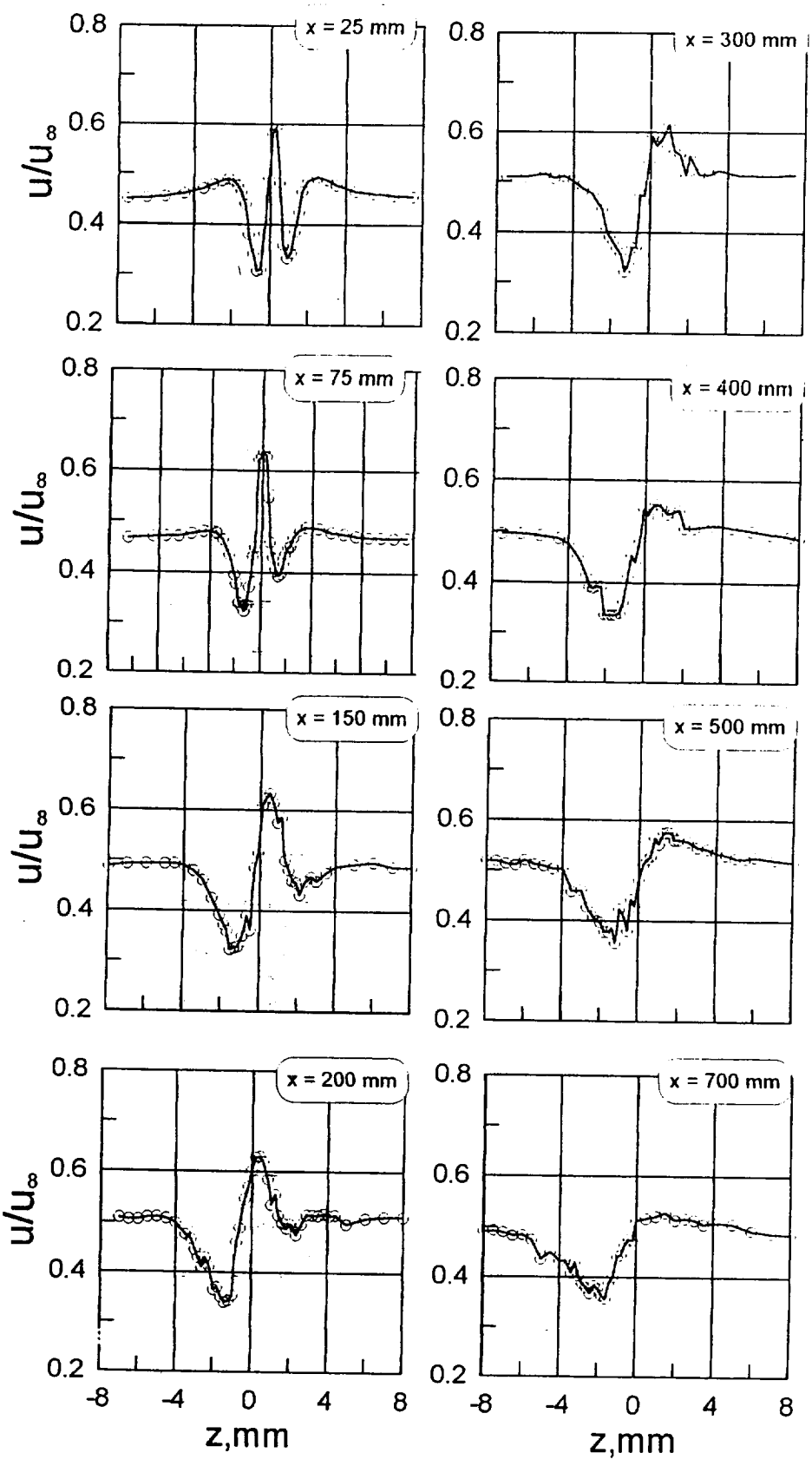

Figure 20 a). Boundary layer distortion in configuration 10 where initially symmetric velocity profile gradually becomes antisymmetric.

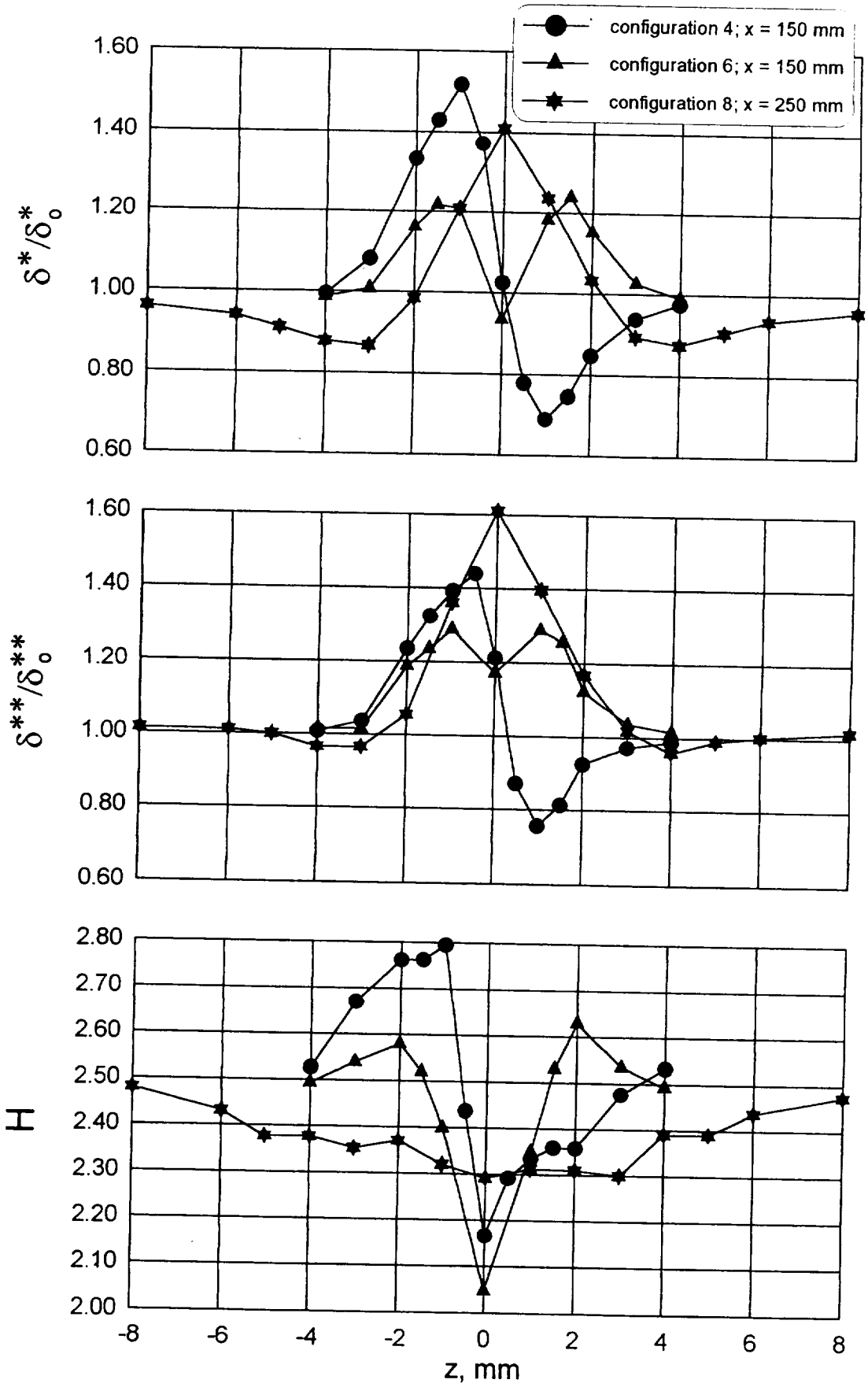

Figure 20b). Integral characteristics of boundary layer distorted by wake as function of z for different regimes of interaction.

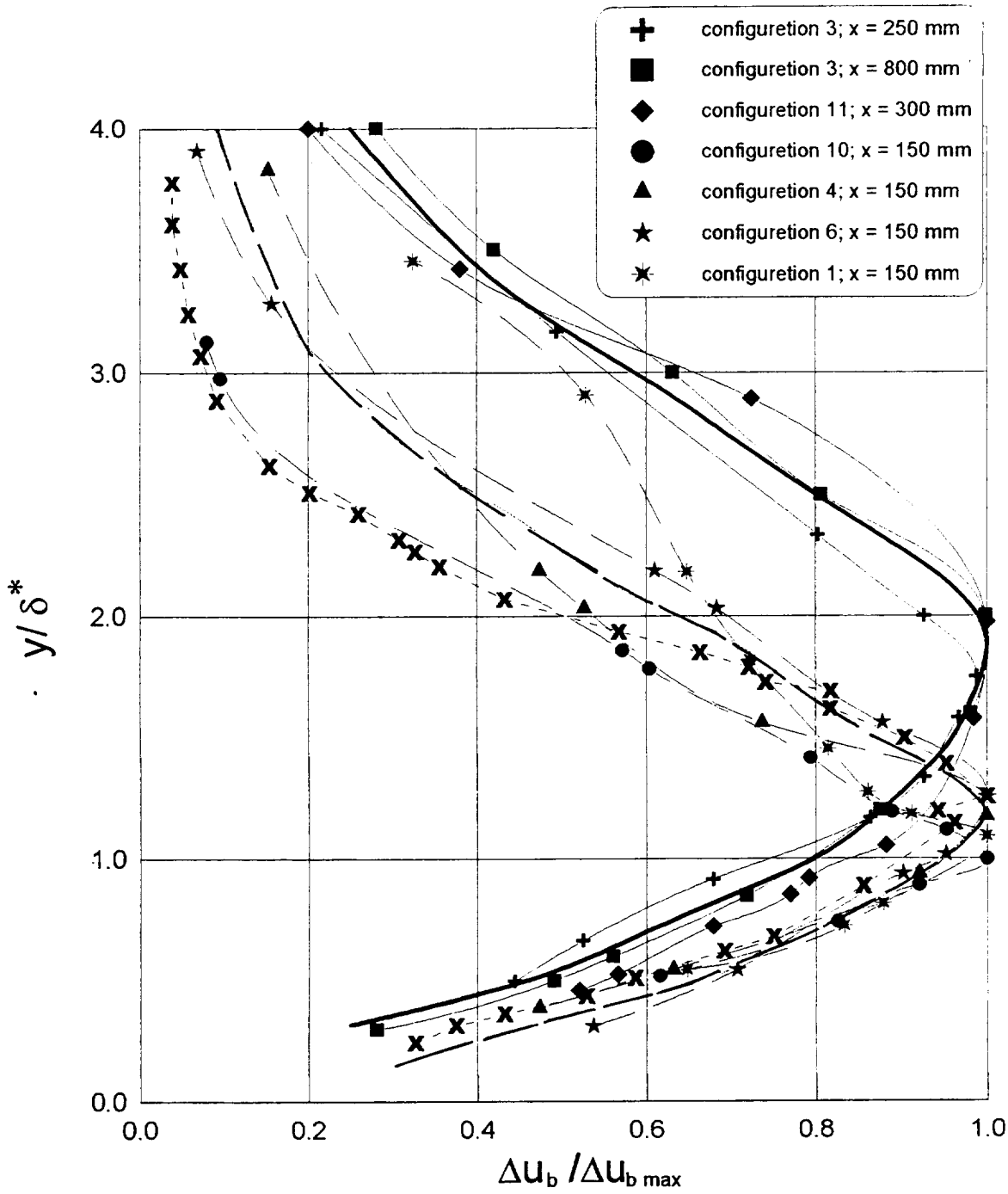

Figure 21. Vertical profiles of flow distortion in boundary layer measured in different configurations (+■◆●▲★✳); common curve for linear regimes (——); common curve for nonlinear regimes (- - -); low-frequency pulsations in boundary layer subjected to free-stream turbulence [9] (×).

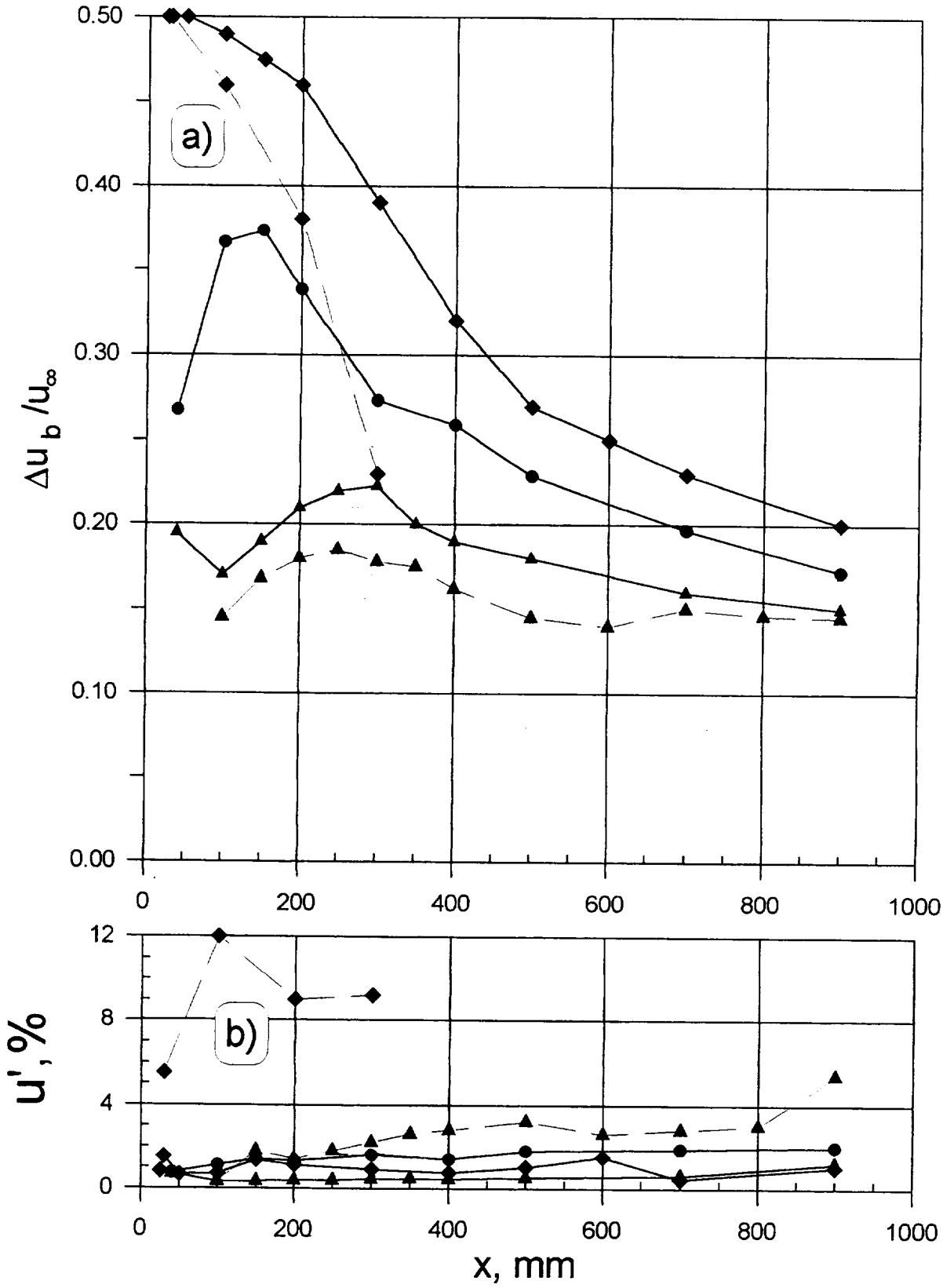

Figure 22. Flow distortion Δu_b (a) and r.m.s. velocity pulsation (b) as functions of x for near wakes (L = 40 mm) interaction with plates № 1 - 3.

▲ - plate №1; ● - plate №2; ◆ - plate №3;
(——) - single wire wake; (- - -) - wake from 5 wires.

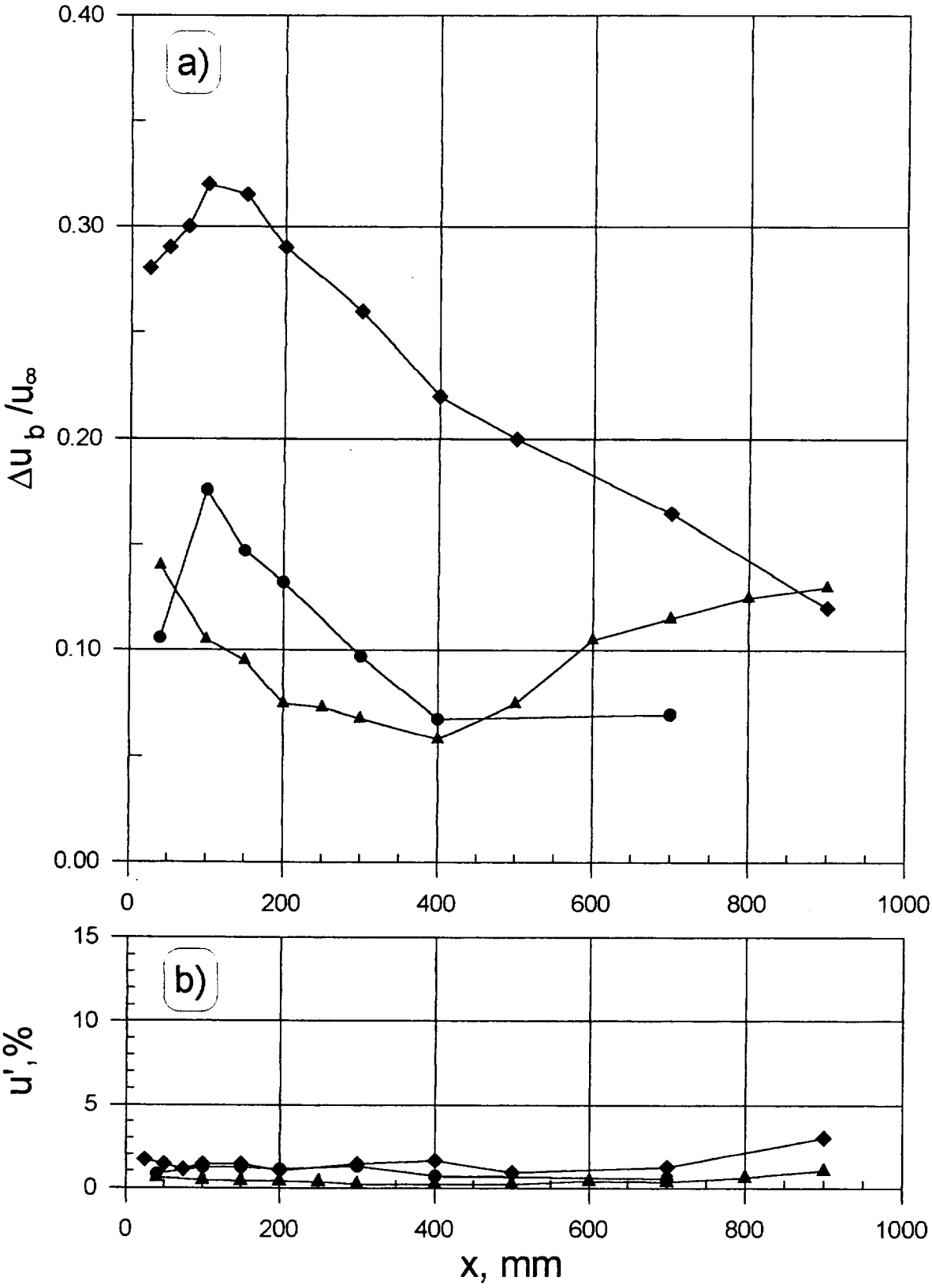

Figure 23. Flow distortion Δu_b (a) and r.m.s. velocity pulsations (b) as functions of x for medium wakes (L = 250 mm) interaction with plates № 1 - 3. Designations are similar to Figure 22.

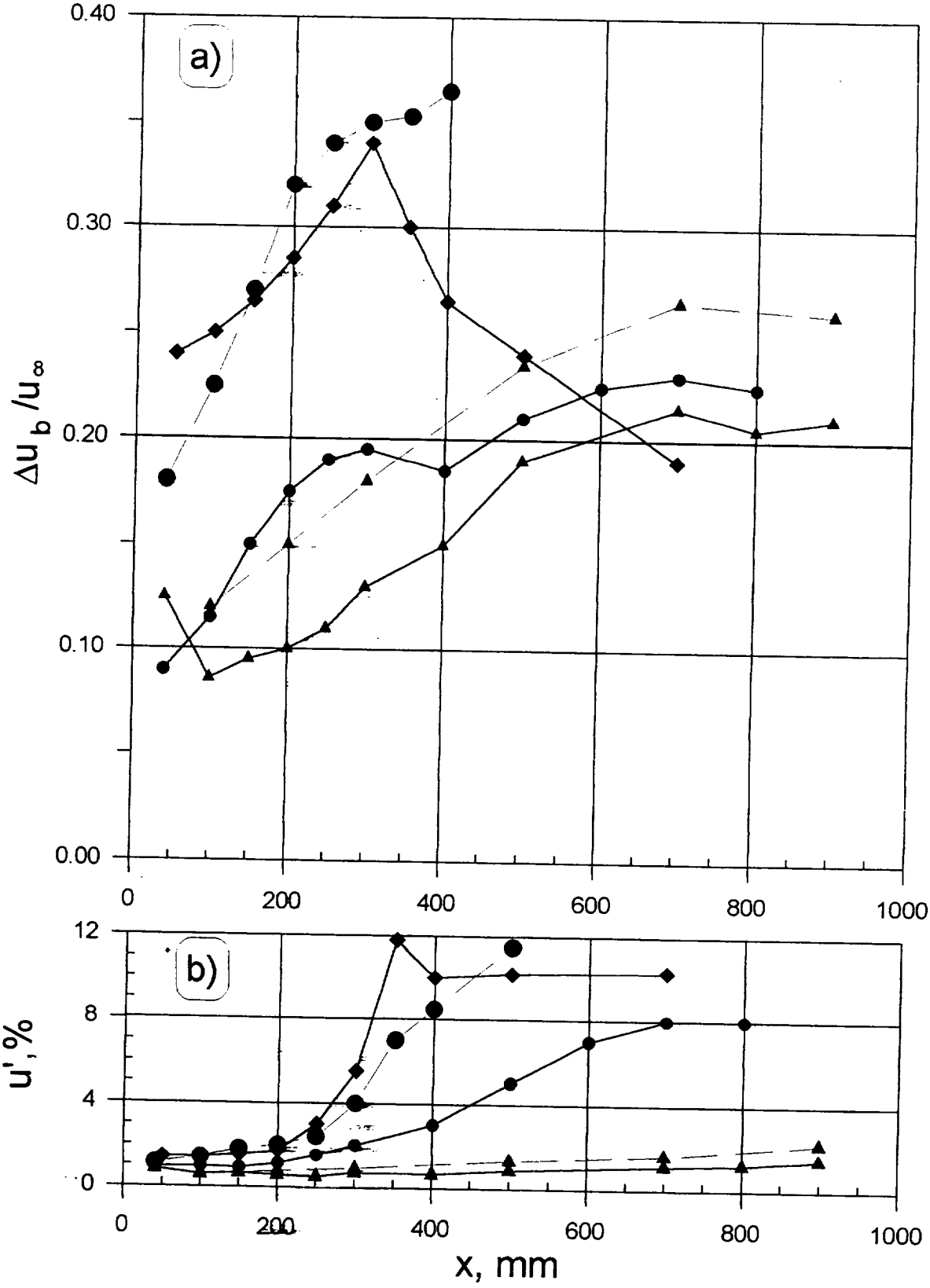

Figure 24. Flow distortion Δu_b (a) and r.m.s. velocity pulsations (b) as functions of x for far wakes (L = 725 mm) interaction with plates № 1 - 3. Designations are similar to Figure 22.

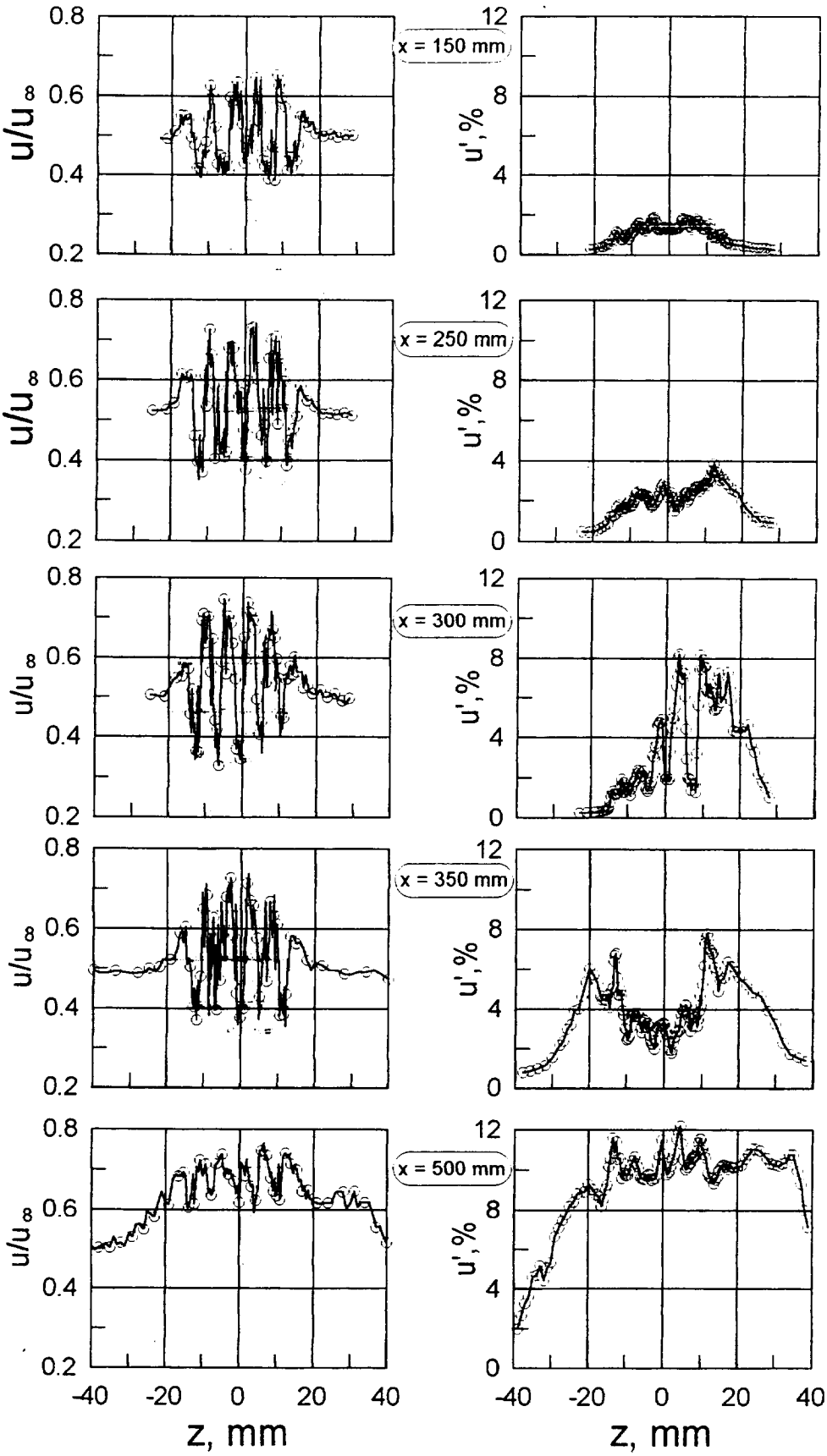

Figure 25 Spanwise profiles of mean velocity u and r.m.s. pulsations u' in boundary layer in configuration 22. (u_∞ = 17 m/s; 5 wires; plate № 2; L = 725 mm)

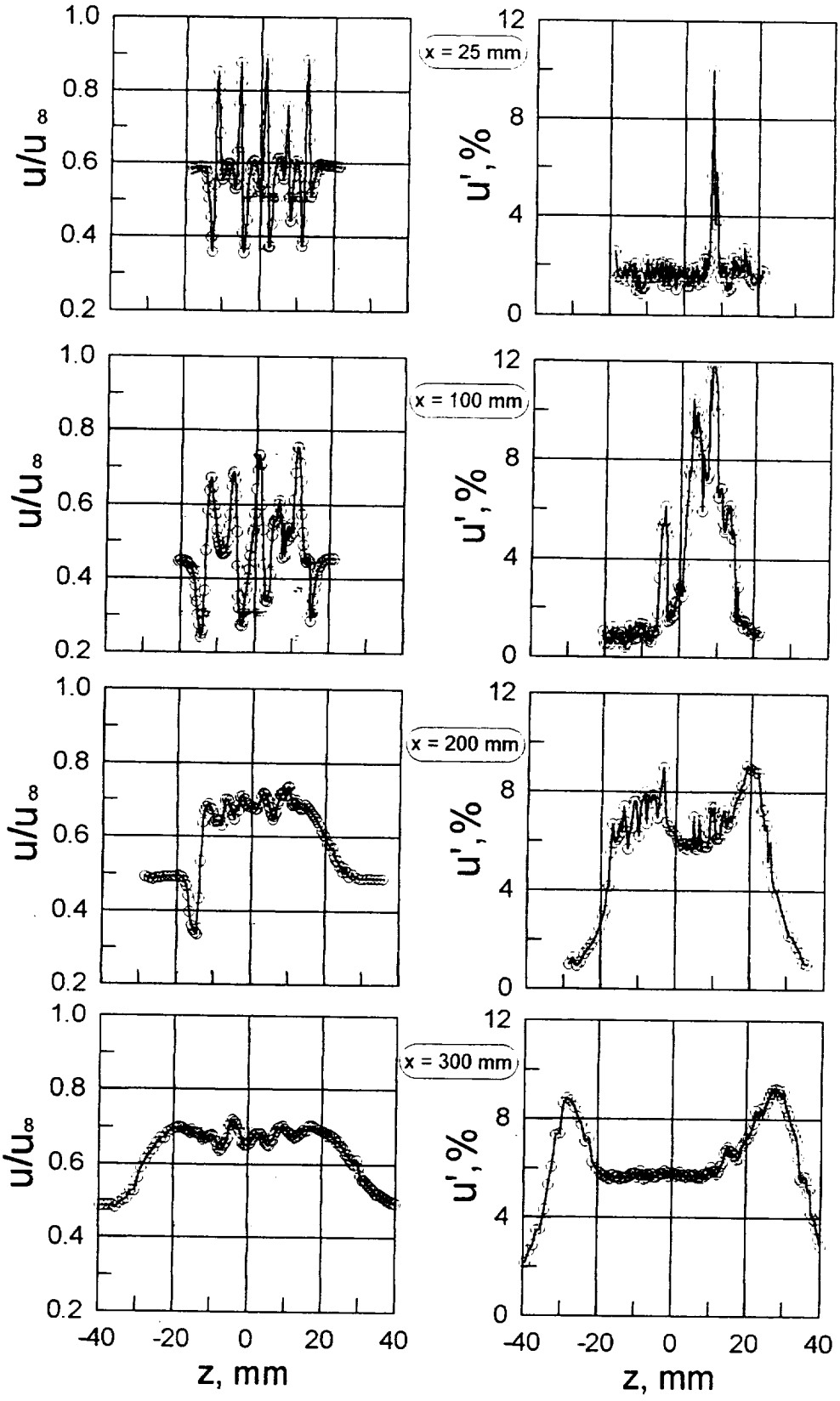

Figure 26 . Spanwise profiles of mean velocity u and r.m.s. pulsations u' in boundary layer in configuration 20. (u_∞=17 m/s; 5 wires; plate № 3; L= 40 mm)

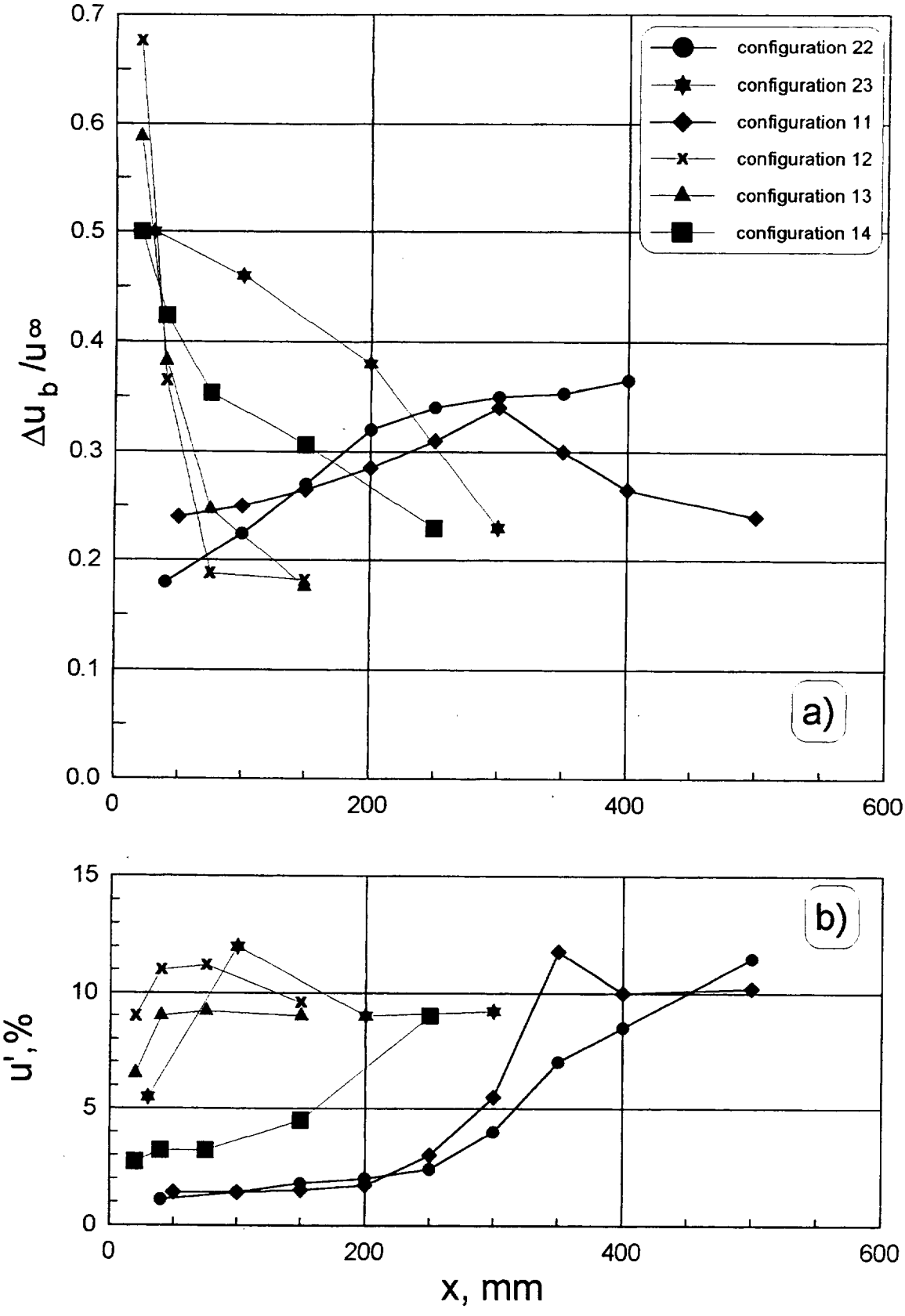

Figure 27. Boundary layer distortion (a) and r.m.s. pulsations (b) as functions of x in configurations where laminar-turbulent transition occurred.

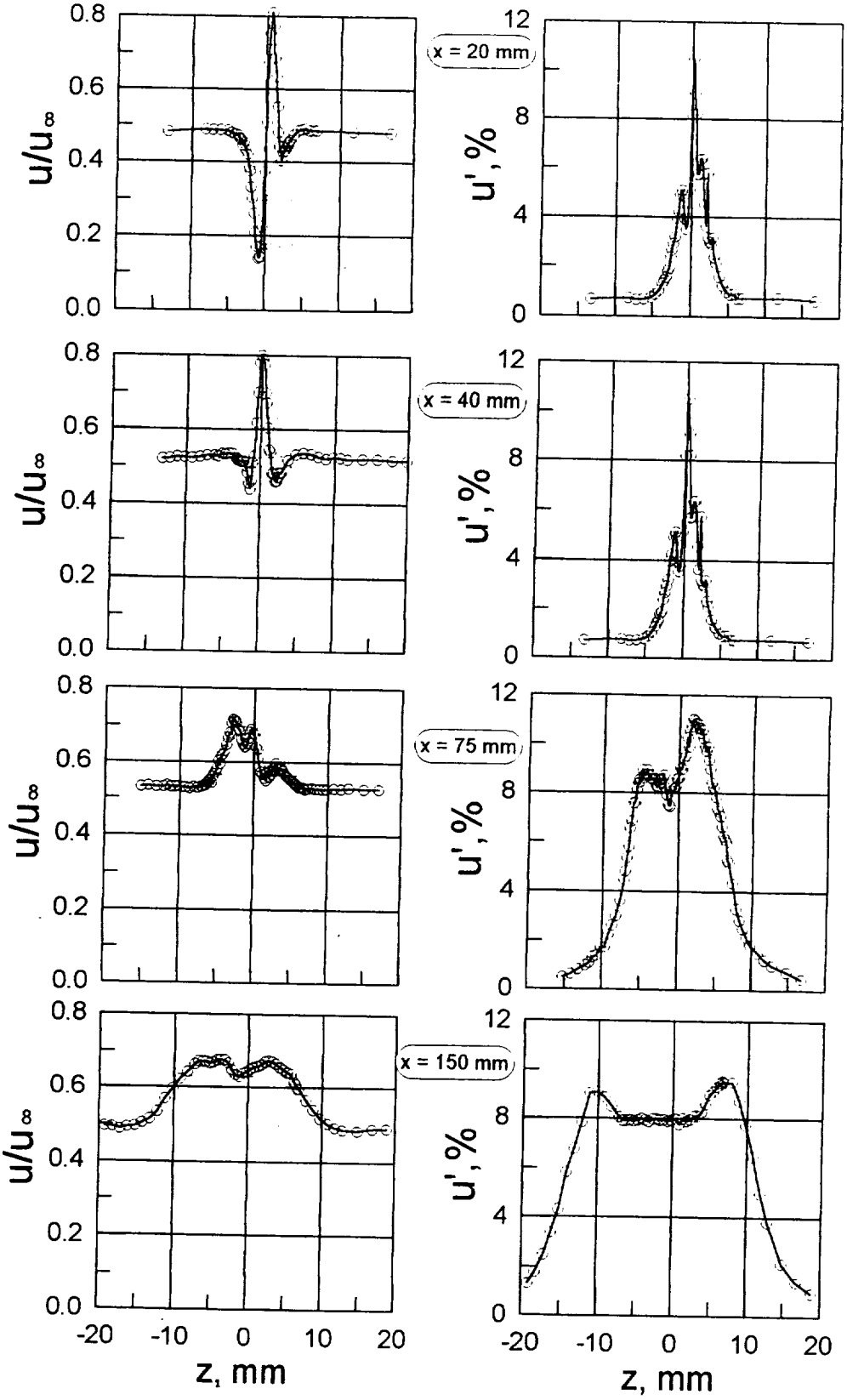

Figure 28 . Spanwise profiles of mean velocity u and r.m.s. pulsations u' in boundary layer in configuration 12. (u_∞=17 m/s; plate № 4; d = 0.09 mm; L= 40 mm)

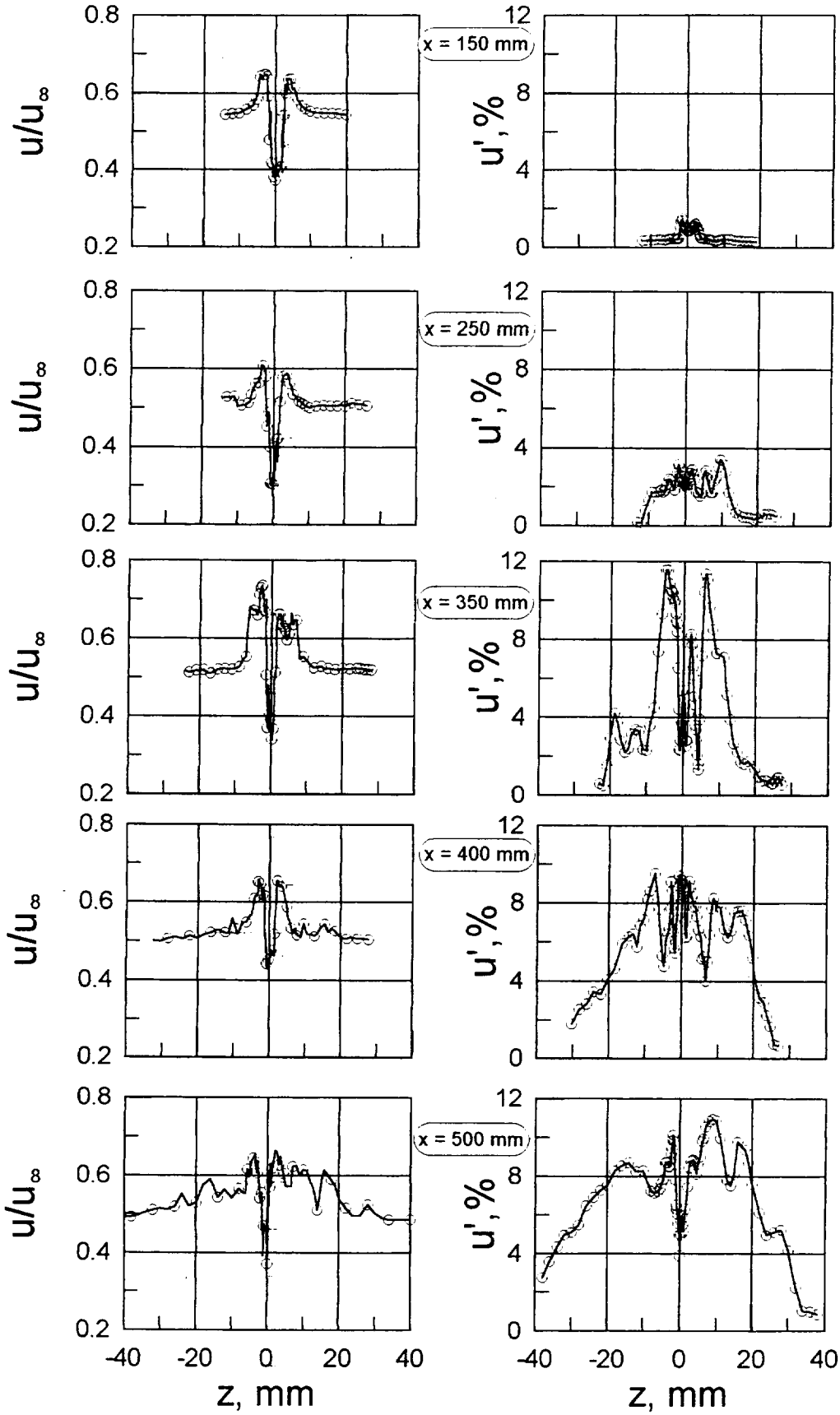

Figure 29 . Spanwise profiles of mean velocity u and r.m.s. pulsations u' in boundary layer in configuration 11. (u_∞=17 m/s; plate № 3; d = 0.09 mm; L= 725 mm)

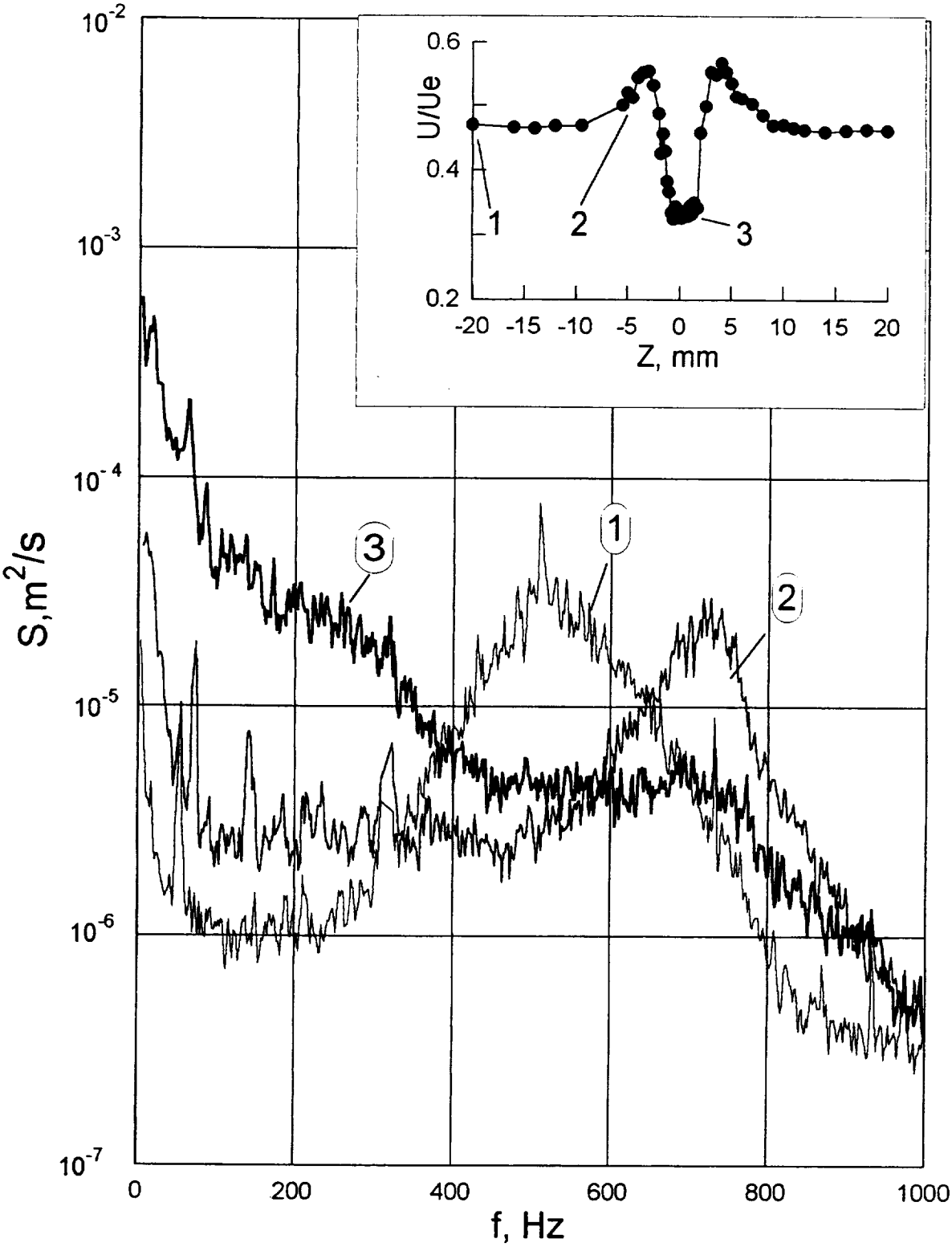

Figure 30. Power spectrum of streamwise velocity pulsations S(f) measured in configuration 11 at x = 150 mm

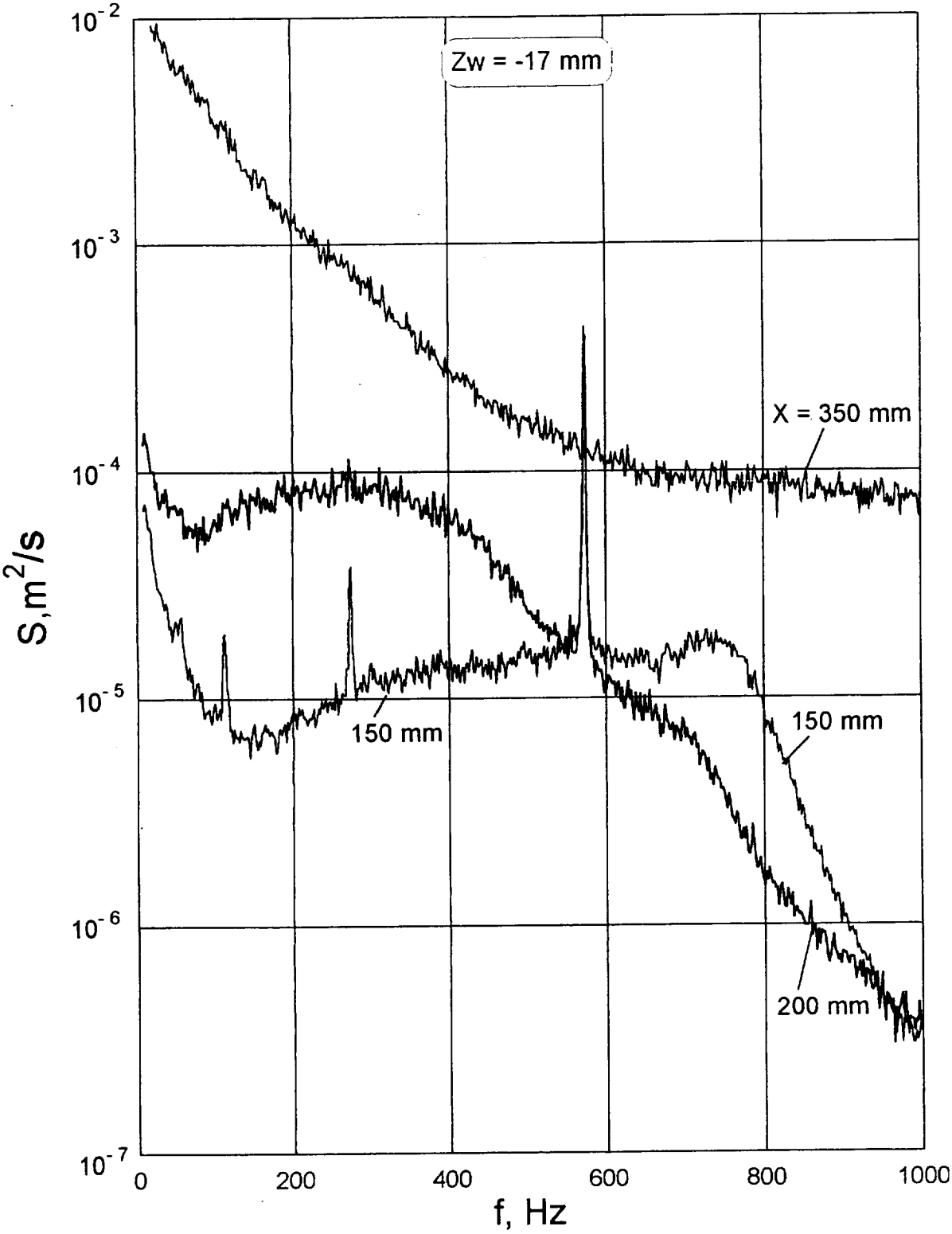

Figure 31. Evolution of power spectrum streamwise velocity pulsations S(f) measured at the side of disturbed area (z = -17 mm) in boundary layer distorted by wake from 5 wires in configuration 22.

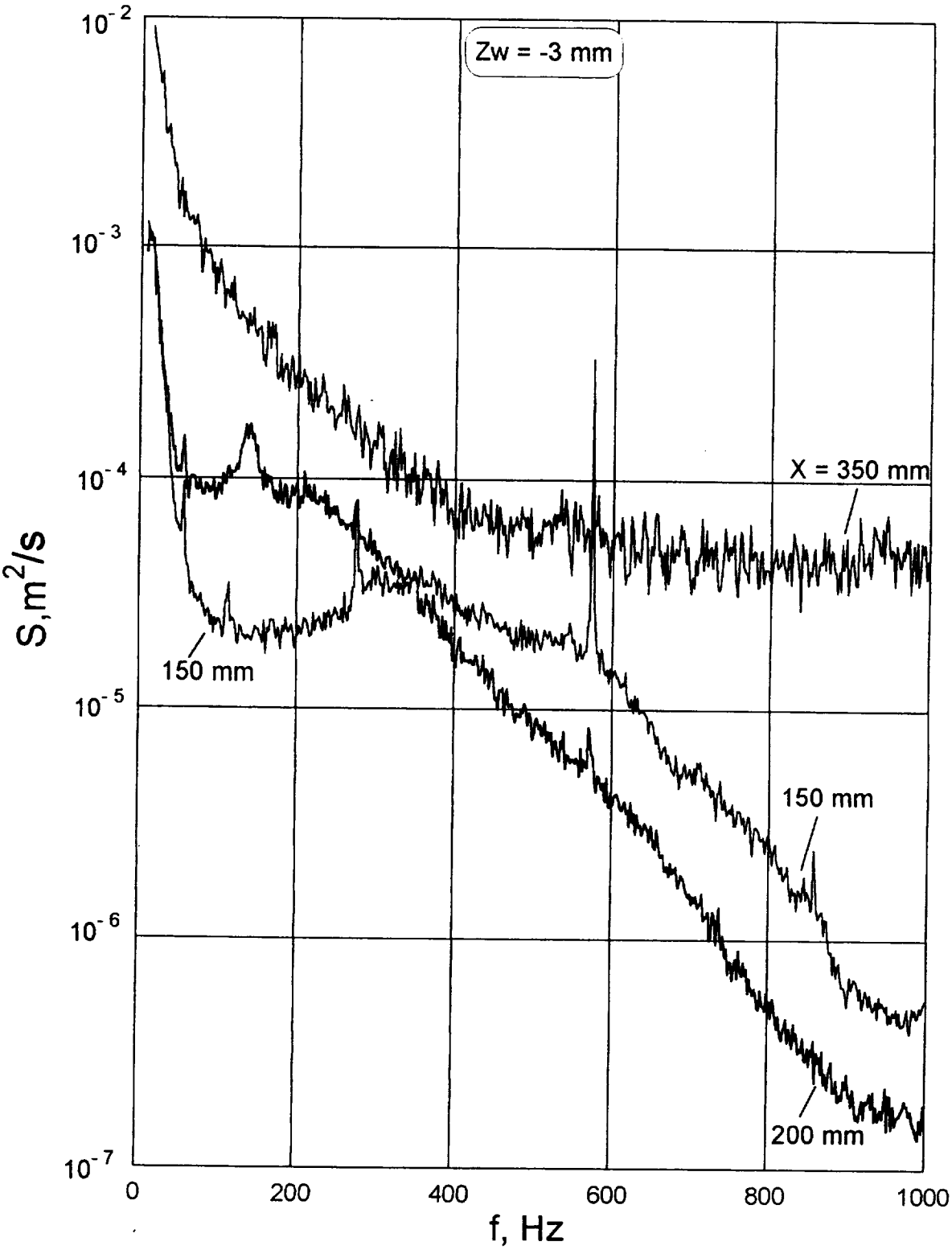

Figure 32. Evolution of power spectrum of streamwise velocity pulsations S(f) measured in the nearest to centre velocity maximum (z = - 3 mm) in boundary layer distorted by wake from 5 wires in configuration 22.

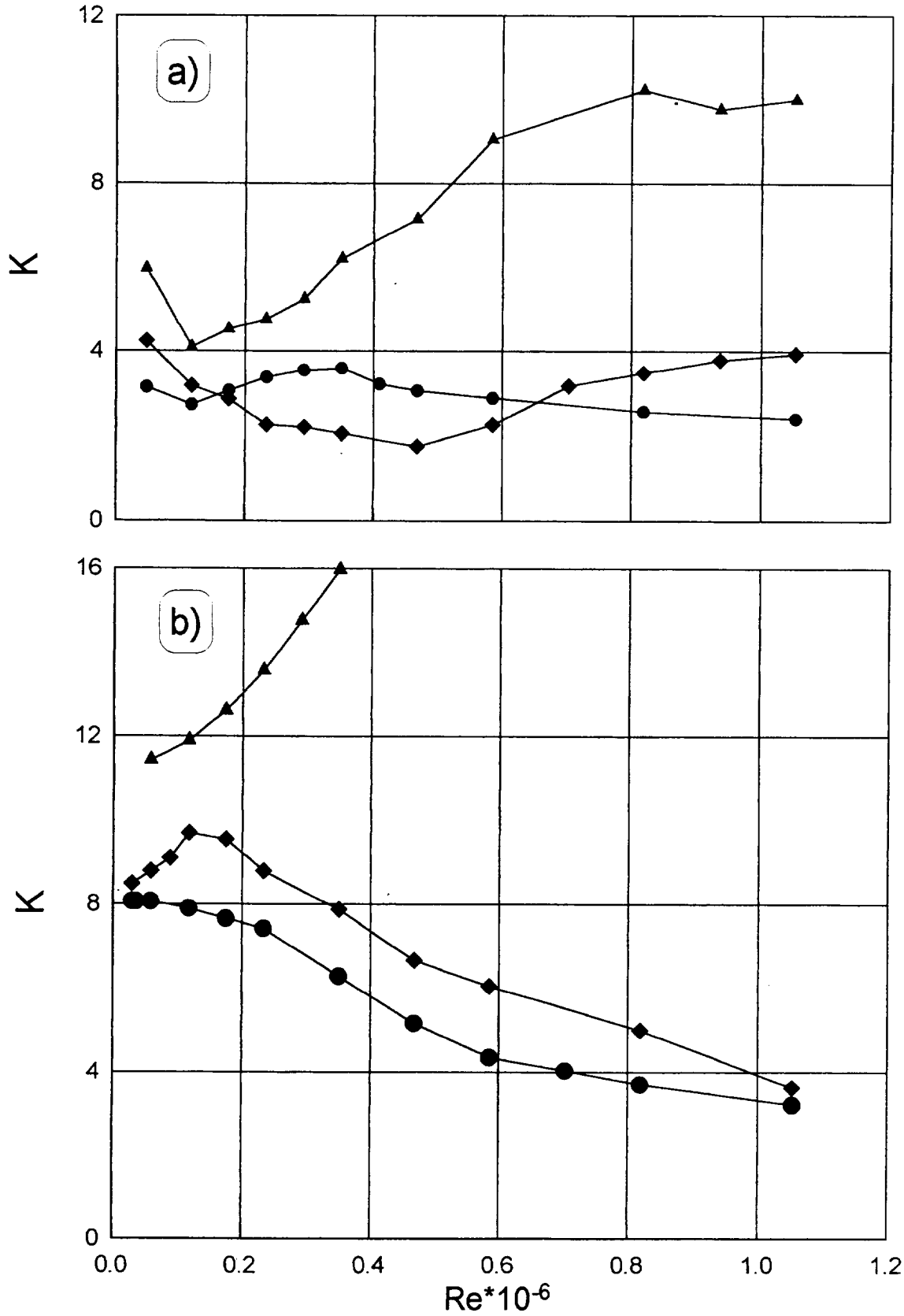

Figure 33. Amplification coefficient $k = \Delta u_b / u_o$ as function of Reynolds number $Re = u_\infty x/\nu$ for different wakes interaction with sharp nose plate № 1 (a) and blunt nose plate № 3 (b)

● - wake from wire of d = 0.09 mm at L = 40 mm, a.s. regime

◆ - wake from wire of d = 0.09 mm at L = 250 mm, s. and tr. regime

▲ - wake from wire of d = 0.09 mm at L = 725 mm, s. linear regime

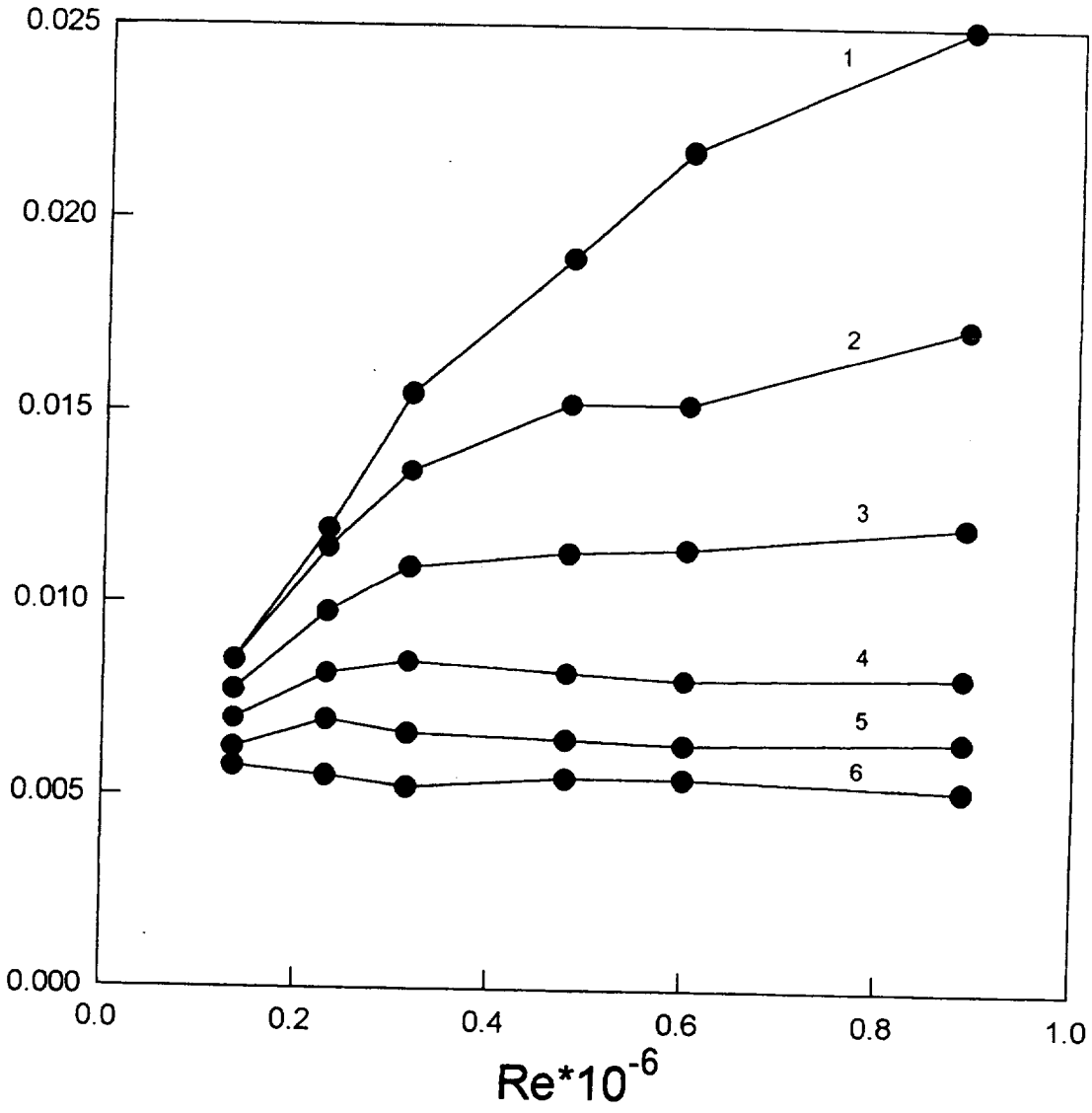

Figure 34. Velocity pulsations measured in different frequency renges in [9] as functions of Reynolds number $Re = u_\infty x/\nu$.

1- 4 - 8 Hz; **2**-8 -12 Hz; **3**-12 - 16 Hz;
4- 16 - 20 Hz; **5**-20 - 24 Hz; **6**-24 - 28 Hz

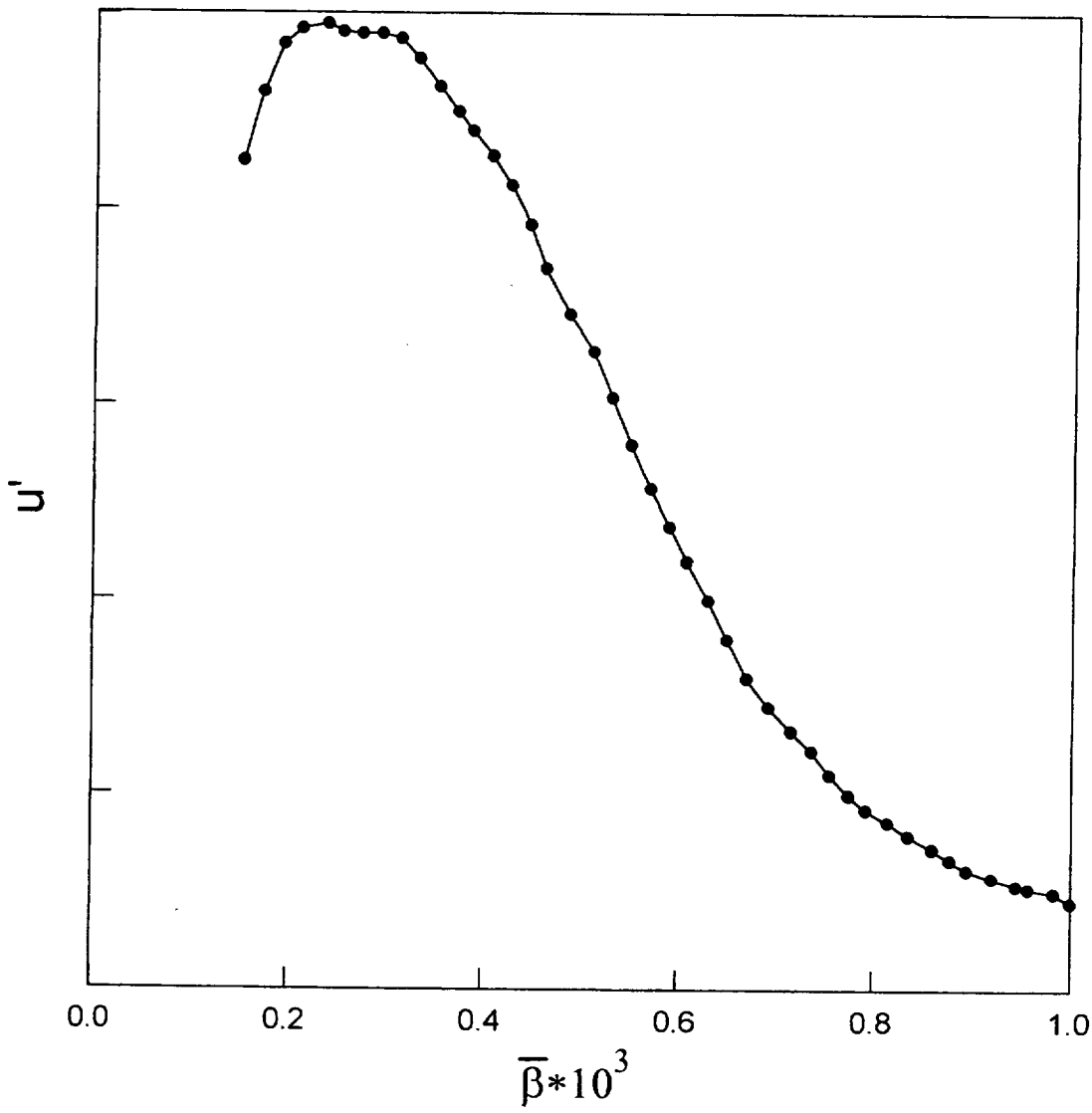

Figure 35. Broadband velocity pulsations in a boundary layer subjected to free-stream turbulence as function of spanwise wavenumber. Computed from data of Figure 5 of [9].

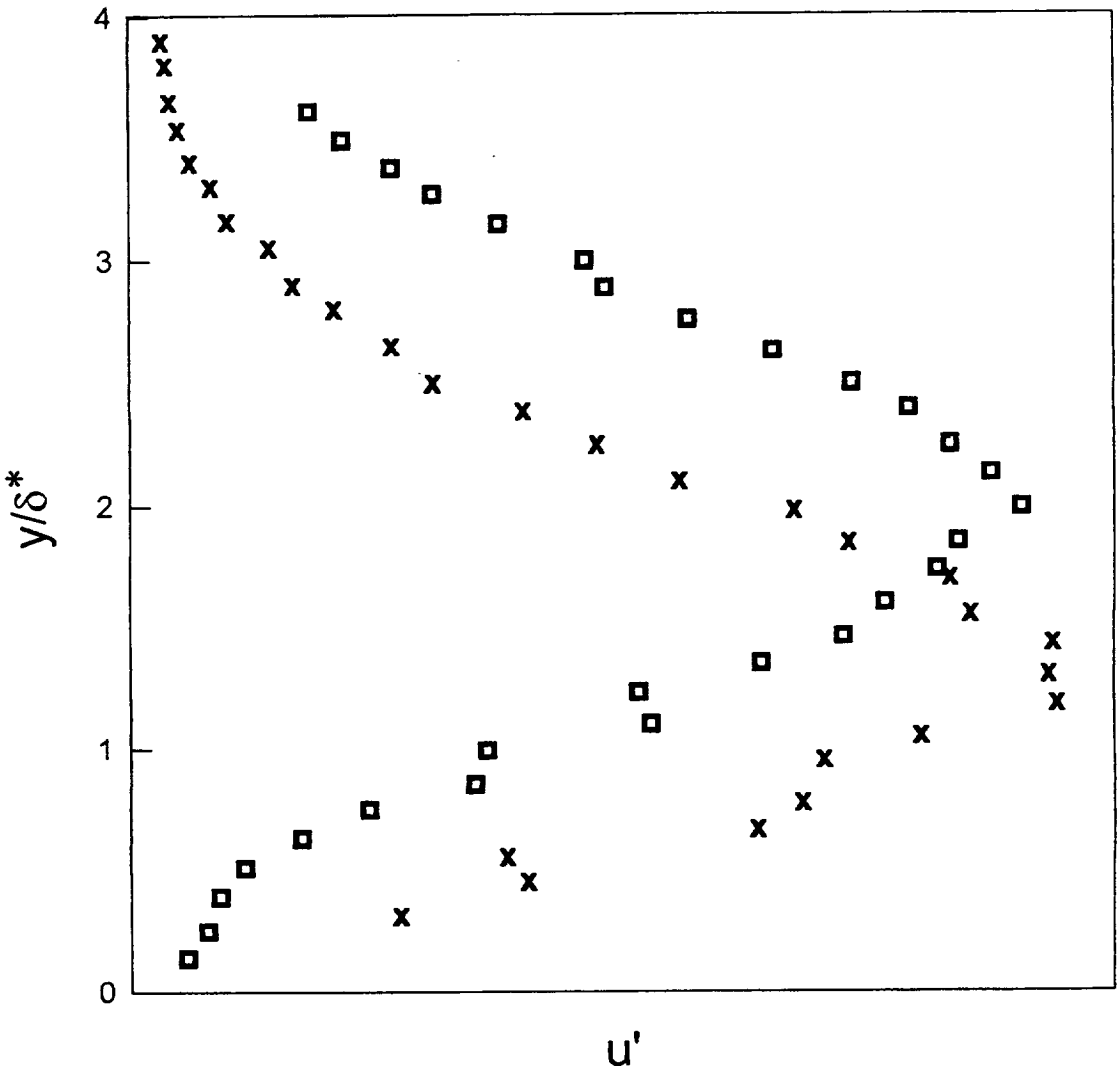

Figure 36. Vertical profiles of high-frequency (24 - 28 Hz) velocity pulsations in boundary layer measured by Kendall [9] at $x = 178$ mm (x) and $x = 1170$ mm (□)

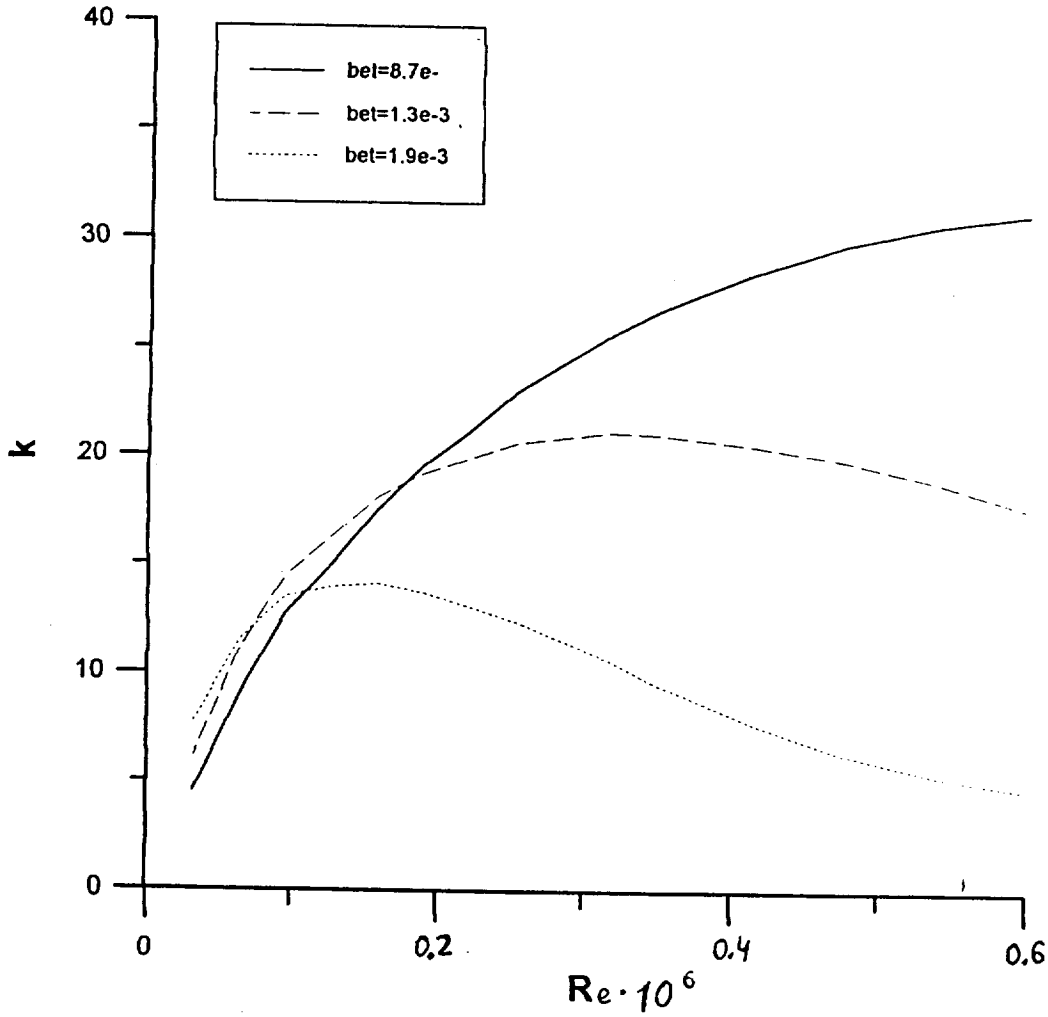

Figure 37. Amplification coefficients of optimally growing steady disturbances of different spanwise period as function of $Re = u_\infty x/\upsilon$ (computed from results of [12])

(——) - $\beta = 8.7 \cdot 10^{-4}$; (- - -) - $\beta = 1.3 \cdot 10^{-3}$; (·····) - $\beta = 1.9 \cdot 10^{-3}$

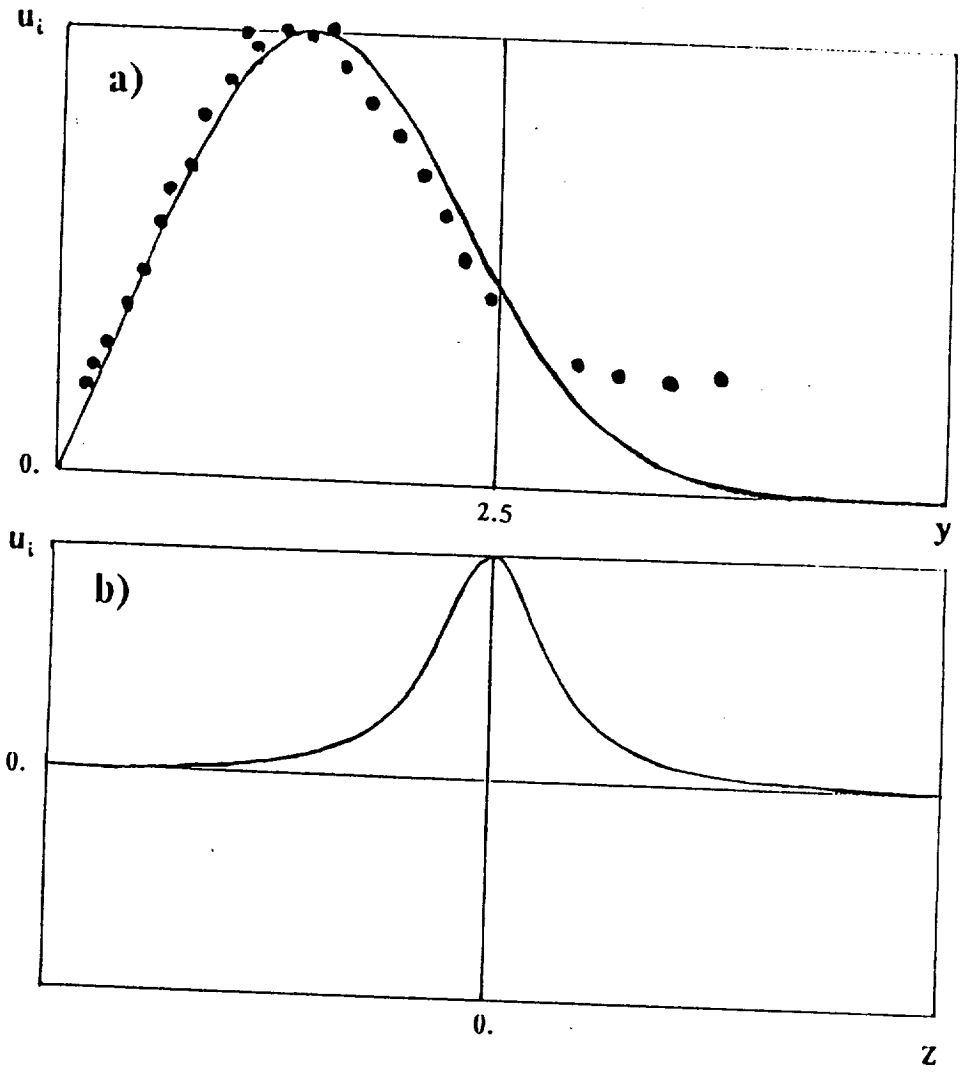

Figure 38. Vertical (a) and spanwise (b) profiles of flow inhomogeneity

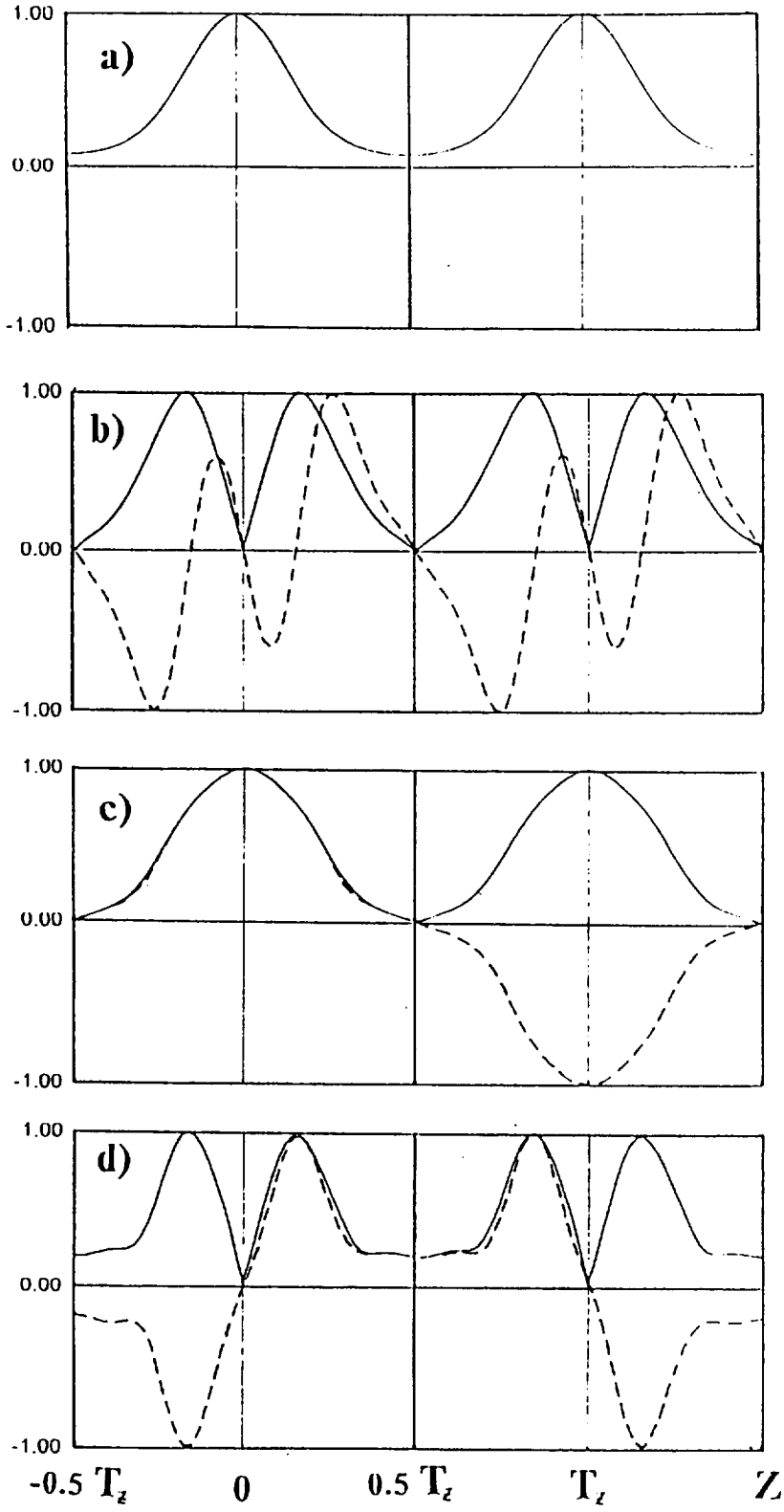

Figure 39.

Spanwise distributions of streamwise velocity of disturbances $Re(U)$ (- - - - -) and it's amplitude $|U|$ (———) in harmonically modulated flow with $a=-0.3, \alpha=0.25, \beta=0.6$

(a), (b) - symmetric and antisymmetric fundamental modes

(c), (d) - symmetric and antisymmetric subharmonic modes

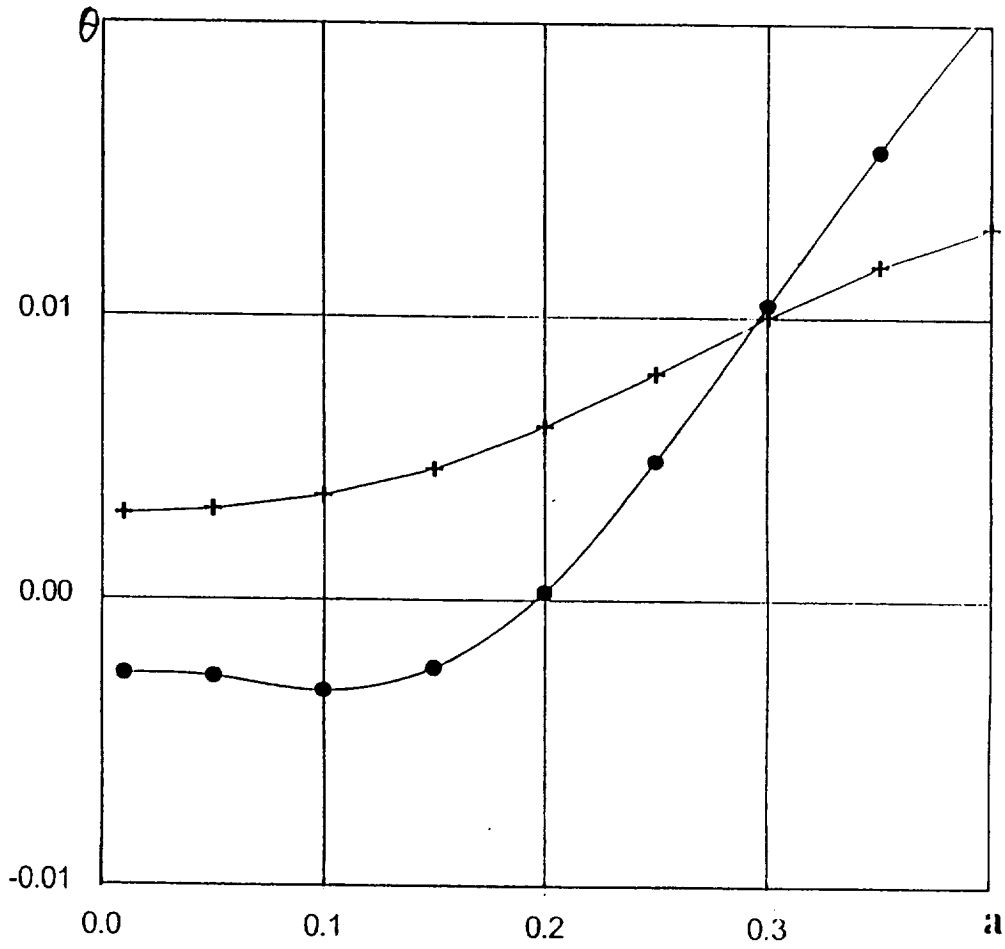

Figure 40. Growth rates of symmetric (— + —) and antisymmetric (—•—) modes as functions of modulation amplitude a in flow with $\alpha = 0.25$, $\beta = 0.6$.

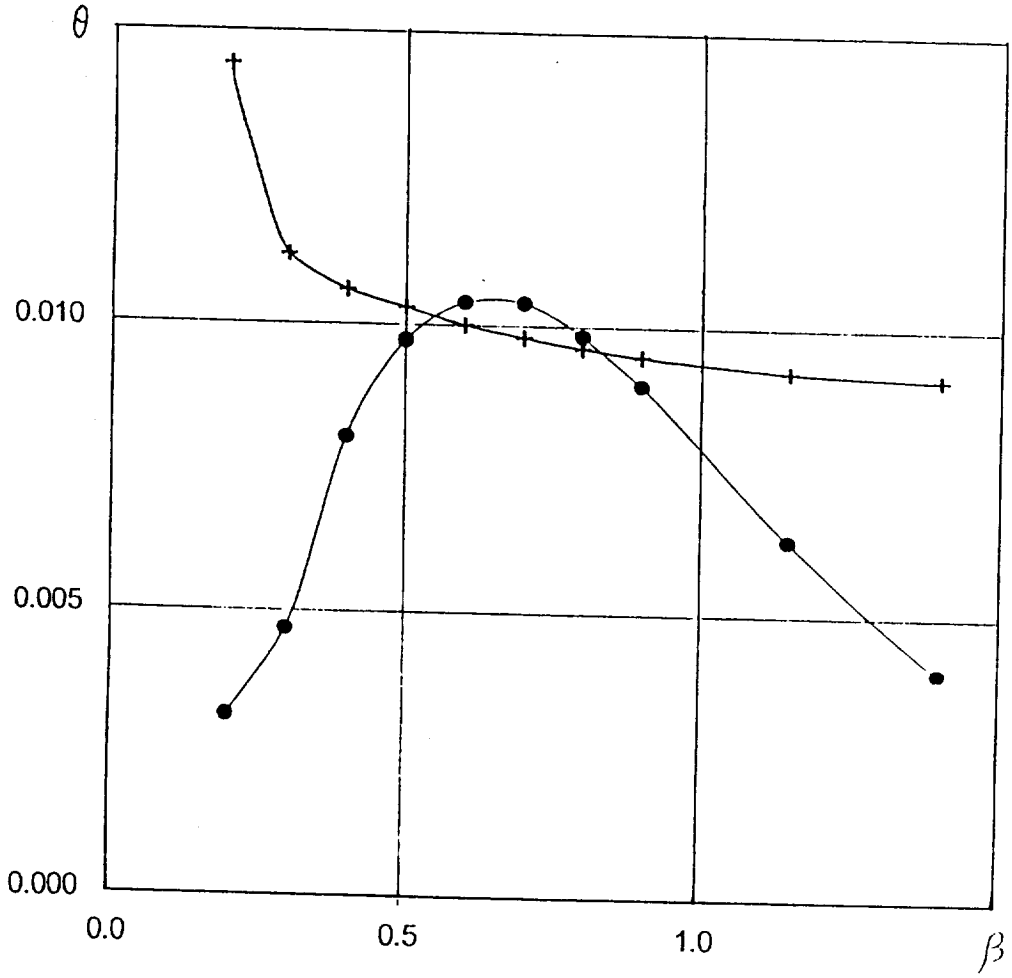

Figure 41. Growth rates of symmetric (– + —) and antisymmetric (—•—) modes as functions of β in flow with $\alpha = 0.25$, $a = -0.3$.

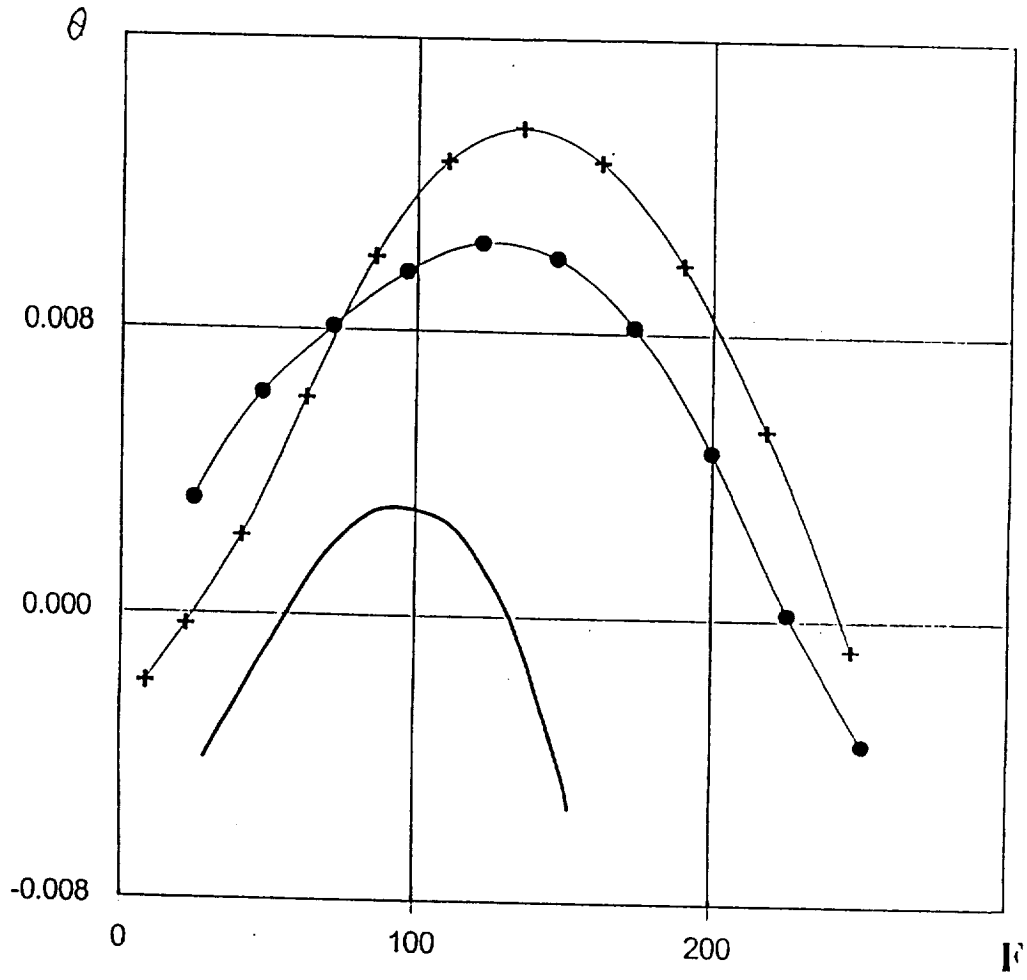

Figure 42. Growth rates v.s. reduced frequency F. Symmetric (—+—) and antisymmetric (—●—) modes for a=-0.3, β=0.6; (———) -TS waves

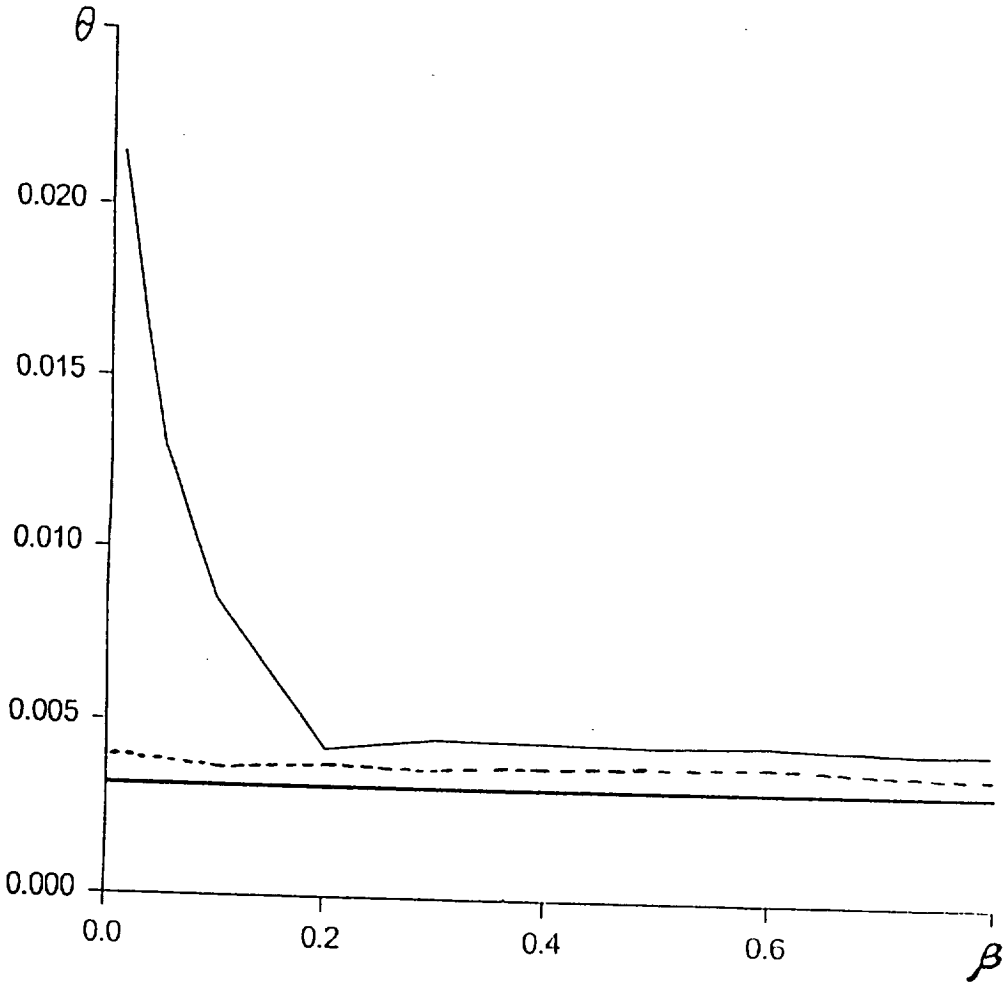

Figure 43. Growth rates v.s β for localized inhomogeneity flow (3.6) with $q=0.6$; (———) - $a=-0.3$; (- - - -) - $a=+0.3$; (▬▬) - TS wave

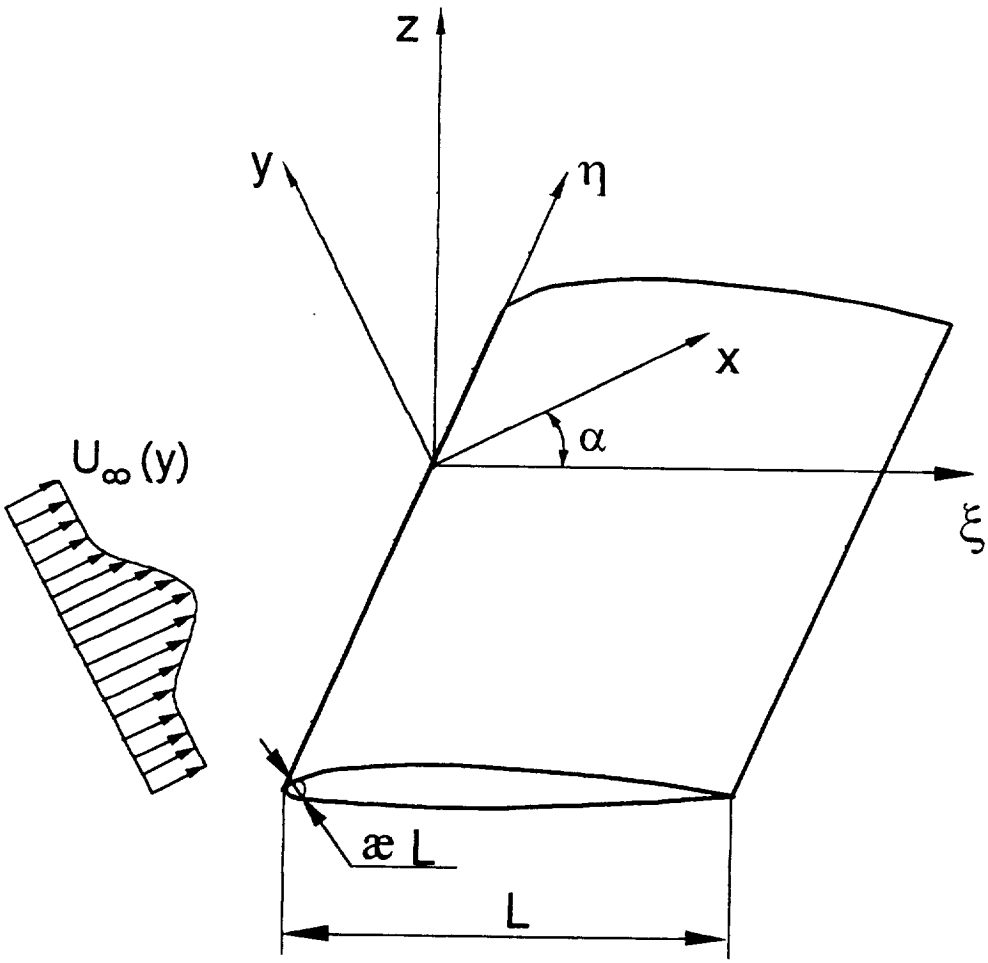

Figure 44. Flow configuration and coordinate systems used.

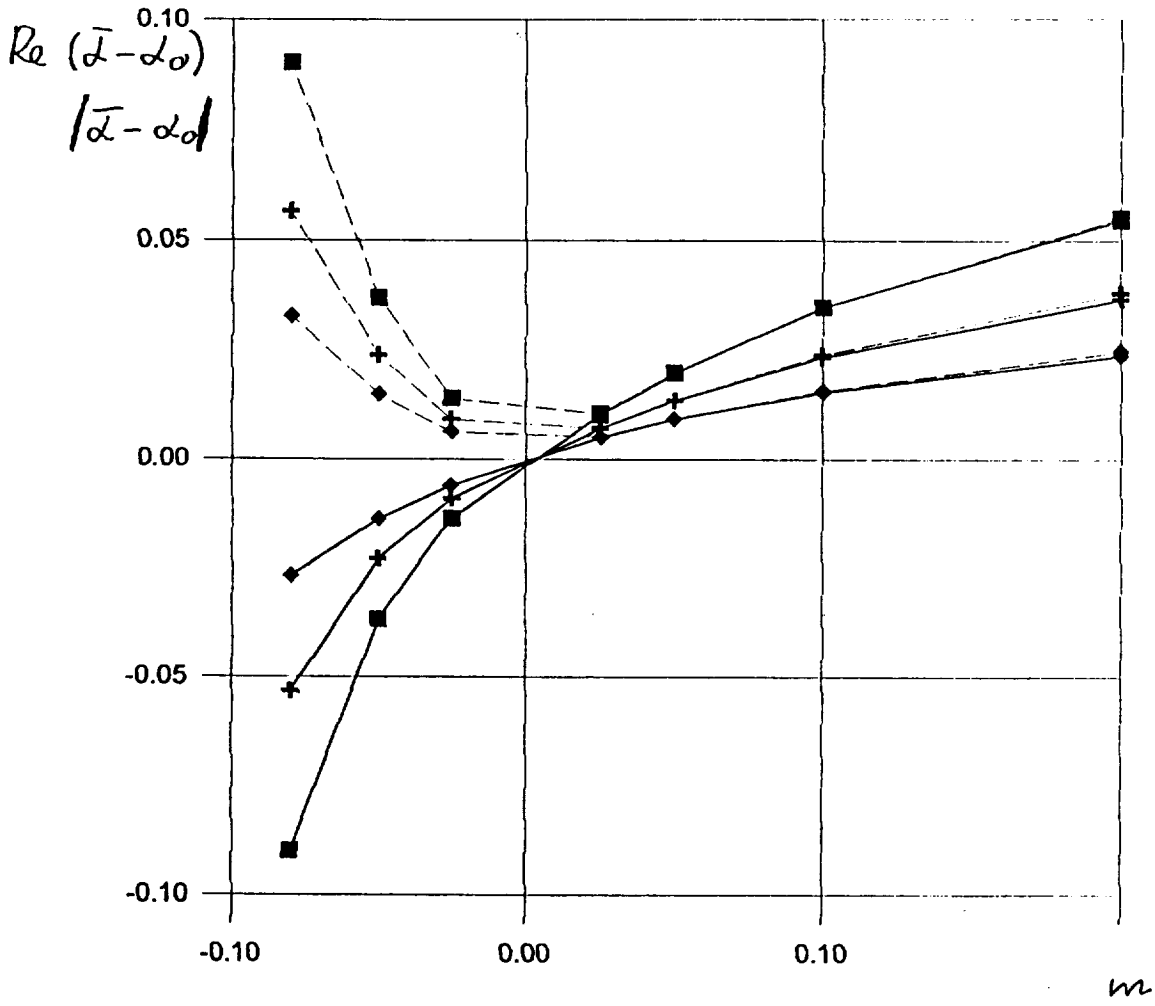

Figure 45. Real part (———) and absolute value (- - - - -) of $\bar{\alpha} - \alpha_0$ as functions of exponent m in Faulkner-Scan flow.
♦ - $\beta = 0.2$ + - $\beta = 0.4$ ■ $\beta = 0.6$.

REPORT DOCUMENTATION PAGE

Form Approved
OMB No. 0704-0188

1. AGENCY USE ONLY (*Leave blank*)	2. REPORT DATE	3. REPORT TYPE AND DATES COVERED
	June 1999	Contractor Report

4. TITLE AND SUBTITLE
Receptivity of Flat-Plate Boundary Layer in a Non-Uniform Free Stream (Vorticity Normal to the Plate) - Final Report

5. FUNDING NUMBERS
NCC1-241

282-10-01-01

6. AUTHOR(S)
M. N. Kogan, V. G. Shumilkin, M. V. Ustinov, and S. V. Zhigulev

7. PERFORMING ORGANIZATION NAME(S) AND ADDRESS(ES)
Central Aerohydrodynamics Institute (TsAGI)
Zhukovski
Moscow Region
140160
Russia

8. PERFORMING ORGANIZATION REPORT NUMBER

9. SPONSORING/MONITORING AGENCY NAME(S) AND ADDRESS(ES)
National Aeronautics and Space Administration
Langley Research Center
Hampton, VA 23681-2199

10. SPONSORING/MONITORING AGENCY REPORT NUMBER
NASA/CR-1999-209334

11. SUPPLEMENTARY NOTES
Langley Technical Monitor: Dennis M. Bushnell

12a. DISTRIBUTION/AVAILABILITY STATEMENT
Unclassified-Unlimited
Subject Category 34 Distribution: Standard
Availability: NASA CASI (301) 621-0390

12b. DISTRIBUTION CODE

13. ABSTRACT (*Maximum 200 words*)
Experimental and theoretical studies of low speed leading edge boundary layer receptivity to free-stream vorticity produced by upstream wires normal to the leading edge are discussed. Data include parametric variations in leading edge configuration and details of the incident disturbance field including single and multiple wakes. The induced disturbance amplitude increases with increases in the leading edge diameter and wake interactions. Measurements agree with the theory of M. E. Goldstein.

14. SUBJECT TERMS
Receptivity; Transition; Instability; Leading Edge

15. NUMBER OF PAGES
82

16. PRICE CODE
A05

17. SECURITY CLASSIFICATION OF REPORT	18. SECURITY CLASSIFICATION OF THIS PAGE	19. SECURITY CLASSIFICATION OF ABSTRACT	20. LIMITATION OF ABSTRACT
Unclassified	Unclassified	Unclassified	UL